TECHNISCHE UNIVERSITÄT MÜNCHEN

FACHGEBIET ORGANISCHE CHEMIE
UND
ZENTRALINSTITUT FÜR MEDIZINTECHNIK

Magnetic Resonance with Magnetic Nanoparticles - Fabrication and Characterisation

Christine Rümenapp

Vollständiger Abdruck der von der Fakultät für Chemie
der Technischen Universität München zur Erlangung des akademischen Grades eines

Doktors der Naturwissenschaften

genehmigten Dissertation.

Vorsitzende:	Univ.-Prof. Dr. Sevil Weinkauf
Prüfer der Dissertation:	1. Univ.-Prof. Dr. Steffen J. Glaser
	2. Univ.-Prof. Dr. Axel Haase

Die Dissertation wurde am 2. September 2013 bei der
Technischen Universität München
eingereicht und durch die Fakultät für Chemie am 14. Oktober 2013 angenommen.

Abstract

Magnetic nanoparticles have been used as ferrofluids in a variety of technical applications but also in life sciences. In the biomedical field they have been used as carriers for magnetic drug targeting and for the magnetic transfection of cells, in the hyperthermia treatment of cancer, as contrast agents for magnetic resonance imaging and for magnetic separation and purification of samples. For the separation and purification techniques the magnetic nanoparticles are functionalised with small molecules, proteins or genetic material to be able to bind specifically to their target. If magnetic nanoparticles bind specifically to a target the nuclear magnetic resonance T_2 relaxation time is changing. This fact can be used for a detection system based on the binding of magnetic nanoparticles to their target and/or their clustering in fluids and on the change of the nuclear magnetic resonance T_2 relaxation time.

In this work small, monodisperse, colloidal stable, magnetic nanoparticles with a narrow size distribution were prepared in large volumes using a combination of a co-precipitation of iron salts and a polyol method. They were coated with tetraethoxysilane and functionalised with (3-Aminopropyl)triethoxysilane for further functionalisation with antibodies. The particles were characterised using transmission electron microscopy, dynamic light scattering, Mössbauer spectroscopy, electron diffraction pattern, Fouriertransformed infrared spectroscopy, Zeta potential measurements, M(H) measurements as well as magnetic particle spectroscopy.

To establish the measurement set-up consisting of a 21.7 MHz ($\approx$ 0.5 T) nuclear magnetic resonance relaxometer and the manufactured magnetic nanoparticles, the particles were functionalised with an anti-avidin antibody for the detection of FITC-avidin. The lowest detectable concentration of FITC-avidin was 1.35 fM FITC-avidin with anti-avidin magnetic nanoparticles of 1 mM Fe iron content and a change in the nuclear magnetic resonance T_2 relaxation time of approximately 25%. This detection limit is half the detection limit of the literature, making the measurement set-up twice as sensitive.

This system was developed further for the detection of food spoiling organisms in the food and beverage industry. As a first target organism *Saccharomyces cerevisiae* was chosen, which is one of the main spoiling organisms in the production of alcohol free beverages. *S. cerevisiae* was detected at a concentration of $4{\cdot}10^8$ cells/ml using anti-*S. cerevisiae* magnetic nanoparticles at an iron concentration of 1 mM. This results in a very good detec-

tion limit for FITC-avidin, but an improvable detection limit for *S. cerevisiae*. The used antibodies for *S. cerevisiae* showed a very low binding affinity to *S. cerevisiae*, being one cause for this high detection limit. According to the literature, an improvement of the detection limit for targets of the size of *S. cerevisiae* can be achieved by an increase of the magnetic particle size. Therefore, to reach better results for the application for the detection of *S. cerevisiae* in the quality control the particle size could be increased for a better detection signal and the binding affinity of the anti-*S. cerevisiae* antibodies could be improved as well.

Zusammenfassung

Magnetische Nanopartikel werden bisher als Ferrofluide in der Technik, aber auch in den Lebenswissenschaften angewandt. Im Bereich der Medizin werden sie für die Krebstherapie mit Hyperthermie, für die Magneto-Transfektion, als Träger für die zielgerichtete Verabreichung von Medikamenten mit Hilfe von Magnetfeldern und als Kontrastmittel für die Magnetresonanztomographie eingesetzt. In biologisch-chemischen Laboren werden sie für die Auftrennung bzw. Aufreinigung von Proben benutzt. Dazu werden die magnetischen Nanopartikel mit kleinen Molekülen, Proteinen, oder genetischem Material funktionalisiert, damit sie in der Lage sind an ihre Zielmoleküle spezifisch zu binden.
Durch das Anbinden von Zielmolekülen an magnetische Nanopartikel und deren mögliches Aggregieren ändert sich die bei der Kernresonanztomographie gemessene T_2 Relaxationszeit. Diese Veränderung in der T_2 Relaxationszeit kann für die Detektion von verschiedenen Stoffen in Flüssigkeit genutzt werden. Ein Messsystem besteht hierbei aus den magnetischen Nanopartikeln und einem Kernspinresonanz-Relaxometer mit welchem die T_2 Relaxationszeit gemessen werden kann.

In dieser Arbeit wurden kleine, monodisperse und kolloidal-stabile, magnetische Nanopartikel hergestellt. Für die Herstellung von möglichst großem Volumen wurde die Co-präzipitation zusammen mit einer Polyolmethode angewandt. Die so produzierten magnetischen Nanopartikel wurden mit Tetraethoxysilan ummantelt und anschließend mit (3-Aminopropyl)triethoxysilan funktionalisiert um eine Anbindung von Antikörpern möglich zu machen. Alle hergestellten magnetischen Nanopartikel wurden mit Hilfe von Transmissionselektronenmikroskopie, dynamischer Lichtstreuung, Mössbauer Spektroskopie, Elektronendiffraktion, Fouriertransformierter Infrarotspektroskopie, Zetapotenzialmessungen, M(H) Messungen und Magnet Partikel Spektroskopie charakterisiert.

Für die Etablierung des Messverfahrens bestehend aus einem Kernspinresonanz-Relaxometer mit 21.7 MHz ($\approx$ 0.5 T) und den hergestellten magnetischen Nanopartikeln wurden diese zunächst mit einem Antikörper gegen Avidin funktionalisiert. FITC-avidin konnte damit bereits bei einer Konzentration von 1.35 fM mit anti-avidin magnetischen Nanopartikeln mit 1 mM Eisenkonzentration bestimmt werden. Der dabei entstandene Unterschied in den T_2 Relaxationszeiten betrug ca. 25%. Im Vergleich mit der Literatur wurde das Detektionslimit halbiert. Das bedeutet, dass das etablierte Messverfahren im Vergleich doppelt so sensitiv ist.

Als Anwendungsgebiet wurde die Qualitätskontrolle in der Lebensmittelindustrie gewählt. Zu den qualitätsschädlichen Keimen in der Herstellung von alkoholfreien Getränken wird auch *Saccharomyces cerevisiae* gezählt. Mit dem genannten Messaufbau und magnetischen Nanopartikeln funktionalisiert mit Antikörpern gegen *S. cerevisiae* bei einer Konzentration von 1 mM Eisen wurde *S. cerevisiae* bei einer Konzentration von $4{\cdot}10^8$ Zellen/ml detektiert. Dieses Limit ist für den Einsatz der Methode in der Industrie noch zu hoch. Untersuchungen zeigten eine geringe Bindungsaffinität des verwendeten Antikörpers an *S. cerevisiae*. Somit kann die Verwendung von einem Antikörper mit einer besseren Bindungskonstante zu einer besseren Sensitivität des Messsystems führen.

Contents

1. Introduction

Magnetic nanoparticles are monodisperse, superparamagnetic, nanometer-sized particles made of metals, metal alloys or metal oxides. The first magnetic nanoparticles were used in *magnetic fluids* and made of iron oxides. These magnetic fluids were prepared for the use in clutches and breaks in the 1940s. They were very polydisperse and made up of micro sized or even larger particles, which solidified completely in the presence of a magnetic field [1].
Later *ferrofluids* were synthesised where the magnetic nanoparticles were dispersed in organic media. The size of the magnetic nanoparticles in these fluids was decreased to 3-15 nm making them almost monodisperse and they were now colloidal stable and stayed fluid under the influence of a magnetic field [1]. Ferrofluids are used in many technical applications like rotating shaft seals, seals for vacuum chambers, bearings and dampers in cars or in loudspeakers where they are held in place by permanent magnets [2]. From their technical application the use of magnetic nanoparticles was also established in the field of life science. However, the requirements changed. For the application in life science they not only had to be superparamagnetic and single-domain, they also had to be monodisperse, colloidal stable in aqueous solutions, biocompatible and biodegradable. Due to these new requirements various kinds of synthesis methods were developed and are still under investigations. The most common methods are the co-precipitation of iron salts precursors and thermal decomposition methods of iron organic precursors [3, 4, 5]. These methods and their further development made it possible to design magnetic nanoparticles according to the requirements of their application.
To make magnetic nanoparticles biocompatible they are coated with biocompatible materials, like dextran, silica or carboxylates [6]. The first commercial particles with these coatings were *contrast agents* for magnetic resonance imaging [7, 3, 8, 9]. This imaging technique is based on the nuclear spins of certain nuclei, like the hydrogen in water molecules. If protons are subjected to a strong magnetic field, they align in the direction of the magnetic field. After their excitation with a series of radio-frequency impulses the decay of their total magnetisation is monitored. This signal decay depends on the magnetic field and on the density of water present in a tissue and is differentiated into the T_1 relaxation time and the T_2 relaxation time. By introducing magnetic nanoparticles in a tissue, they induce magnetic field inhomogeneities. In so-called T_2 weighted images, the presence of magnetic nanoparticles leads to a signal loss and the locations of the magnetic nanoparticles appear black [10]. For the contrast enhancement in T_1 weighted images paramagnetic contrast agents are used [11]. Besides the use as contrast agents in magnetic resonance imaging, magnetic nanoparticles are used in another imaging modality called magnetic particle imaging. In this method only the magnetic nanoparticles are detected. It is based

on the non-linear magnetisation curve of small magnetic nanoparticles and results in a high spatial resolution and a high sensitivity compared to magnetic resonance imaging [12, 13]. Magnetic nanoparticles with a diameter of 19 nm result in a spatial resolution of 0.8 mm [14].
Another applicaton of magnetic nanoparticles in the medical field is their use in the therapy of cancer. One way to do this is called *hyperthermia*, where the tumour is treated by heating up the tissue to 43 °C and thereby destroying the cancer cells. The magnetic nanoparticles are subjected to the tumour and subsequently an oscillating magnetic field with a frequency of 100 kHz is applied. Under the influence of the magnetic field the particles are rotating and heating up. This temperature causes the tumour cells to die and eventually the tumour can be treated. This technique has been successfully applied to glioblastomas [15] and prostate cancer [16].
To be able to target the cancer tissue more specifically and to avoid systemic side effects of chemotherapeutica *magnetic drug targeting* was developed [17]. For this purpose magnetic nanoparticles were not only coated with biocompatible substances but were loaded with drugs, DNA, proteins or cells and directed to the regions of interest by applying external magnetic fields [18, 19, 20, 21]. These magnetic fields need to be designed accordingly to the properties of the magnetic nanoparticles and to the region of interest [22, 23, 24]. To improve the properties of magnetic nanoparticles for magnetic drug targeting the magnetic moment of the particles is increased by combining single domain particles together in one bigger particle by silica or polymer coatings. The draw back is still the application of the magnetic fields. Due to the blood flow and the penetration depth of the magnetic field in the human body, the application of magnetic drug targeting inside the human body is still a challenging task [23].
Magnetic nanoparticles which are binding specifically to a target can also be used for *purification and separation* techniques as well as for *magnetic transfection* of cells in the cell culture. These particles are larger than 10 nm or even in the micrometer size range to make them easier to trap with magnetic fields due to their higher magnetic moments [2]. Since these methods are *in vitro* methods, a larger size of the particles is not a problem for the application. For the separation and purification techniques these particles carry specific molecules which are able to bind to the target in question. Those targets can be small molecules, proteins, DNA, cells or pathogens [2]. The particles are incubated with the sample and bind to the target. Subsequently, a magnetic field is applied to retrieve the magnetic particles with their target out of the sample. This technique is used to purify samples at a laboratory scale [25], products from biotechnological reactor applications [26] and to clean waste-water from pollutants [27]. For the magnetic transfection of cells in the cell culture the particles carry DNA or viruses, are added to a adherent cell culture and are transfered into the cells by applying a magnetic field underneath the culture flask [28].
Combining the purification method and magnetic resonance imaging, the *NMR T_2 relaxation time* of the sample changed, if the magnetic nanoparticles bind to a target and agglomerate. The theory to the changing of the relaxation times of protons in the presence of magnetic nanoparticles was examined in more detail in 1999 by Roch et al. [29]. By the use of theoretical models, they showed a dependence of the T_2 relaxation time on the

magnetic nanoparticle size [30, 31]. The first applications of this effect were reported by Weissleder et al. who used the effect of the change in the T_2 relaxation time upon the clustering or dispersion of magnetic nanoparticles to detect small molecules, DNA, proteins, bacteria, viruses and cells [32]. Tumour tissue was also profiled with this technique for certain tumour markers. The same effect is used for the new imaging modality of functional magnetic resonance imaging [33]. Using this imaging technique it is possible to investigate molecular pathways occuring in the brain upon learning.

In this work, T_2 relaxation time measurements for the detection of specific targets were transfered to the quality control in the food and beverage industry. Magnetic nanoparticles were prepared and characterised for their application in the detection of quality spoiling organisms, especially in the beverage industry. Food spoiling organisms are not a danger for human health but are costly for the industry if products are contaminated [34, 35]. In the beverage industry, these organisms cause a change in the taste, colour and also texture of the beverage [34]. In the case of alcohol free beverages *Saccharomyces cerevisiae* is classified as a spoiling organism. *S. cerevisiae* is also known as Baker's yeast and is needed for the fermentation processes involved for the production of beer. Alcohol free beverages contaminated with *S. cerevisiae* would show an alcohol concentration. To detect *S. cerevisiae*, magnetic nanoparticles were prepared, fully characterised and functionalised with anti-*S. cerevisiae* antibodies. The binding of the magnetic nanoparticles to *S. cerevisiae* was detected using NMR T_2 relaxation time measurements and visualised using bright field and transmission electron microscopy. The detection limit was determined by titrating different concentrations of *S. cerevisiae* to magnetic nanoparticles of the same iron concentration. The measurement system, consisting of the manufactured magnetic nanoparticles and a spectrometer of 21.7 MHz ($\approx$ 0.5 T), and the preparation of the magnetic nanoparticles was established using avidin as a target molecule. Avidin, a well characterised protein complex, is a tetramer made of four equal subunits. With antibodies against the subunits bound to magnetic nanoparticles, a clustering of the magnetic nanoparticles was induced. This clustering was then followed with NMR T_2 relaxation time measurements for the detection of avidin. To determine the detection limit of the measurement system for avidin different concentrations of avidin were incubated with the same concentration of magnetic nanoparticles and the T_2 relaxation time was measured.

In the next chapter the physical and chemical properties of magnetic nanoparticles and the reaction theory of their synthesis will be introduced. Furthermore, the chemistry of iron oxides and iron ions as well as the chemistry of the relevant coatings and bioconjugate techniques used for their functionalisation are described.

Following the theoretical aspects of this work, the methods are described in *Chapter 3*. The preparation of the particles as well as their coating and functionalisation is explained. The coating and the functionalisation are conducted by the introduction of covalent bonds between the particle and the coating and the functionalisation. The particles were char-

acterised at all manufacturing stages according to their core, their size, their surface and their magnetic behaviour. Their iron oxide chemistry was examined using Mössbauer spectroscopy and their size was determined by dynamic light scattering and transmission electron microscopy. Their coatings were verified by fourier transformed infrared spectroscopy , Zeta potential measurements and transmission electron microscopy. For the determination of their magnetisation and relaxivity properties, M(H) measurements, magnetic particle spectroscopy and T_2 relaxtion measurements were conducted.

In *Chapter 4* the results from the different characterisation methods of the magnetic nanoparticles are presented. Results of the titration and long-term experiments for the detection of avidin and *S. cerevisiae* are given together with brightfield and transmission microscopy images of the clustering of the magnetic nanoparticles.

Chapter 5 compares the results of the different characterisation methods with each other and with the literature. The detection limits for avidin and *S. cerevisiae* are discussed with respect to the literature and are compared with each other. A conclusion of this work is given in *Chapter 6*.

2. Theory

2.1. Magnetic Nanoparticles

2.1.1. Physical and Chemical Considerations

Due to their size and their magnetic properties magnetic nanoparticles (MNPs) show physical behaviour different from the bulk material. In the following the magnetism of nanoparticles, their physical interactions and factors for their colloidal stability are introduced.

Magnetism

The material of the core as well as the size and shape of a superpara- and ferromagnetic particle mainly define its magnetic properties. The type of core material defines whether the particle is para-, ferro-, or ferrimagnetic at a given temperature. In general, magnetism depends strongly on the temperature. If the temperature is higher than the material specific Curie temperature, ferromagnetism and thus superparamagnetism disappears and the material shows paramagnetic behaviour [1]. In the next paragraphs first an overview over different types of magnetism is given. Afterwards the magnetism of iron oxide particles is explained in more detail.

Paramagnetism Each atom of a paramagnetic material behaves as individual, non-interacting and randomly orientated molecular magnet with a magnetic dipole moment. Therefore no Weiss domains exist [1]. In absence of an external magnetic field all dipoles of a paramagnetic material are oriented at random. If an external magnetic field is applied to paramagnetic materials, the molecular magnets start to align with the direction of the external magnetic field. Increasing the magnetic field strength causes more and more molecular magnets to align with the external field until all molecular magnets are aligned. Complete alignment of the particles with the external field is defined as magnetic saturation. Paramagnetic substances are liquid oxygen, rare-earth salt solutions and ferromagnets above their Curie-temperature [1]. Their magnetic saturation in paramagnetic materials can only occur at very low temperatures or at very high magnetic field strengths. Paramagnetic gadolinium chloride, for example, starts to saturate at approximately 50 T [36]. Once the external magnetic field is removed all molecular magnets will instantaneously orientate at random

again due to thermal fluctuations. Hence, no net magnetisation or remanence occurs in paramagnetic particles.

Ferromagnetism and cognate magnetism (ferrimagnetism, antiferromagnetism) are characterised by a strong exchange interaction energy, which leads to a regular orientation of the magnetic moments. In contrast to paramagnetic material, the magnetic moments of atoms in ferromagnets are fixed in their direction and organised in so-called Weiss domains. Depending on the alignment of the magnetic moments in the domains the magnetic behaviour can be devided in ferromagnetism (all moments are aligned in the same direction), antiferromagnetism (the magnetic moments are alternating their direction in each domain) or ferrimagnetism (the magnetic moments are unequal and are alternating their direction) [1]. Nanoparticles with sizes larger than a diameter, D_{sd}, consist of multiple Weiss domains, each separated by a domain wall (Figure 2.1) [37, 38]. As long as no external magnetic field is applied, there is no necessity for the magnetic moments in the different Weiss domains to orientate themselves in the same direction. In the presence of an external magnetic field the domain walls will reorganise and the total magnetic moment, as well as the magnetisation, $\vec{M}$, of the ferromagnetic particle, start to align with the external field. After removing the external magnetic field, the magnetisation of the ferromagnetic particle can be partially or even fully retained, the particle shows a magnetic remanence and can act as a permanent magnet. Particles made of magnetite or maghemite having multiple domains are ferrimagnetic [1].

Figure 2.1 relates the sizes of nanoparticles of different material to their magnetic behaviour. To obtain a first hint of the particle size of a single domain particle, the magnetisation reversal energy (the energy for the magnetic moments to flip their direction) can be set equal to the thermal energy. This size for which magnetic nanoparticles exhibit superparamagnetic behaviour is different for each material (Figure 2.1) [39]. In reverse, for known sizes the blocking temperature can be calculated as well. As mentioned before, depends the number of Weiss domains strongly on the size of the particle. If the size of the ferromagnetic core, D_c, is smaller than a critical size, D_{sd}, the multiple domain state will be abandoned for the benefit of an energetic more favourable single domain state (Figure 2.1). These single domain particles consist of only one Weiss domain, so that all of the internal dipole moments point in the same direction. The magnetic moment of the ferromagnetic single domain particle is proportional to its volume. In ferromagnetic single domain particles, the magnetisation can only be changed by relaxation of the entire particle (Brownian relaxation) and the magnetisation vector (Néel relaxation) and not due to reorganisation of the domain walls [40]. The Brownian relaxation can be expressed as

$$\tau_B = \frac{3V\eta}{k_B T} \tag{2.1}$$

and the Néel relaxation as

$$\tau_N = \frac{1}{f_0} \exp^{\frac{K_a V}{k_B T}}, \tag{2.2}$$

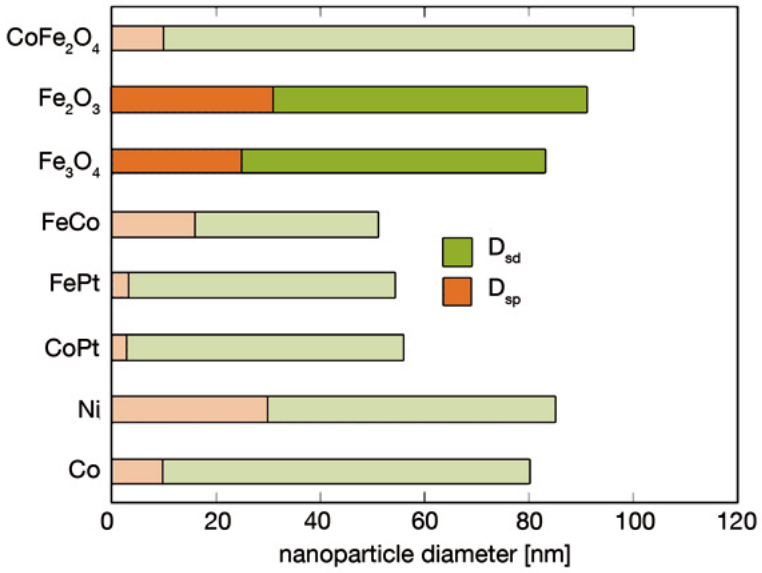

Figure 2.1.: At a given temperature nanomaterials show a distinctly different behaviour for different sizes. The critical sizes for the observation of superparamagnetism and single-domain behaviour, D_{sp} and D_{sd}, respectively, in a variety of common ferromagnetic fine particles are shown. For core diameters $D_c < D_{sp}$, they exhibit superparamagnetism; for $D_c > D_{sd}$, they split into multiple domains to minimise their overall energy and between $D_{sp} < D_c < D_{sd}$, they are ferromagnetic and single domain. The data are calculated from the known saturation magnetisation of the particles, from their anisotropy constant and from the exchange stiffness at a given temperature at an assumed measurement time of the magnetisation of 100 s (adapted from [39]).

where η is the damping constant, V the volume of the particle, k_B the Boltzmann constant, T the temperature, f_0 a frequency of 10^9 Hz and K_a is the anisotropy constant. If even the smaller value of one of the two relaxation mechanisms (Brown or Néel) is much greater than the time scale of an experiment the particle or sample can be regarded as ferromagnetic [1]. Magnetic saturation occurs at small external fields compared to paramagnetic particles. Saturation is achieved, for example, at 1-2.5 T for massive steel and can be 0.15-0.25 T for iron oxide nanoparticles [1, 14, 41, 42].
Next to the magnetisation of the particle the single domain particle is also characterised by its anisotropy energy, E_a. The magnetic energy of a magnetic nanoparticle depends strongly on the direction of its magnetisation vector in respect of its crystallographic directions. The directions that minimise this energy, that means when both directions are parallel, are called easy axes. The more the tilt angle between both increases the more increases the magnetic energy. This leads to a variation of amplitude of the energy curve which is called anisotropy energy. This energy can be expressed as:

$$E_a = K_a V \tag{2.3}$$

This means that E_a is proportional to the volume of the particle, the bigger the particle the

higher its anisotropy energy [3]. The anisotropy field of the particle can be influenced by the crystal agglomeration and there are four contributions to be mentioned [3]:

1. the bulk magnetocrystalline anisotropy field, which depends on the chemistry and the crystalline structure of the particle,
2. the demagnetising field, which is determined by the shape of the particle. For a spherical particle it is zero and increases with the elongation of the particle.
3. the anisotropy constant, which depends on the surface structure of the crystal,
4. the dipolar interaction of agglomerated particles, which increases with the decrease of the distance between the particles in the cluster.

Superparamagnetism occurs, if the size of a ferromagnetic single domain particle is further decreased, so that D_c is smaller than a second critical size D_{sp} (Figure 2.1). In those particles thermal fluctuations outcompete the dipole-dipole interactions and cause the magnetisation to flip randomly in absence of an external magnetic field [43]. For the magnetisation to flip the anisotropy energy has to be overcome [1]. If the thermal energy is higher than the anisotropy energy those fluctuations of the magnetisation in the particle can be induced. The time needed for the magnetisation to flip between the easy axes, the Néel relaxation time, can also be expressed in terms of the anisotropy energy, following the Arrhenius law, as

$$\tau_N = \tau_0(E_a) e^{\frac{E_a}{k_B T}}, \tag{2.4}$$

where $\tau_0(E_a)$ is a anisotropy energy depend time constant given by

$$\tau_0(E_a) = \frac{\sqrt{\pi}}{4} \frac{(M_{s,0} V)}{E_a \gamma_e} \left[\frac{1}{\eta_f} + \eta_f \left(\frac{M_{s,T}}{M_{s,0}} \right)^2 \right] \sqrt{\frac{kT}{E_a}} \left(1 + \frac{k_B T}{E_a} \right), \tag{2.5}$$

where $M_{s,0}$ is the specific magnetisation of the crystal extrapolated at 0 K, $M_{s,T}$ is the specific magnetisation at room temperature, γ_e is the gyromagnetic ratio of the electron ($= 1.76 \cdot 10^{11}$ $s^{-1}T^{-1}$), η_f is a dimensionless constant, $\eta_f = \eta \gamma_e M_{s,0}$ [3]. Therefore, the anisotropy energy and the volume of the particle determine its Néel relaxation time. All together, the energy barrier, which separates the ferromagnetic single domain state from the superparamagnetic state, is proportional to the volume of the particle, to the anisotropy constant and to the measurement time [39]. This means, that for small particles the magnetic reversal energy becomes small enough, for their magnetic moments to become unstable, or thermally activated. This is an important factor for their colloidal stability, since the interaction between the particles will change, if they are subjected to an external magnetic field. An approximation of the particle volume can be made by setting the magnetisation reversal energy equal to the thermal energy and deriving for its radius, r, with the approximation

$$r \sim \left(\frac{k_B T}{M_{s,T}^2}\right)^{1/3}. \tag{2.6}$$

As one can see in Figure 2.1, are the critical sizes, D_{sd}, for ferromagnetic single domain particles and D_{sp} for superparamagnetic particles different for different materials [39]. Superparamagnetic particles have, exactly like paramagnetic particles, no net magnetisation if no external field is applied. However, the needed external field strength to saturate superparamagnetic particles is comparable to the field strength for ferromagnetic particles [1, 14, 41, 42].

The net magnetisation of MNPs is smaller compared to bulk material due to surface effects of the spins. Since nanoparticles have a high surface to volume ratio a large percentage of the atoms are surface atoms. This also implies that most of the spins of the MNP are surface spins. These surface spins contribute to the magnetisation of the particle. Since they are not embedded in a symmetrical structure, this breaking of the symmetry leads to a lower net magnetisation compared to the bulk material [44]. This was proven using Mössbauer spectroscopy of particles, whose core was made of ^{56}Fe and the shell was made of ^{57} Fe leading to a signal loss of the core since only ^{57}Fe contributes to a Mössbauer spectrum. It was seen that the hyperfine fields of the surface had a more linear temperature dependence than the bulk material [2]. Also the different synthesis methods of magnetite nanoparticles lead to large differences in their magnetic properties due to the fact of the obtained varieties of sizes, crystallinity and shapes. The saturated magnetisation values for magnetite nanoparticles found in the literature range from 30-50 emu/g (= 30-50 Am^2kg^{-1}) [5], whereas the bulk material has a saturation magnetisation of 92-100 emu/g (= 92-100 Am^2kg^{-1}) [45].

Magnetic Moment The magnetic moment $\vec{\mu}$ of a magnetic dipole aligns with a given magnetic flux density field, $\vec{B}$. Its magnitude, μ, follows a Langevin function, given by Equation 2.7 [1]:

$$\mu = \mu_{sat} \cdot \mathscr{L}(B) \tag{2.7}$$

with the saturation of the magnetic moment μ_{sat} and the Langevin term given by Equation 2.8:

$$\mathscr{L}(B) = \coth\left(\frac{\mu_{sat} B}{k_B T}\right) - \frac{k_B T}{\mu_{sat} B} \tag{2.8}$$

The net magnetisation can be estimated using the number of magnetic dipoles inside a nanoparticle when interactions between single dipoles are neglected.

Physical and Chemical Interactions

Nanoparticles are subjected to several forces and obtain certain properties which cause them to aggregate and therefore lose their colloidal stability. Especially magnetic nanoparticles are under the influence of four different kinds of potentials, which are either attractive or repulsive potentials. First, the van der Waals potential, W_{vdW}, has to be mentioned which is an isotropic attractive potential acting in a short range. The electrostatic double layer potential, W_{edl}, counteracts these van der Waals potentials and is influenced by the salt content of the suspensions. These two potentials have been theoretically described by the Derjaguin-Landau-Verwey-Overbeek (DLVO) theory [46]. For both potentials the surface potential ψ_0 of the particles and the composition of the solvent is essential. Instead of the surface potential the Zeta potential is often used due to its easier determination.

Taking two identical particles with radius r and a core distance s, the van der Waals and the electric double layer potential for small potentials are [46]

$$W_{vdW} = -\frac{A_H}{6}\left(\frac{2r^2}{s^2-4r^2}+\frac{2r^2}{s^2}+\ln\frac{s^2-4r^2}{s^2}\right) \tag{2.9a}$$

$$W_{edl} = 4\pi\varepsilon\psi_0^2\left\{\begin{array}{ll} \frac{r}{2}\ln\left(1+\exp\left(-\kappa(s-2r)\right)\right) & \text{for } \kappa r > 5 \\ \frac{r^2}{s}\exp\left(-\kappa(s-2r)\right) & \text{for } \kappa r < 5 \end{array}\right\}, \tag{2.9b}$$

with

$$\kappa = \sqrt{\frac{2N_A e^2 I}{\varepsilon_{sol} k_B T}}, \tag{2.9c}$$

where A_H is the Hamaker constant, e is the elementary charge, N_A is the Avogadro constant, κ^{-1} is the Debye-length, I is the ionic strength and ε_{sol} is the dielectric permittivity of the solvent. Both potentials, W_{vdW} and W_{edl}, underlie many assumptions and approximations. One assumption is the equivalence of valence of the ions in the solution (1:1 solution of cations and anions). Furthermore, Equation 2.9c is based on the Debye-Hückel approximation for small potentials. For particles of 20 nm diameter and a Zeta potential of 50 mV in a salt solution of 100 mM ionic strength, one derives the W_{vdW} and W_{edl} and the total potential W_{total} in dependence of the relative distance $(s-2r)/2r$ of the two particles shown in Figure 2.2.

The indirect dependence of the Zeta potential on the ionic strength of the solvent is important to note. If the ion concentration increases, the potential of the electric double layer decreases. This leads to a critical ionic strength where the influence of the electric double layer on the stability of the particles is nearly zero and no repulsive force exists. At this point the particles aggregate. The relations of the Zeta potential can be expanded to the pH of the solvent. In aqueous solutions the iron atoms on the surface of the particles act as Lewis acids and coordinate with water as the lone-pair electron donator. Upon this co-

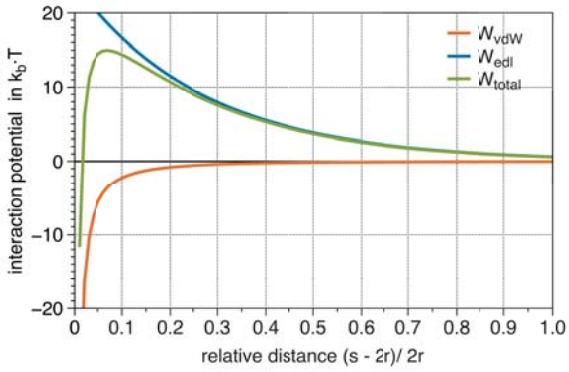

Figure 2.2.: Van der Waals, W_{vdW}, electric double layer, W_{edl}, and total, W_{tot}, interaction potential between two particles in a solution depending on the relative distance of the particles derived from the distance of the cores s and the diameter of the particles $2r$

ordination the water dissociates and the particle gets hydroxyl-functionalised. Due to their amphoteric behaviour the hydroxyl groups can act with bases or acids causing the surface of the particle to be positive or negative depending on the pH of the solution. The point of zero charge (PZC) where the Zeta potential is zero is at pH 6.8 for magnetite nanoparticles [3]. At this pH value the surface charge density is too small and the particles flocculate. Non-naked particles are able to disperse again if the pH is adjusted.

The second couple of attractive and repulsive potentials are the magnetic dipole-dipole interactions and the steric repulsion potential. Magnetic dipole-dipole interactions are special for MNPs and are crucial for their special behaviour. For two particles with magnetic moments $\vec{\mu}_1$ and $\vec{\mu}_2$ they can be described as

$$W_{dd} = \frac{1}{4\pi\mu_0}\left[\frac{\vec{\mu}_1 \cdot \vec{\mu}_2}{s^3} - \frac{3}{s^5}\left(\vec{\mu}_1 \cdot \vec{s}\right)\left(\vec{\mu}_2 \cdot \vec{s}\right)\right], \tag{2.10}$$

with μ_0 being the permeability of vacuum [1]. Taking Equations 2.9a and 2.9b in comparison with Equation 2.10 one can see that the van der Waals potential decreases with the distance between both particles of s^{-2}, the electric double layer with s^{-1} and the magnetic dipole-dipole potential with s^{-3}. This means that the electric double layer has the longest influence in the distance on the interaction of two particles. If the particles are getting closer the van der Waals attraction comes into account and if they are very close and their magnetic moments are aligned the magnetic dipole-dipole potential has to be taken into account as well. For superparamagnetic particles the magnetic dipole-dipole interaction depends on the external magnetic field which induces the magnetic dipole moment. This again depends on the material and on the size of the particle and therefore again on its diameter. If two particles have the same magnetic dipole moment, an external magnetic field is applied and both magnetic dipole moments align parallel to the external field the magnetic force is at its maximum and the particles tend to aggregate. To minimise magnetic dipole-dipole interaction, the dipole-dipole contact energy must be smaller than the

thermal energy k_BT. For ferromagnetic particles, the dipole-dipole interaction energy depends on the particle volume. Hence, the size of the particle must be reduced. As long as the dipole-dipole contact energy is much smaller than the thermal energy, the influence on the colloidal stability of magnetic interaction can be neglected [1]. Accordingly, for particles based on Fe_3O_4 this is the case for a core diameter smaller than approximately 8 nm [1]. Taking calculations from Figure 2.1 into account to maximise the colloidal stability of superparamagnetic nanoparticles their size should be even less than the calculated diameter of approxmiately 20 nm. The assumption would be that particles of diameter sizes of 8-20 nm experience a stronger magnetic dipole-dipole force than smaller particles. Since the magnetic moment increases with the particle volume and therefore also the magnetic dipole-dipole potential this seems to be reasonable. Steric repulsion forces only act in non-naked particles and stabilise the particles in suspension due to the surface characteristics.
Not only their physical interactions depend on their size and surface characteristics, the chemical behaviour of magnetic nanoparticles is also dependent on both parameters. Furthermore, which makes it more complicated, is the fact that both factors are interrelated since the ratio of surface, S, to volume, V, increases as the particle size decreases [2, 47]. For a spherical nanoparticle this is even more evident since:

$$\frac{S}{V} = \frac{3}{r}. \tag{2.11}$$

The crystal structure of magnetite is built up of cubic closed-packed atoms. This would mean that the particles originate from one center atom in the cluster. For a cluster made up of three layers of dense packed shells this means that more atoms are located on the surface than in the core of the particle [48]. This is especially true for particles with a diameter of less than 10 nm. Additionally, their surface to volume ratio is very important for their colloidal stability. Surface atoms are very chemically reactive compared with the same atoms in the core due to their lack of adjacent coordinate atoms. This leads to unsaturated sites or dangling bonds which are willing to react with other chemical partners. A greater surface energy of small nanoparticles is the consequence. The smaller the nanoparticle is, the larger is the effect of the surface energy and hence its contribution to the overall energy of the system. Finally this leads to a lower melting temperature of nanoparticles compared to the bulk material [47, 48].

Requirements for Colloidal Stability

All interactions above have to be considered when searching for measures to stabilise a MNP suspension. In most cases naked nanoparticles are stabilised by applying a coating layer. This layer can be made of monomeric stabilisers, inorganic material or polymers [3]. These coatings mainly work on the steric and/or electrical repulsion forces.
Monomeric stabilisers are usually short chained organic acids or inorganic ions like phosphates, fluoride or sulfate. These ions bind to the freshly precipitated particles, peptise them so they are colloidal stable and provide them with functional groups for further mod-

ifications. Using this method only electrical repulsion is responsible for the stabilisation of the particles and there is a very high dependence on the pH and the ionic strength of the solution [3]. Using nitric acid to peptise magnetite particles one obtains positively charged particles since the hydroxyl groups on the particles surface are protonised in acidic medium [44].
As inorganic material iron oxide nanoparticles have been coated with silica, gold or gadolinium(III) [3]. Silica coatings lead to a decrease in the dipolar coupling between the particles depending on the thickness of the layer. A thin layer will separate the particles and thereby prevent cooperative switching of the magnetic moments [44].
Superparamagnetic particles have been coated with polyethylene glycol (PEG), dextran, chitosan, polyethylene imine and phospholipids to mention a few [20, 49, 50]. All of these polymers and polysaccharides can be further modified with different functional groups like, small molecules, peptides, proteins, aptamers, or even antibodies [6, 49].

All coatings have the four things in common [49]:

- they protect the core of the particle from aggregation or flocculation
- they protect the core from further oxidation processes
- they provide chemical handles for the conjugation of the particles with functional molecules like drug molecules, targeting ligands or reporter moieties
- they protect the particles from non-specific cell interactions when used in a medical approach.

In the context of medical applications the surface coating of magnetic nanoparticles mainly influences their pharmacokinetics, cellular uptake and ability to cross biological barriers, defining their biocompatibility. Macrophages and mainly proliferating cells are able to internalise MNPs when they are smaller than 100 nm [20]. In macrophages this happens via receptor-mediated endocytosis while in proliferating cells, e.g. tumour cells, active internalisation takes place, where the uptake occurs by fluid phase endocytosis in the G_1 cell cycle phase (Figure 2.3) [51, 52].

It has also been shown that the uptake seems to depend on the size of the particles. Particles, which are smaller than 50 nm, need to cluster together on the cells surface for endocytosis. One particle alone will not produce enough ATP in the cell, since only one or few receptors will be targeted. Hence, the triggering of a signal cascade, so that the cell's membrane will wrap around the particle, will not occur [49, 53].
Superparamagnetic iron oxide nanoparticles are highly captured in the liver (Kupffer cells), the spleen and the lymph nodes [20, 39, 52, 54]. Depending on their size, the way of clearance from circulation differs. Small particles (<5 nm) are mainly renally secreted as was shown by Choi et al. By using zwitterionic cysteine coated quantum dots the clearance of the nanoparticles from the body depending on their size and surface charge was followed [55]. Particles with the size of 10 to 180 nm are taken up by phagocytotic cells such as Kupffer cells in the liver, macrophages but also microglia in the brain. Their primary elimination from the blood circulation occurs in the reticuloendothelial system [56]. However,

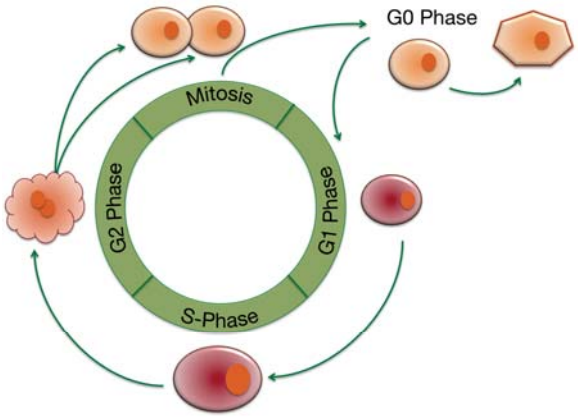

Figure 2.3.: Schematic drawing of the phases of the cell cycle. After the cell division in the mitosis the cells can progress to phase G0, where they can differentiate or re-enter the cell cycle into phase G1. In the G1 phase the cells are prepared for the synthesis of DNA and DNA replication, which will take place in phase S. In phase G2 the set of chromosomes is doubled and the cells are organising themselves for cell division in mitosis.

the incorporation into hemoglobin of erythrocytes has also been reported [57].
Importantly, it still needs to be elucidated, how cells can handle the overdose of iron oxide, which is present right after the injection of a superparamagnetic contrast agent [58].
Besides the size of MNPs, their uptake depends on other factors like their chemical composition, shape, surface structure and charge, aggregation and solubility, but also on the presence of functional groups or other chemicals [59]. Nevertheless, it has to be mentioned that, the smaller the particles, the more reactive is their surface leading to a higher concentration of reactive oxygen species and therefore free radicals in the cells. This in turn causes oxidative stress, inflammation and finally damage to proteins, membranes and DNA [51].

2.1.2. Synthesis of Magnetic Nanoparticles

The synthesis of MNPs is based on the process of nucleation and growth. Nucleation is a common reaction in nature including the formation of clouds or the bubbling of carbon dioxide out of a carbonised beverage. Since the last century work has been done to understand the kinetics and thermodynamics of condensation of liquid from the vapor phase and of the precipitation and crystallisation of solids from solution [60]. Since, the optical, electrical and catalytic properties of particles at the nanoscale are very much influenced by their shape and size, it is very important to understand the mechanisms of nanoparticle formation. This again helps to gain control over the properties of the manufactured clusters and, moreover, to tune the reaction conditions to obtain nanoparticles of the desired size and shape [60, 61].

Synthesis - Reaction Theory

For the preparation of nanoparticles using precipitation methods there are two theories for the nucleation process to be considered: first the principle of LaMer and Dinegar, second the classical nucleation theory reflecting on the thermodynamics and the kinetics of the nucleation reaction.

LaMer and Dinegar introduced in 1950 the basic principles for the formation of colloidal nanocrystals in a liquid phase [62]. Their model was the formation of polydisperse sulfur partiles, known as "milk of sulfur", since the solution turns opaque during the reaction.

According to their model (Figure 2.4), first, zero-valence atoms of the chosen element, sulfur in their case, have to be provided continuously through an appropriate chemical reaction to maintain a sustainable growth of the particles,

$$Na_2S_2O_3 + H_2SO_4 \longrightarrow S^0 + SO_3^- \tag{2.12}$$

$$n\ S^0 \longrightarrow S_n^0.$$

Even when the saturation concentration, c_s, is reached the elemental sulfur can not spontaneously condense into first solid nuclei (Figure 2.4). The concentration of the sulfur has to reach a critical concentration, c_{crit}, for the sulfur precursors to condense into nuclei since they do not condense into solids spontaneously. This is due to the fact that the formation of a new solid phase in a liquid environment is an energy-consuming process [61].

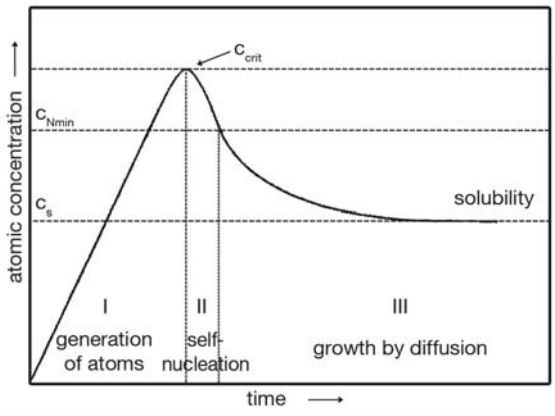

Figure 2.4.: Schematic presentation of the LaMer model describing the nucleation and growth of sulfur nanoparticles as a function of concentration of monomers before and after the nucleation and the time (adapted from [61] and [62])

After this point, the growing of the nuclei can occur at concentrations less than c_{crit} but higher than c_s, since he growing process is less energy consuming compared to the formation of nuclei. Therefore, the nucleation and growth steps are two processes relatively

separated from each other by the concentration of the monomers. New nucleation over time only occurs at precursor concentrations higher than c_{Nmin}. Below this concentration, after reaching c_{crit}, the system is still supersaturated leading to the growth of discrete particles by diffusion of sulfur precursors to the stable nuclei. Thus, once region III is reached, the concentration of the precursors represents a balance between their rate of production due to the chemical reaction (Reaction 2.12) and their removal by the diffusion processes to the nuclei. The rate of growth is therefore controlled by the rate of the chemical reaction and the two steps of the reaction, nucleation and growth, can be controlled by tuning the concentration of the sulfur precursors. The important aspect is that the formation of the zero-valence sulfur, or any other element like silver, has to be applied continuously by a reduction reaction. Therefore, this theory is of less importance for the formation of iron oxide magnetic nanoparticles using a sol-gel or co-precipitation method, where the nucleation is caused by the addition of one chemical compound leading to a nucleation burst. In these cases no continuous supply of precursors is provided to reach c_{crit} for the start of the nucleation. This theory can be applied to applications like the formation of semiconductor nanocrystals, the preparation of nanocrystals with a core-shell structure and colloidal silver particles [48, 61, 63, 64].

The classical nucleation theory regards the nucleation reaction as a chemical reaction in which solvated precursors are converted into a solid-state crystalline product. As a chemical reaction this process can be devided in thermodynamic and kinetic aspects [61]. First the thermodynamic aspect will be discussed. There are three types of nucleation [48]:

- **homogeneous nucleation:** solute molecules within a liquid combine to form nuclei without a present solid interface,
- **heterogeneous nucleation:** the nucleus forms on an existing surface of a different material (vessel wall, stirrer),
- **secondary nucleation:** occurs on a pre-existing "seed" of the same material or by aggregation of particles (core-shell clusters).

In the case of the precipitation of nuclei out of a supersaturated solution homogeneous nucleation occurs. Since the supersaturated solution is not stable in energy, the thermodynamics are the driving force of homogeneous nucleation [48]. The overall free energy change, ΔE, contains two competitive terms: one describes the formation of a new volume, or the lattice formation, and is exothermic, the other describes the creation of a new interface between the particle and the solvent and is endothermic. For spherical particles the expression for the free energy change is

$$\Delta E = -\frac{4}{V_m}\pi\left(\frac{d}{2}\right)^3 k_B T ln(S) + 4\pi\left(\frac{d}{2}\right)^2 \sigma_S, \tag{2.13}$$

where V_m is the volume 1 mol of the solid occupies (= molar volume), S the expression for the supersaturation state, d is the diameter of the nucleus and σ_S is the surface free energy

per unit area [48]. The supersaturation state S can be expressed as n/n^{sat}, where n is the mole fraction of the precursor present in solution and n^{sat} the mole of the precursor in a saturated solution. Alternatively, this term can be written for concentrations c/c_{eq}, where c is the concentration of the precursor and c_{eq} is the solubility or equilibrium concentration of the precursor. For the nucleation of droplets from vapor this expression can be written in terms of pressure as p/p_{eq} as well [60].

Taking this expression S has to be > 1, otherwise no precipitation will occur. Figure 2.5 depicts the dependence of the change in free energy, ΔE, on the diameter of the forming nucleus, d.

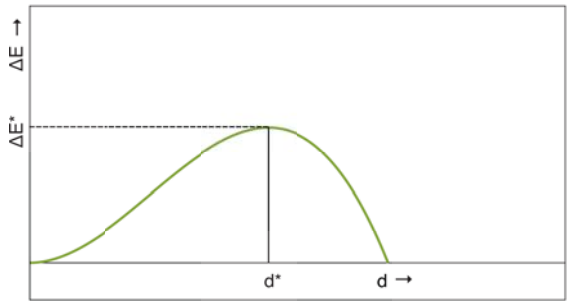

Figure 2.5.: Dependence of the free energy change ΔG, on the diameter of the forming nucleus, d; The maximum of the curve indicates the critical free energy ΔG^* and the critical diameter of the nucleus, d^* (adapted from [60]).

The maximum of the curve gives the critical diameter, d^*, of the nucleus. Is the nucleus smaller than d^* the nucleus will dissolve and growth is unfavourable. For nuclei larger than d^* the nucleus will grow. Since the size of the nucleus is proportional to the number of atoms in the nucleus one can exchange d^* for n^* with n being the number of atoms in the nucleus [60]. In the application of the formation of magnetite MNPs this means, that at a constant temperature and at a given concentration of the iron (II) and iron (III) salts (the precursors), the diameter of the nuclei will either shrink or grow, depending on whether it is smaller or bigger than d^*.

The kinetic aspect of the classical nucleation theory also considers the concentration of the precursors and the transport from the precursor to the particle of a certain size. It correlates the size of the nucleus with the amount of precursor present in the solution. Figure 2.6 depicts the diffusion layer of a precursor around an already formed nucleus. Here, c_b is the bulk concentration of the precursor, c_i the precursor concentration at the interface, c_e the solubility of the nucleus depending on its radius r, and δ is the diffusion layer [65].

The rate of nucleation, J, that means the precursor flux to the particle, depends on the distance, $r+\delta$, between the precursor and the particle, on the concentration, c, of the precursor and on the self diffusion coefficient, D (Figure 2.6 and Equation 2.15). This aspect has been examined by Peng et al. and Sugimoto thoroughly [64, 65].

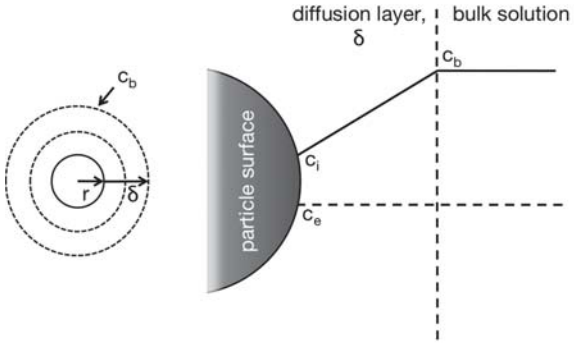

Figure 2.6.: Schematic drawing for the kinetics of the classical nucleation theory including the model of the transport of the precursor to the particle; c_b is the bulk concentration of the precursor; c_i the precursor concentration at the interface; c_e the solubility of the nucleus depending on its radius r (adapted from [65])

The flux of particles is expressed by Fick's first law as

$$\vec{J} = -D \text{ grad } c. \tag{2.14}$$

In the case of the flux of the precursor to the particle through the diffusion layer, where $c_b > c_i$, and due to the spherical symmetry of the particle Fick's law can be written as

$$J = 4\pi r^2 D \frac{dc}{dr}. \tag{2.15}$$

If the diffusion of the precursor to the nucleus is in a steady state, J is constant irrespective of the distance $r+\delta$. Solving the ordinary differential equation within the boundary conditions of r and $r+\delta$ gives

$$J = \frac{4\pi D r(r+\delta)}{\delta}(c_b - c_i). \tag{2.16}$$

After the diffusion process the surface reaction taking place can be written as,

$$J = 4\pi r^2 k(c_i - c_e), \tag{2.17}$$

a simple first-order reaction postulated, where k is the rate constant. Taking Equations 2.16 and 2.17 together it follows that,

$$\frac{c_i - c_e}{c_b - c_i} = \frac{D}{kr}\left(1 + \frac{r}{\delta}\right) \tag{2.18}$$

For $D \ll kr$ the reaction is in the **diffusion controlled regime** and $c_i \approx c_e$. In this case, the particle growth is controlled by the monomer diffusion to its nucleus. Thus, Equation 2.16 leads to

$$J = \frac{4\pi Dr(r+\delta)}{\delta}(c_b - c_e) \tag{2.19}$$

and since J can also be related to dr/dt as

$$J = \frac{4\pi r^2}{V_m}\frac{dr}{dt}, \tag{2.20}$$

Equations 2.19 and 2.20 can be combined to

$$\frac{dr}{dt} = DV_m\left(\frac{1}{r} + \frac{1}{\delta}\right)(c_b - c_e). \tag{2.21}$$

Equation 2.21 states that *dr/dt* is lowered when r increases. If $(c_b - c_e)$ can be regarded as constant, the size distribution becomes narrower with particle growth.

If $D \gg kr$ in Equation 2.18 then $c_b \approx c_i$ and the growth is in the **reaction-controlled regime** [65]. From Equations 2.17 and 2.20 can be derived that:

$$\frac{dr}{dt} = kV_m(c_b - c_e). \tag{2.22}$$

Therefore *dr/dt* is independent of the radius for the reaction-controlled regime and the standard deviation of the size distribution remains constant during the growth [65]. If the growth rate of the nuclei on the surface of a nucleus is faster than the nucleation rate, the whole surface of the nucleus will be covered by a new solid layer. This means that the growth rate is not limited by the diffusion process of the precursor to the nucleus, but by the surface reaction of the precursors. One can say that in the case of magnetite nanoparticles the reaction of the iron and oxygen ions with the existing nuclei goes faster than the establishing of new nuclei. Since this reaction depends on the surface of the particles *dr/dt* is proportional to the surface area of the particle

$$\frac{dr}{dt} = k'r^2, \tag{2.23}$$

where k' is the rate constant. According to this the size distribution must get broader with time, since smaller particles grow slower and bigger particles grow faster. However, this mechanism holds only true for the early stages of particle growth, since the radius would reach infinity in an infinite time [65].

If one looks closely, the term $(c_b - c_e)$ in Equation 2.21 is not independent of the particle size. c_e is the solubility of the particle as a function of its radius. Since the Gibbs-Thomson equation states the relationship between the equilibrium vapor pressure around a circular island and the curvature of the island it is often used in the context of nucleation theory. In this case the equilibrium vapor pressure can be substituted by c_e and the circular island by the particle and one derives

$$c_e = c_\infty \exp \frac{2\sigma V_m}{rRT} \tag{2.24}$$

where c_∞ is the solubility of the solid mit infinite dimension, σ is the specific surface energy and R is the gas constant.

If $2\sigma V_m / rRT \ll 1$, c_e and c_b can be approximated as:

$$c_e \cong c_\infty \left(1 + \frac{2\sigma V_m}{rRT}\right) \tag{2.25}$$

$$c_b \cong c_\infty \left(1 + \frac{2\sigma V_m}{r^* RT}\right) \tag{2.26}$$

with r^* being the critical radius. Taking Equations 2.21, 2.25 and 2.26 together for a typical diffusion-controlled growth with an infinite diffusion layer ($\delta \to \infty$)

$$\frac{dr}{dt} = \frac{K_D}{r}\left(\frac{1}{r^*} - \frac{1}{r}\right), \tag{2.27}$$

with $K_D = \dfrac{2\sigma D V_m^2 c_\infty}{RT}$.

Under constant r^* one obtains

$$\frac{d\Delta r}{dt} = \frac{K_D \Delta r}{\tilde{r}^2}\left(\frac{2}{\tilde{r}} - \frac{1}{r^*}\right), \tag{2.28}$$

where a narrow size distribution is assumed, while Δr is the standard deviation and $\tilde{r}$ is the mean radius of all particles [65].

If $\tilde{r} < 2r^*$ the standard distribution increases with the time for $\dfrac{d\Delta r}{dt} > 0$ in Equation 2.28, leading to a broadening of the particle size distribution under low supersaturation of the precursor [65]. In contrast if $\tilde{r} \geq 2r^*$, then Equation 2.28 is smaller or equal zero, which means the standard deviation becomes smaller with the time, leading to the focusing of the particle size distribution.

This holds true when the supersaturation of the precursor is kept high in comparison with the solubility of the particles of mean radius. Thus, ignoring the Gibbs-Thomson effect,

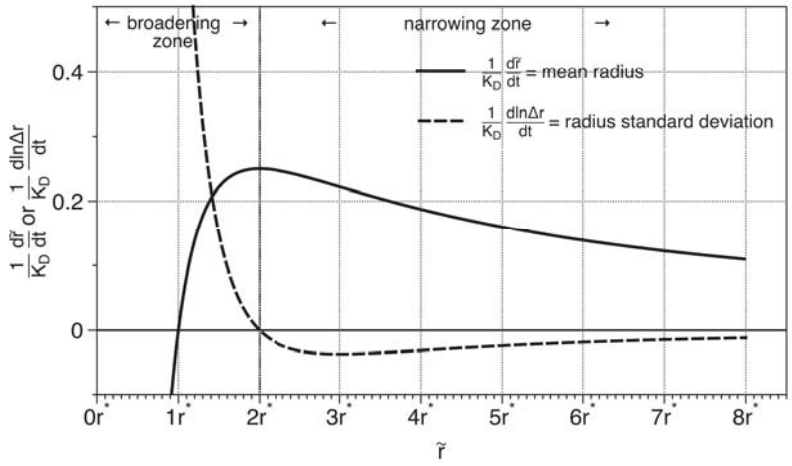

Figure 2.7.: Evolution of the mean particle radius ($\frac{1}{K_D}\frac{d\tilde{r}}{dt}$) and the standard deviations ($\frac{1}{K_D}\frac{dln\Delta r}{dt}$) of the particle radius over time plotted as a function of $\tilde{r}$ in the case of diffusion-controlled growth with an infinite diffusion layer; For $\tilde{r} < 2r^*$ the size distribution broadens and for $\tilde{r} \geqq 2r^*$ it narrows (adapted from [65]).

under the diffusion-limited growth the bulk concentration of the precursor, c_b, should be kept just below the critical supersaturated concentration, c_{crit}, to promote a monodisperse diffusion-controlled growth [65]. Figure 2.7 shows the relationship between the critical radius, r^*, and Equations 2.27 and 2.28.

For a simple first-order reaction-controlled growth Equations 2.22, 2.25 and 2.26 may be written as:

$$\frac{d\Delta r}{dt} = K_R\left(\frac{1}{r^*} - \frac{1}{r}\right), \tag{2.29}$$

with $K_R = \dfrac{2\sigma k V_m^2 c_\infty}{RT}$.

Accordingly, $\dfrac{d\Delta r}{dt}$ can be written as

$$\frac{dr}{dt} = \frac{K_R \Delta r}{\tilde{r}^2}. \tag{2.30}$$

This means that for any r Equation 2.30 is positive and some broadening of the size distribution will always take place for a reaction-controlled growth due to the Gibbs-Thomson effect. Furthermore, the broadening effect is unavoidable since $\frac{d\Delta r}{dt}$ is independent of r^* no matter how high the supersaturation of the precursor.
For the model of LaMer et al. the size of the nanoparticles formed can be controlled by the concentration of the precursor produced, if the temperature of the reaction system is

constant [62]. For the classical nucleation theory one can say, that if the concentration of the precursor is constant during the reaction, the cluster size can be regulated by changing the temperature and therefore the free energy change of the system.
In addition, the process of Oswald-Ripening has to be mentioned which is also called coarsening. It usually occurs after the growth phase of the particles. In this case larger particles grow at the expense of small particles. Smaller particles tend to dissolve due to their high surface tension energy which leads to the rise of precursor concentration in the solution. The so new established precursors are available for the decomposition on the bigger particles [66]. To circumvent this problem it is important to obtain a monodisperse size distribution right from the beginning by controlling the nucleation and the growth period.
Thus, if one wants to obtain monodisperse particles with a uniform particle shape, one has to control the kinetics of all steps of synthesis: nucleation, growth, coarsening and the last step, the agglomeration of formed magnetic nanoparticles. All aspects mentioned above have to be considered simultaneously, which makes the synthesis of magnetic nanoparticles very complex compared to the preparation of bulk metals and bulk metal oxides [67]. Taking all aspects together for the co-precipitation of iron salts to obtain iron oxide magnetic nanoparticles, which will be explained later, the goal for a monodisperse size distribution is to have a very short nucleation burst followed by a slower growth of the existing nuclei [48]. The short nucleation burst is achieved in this work by the rapid addition of NaOH to the system under vigorous stirring to elevate the pH of the solution rapidly, for magnetite to precipitate. Afterwards the solution is kept at constant temperature and further stirring to let the nuclei grow to the desired size and no additional precursors are added to stay in the grow regime. The concentration of the precursors stays therefore under the critical concentration, c_{crit} for nucleation and the precursors already formed can add to the existing nuclei. So the time of the nucleation step has to be very short in comparison with the growth process to allow size focusing over time. In the protocol used in this work the size of the growing particles is also controlled by the used solvent. Diethylene glycol serves as solvent and also as stabilizer. Its high boiling temperature leads to better crystallinity of the particles and therefore to higher magnetisation values. Furthermore the hydrophilic diethylene glycols act as ligands serving for the first coating, giving a better stability of the particles preventing them from aggregation. It was also shown that the use of polyols in the preparation of magnetite nanoparticle leads to a narrower size distribution compared to preparations in aqueous environments.

Synthesis - Methods

There are different methods to obtain nanoparticles of different sizes and shapes. In the following the main routes are listed.

Co-precipitation of Fe^{3+} and Fe^{2+} salts in aqueous solution is the most efficient way to obtain magnetic iron oxide nanoparticles [39, 3, 6, 68]. It has the advantage of producing large amounts of iron oxide particles, but the severe draw back of a low control over the

particle size contribution. To find the optimum parameters of concentration and nature of the precursors, the pH the ionic strength, the stirring speed, the amount of nitrogen gas to bubble through the solution, the right temperature and the right base for precipitation or the right amount of cations added to stabilise the produced particles as well as the reaction time have to be determined [3, 68, 69].

Sol process This process is mainly used to obtain semiconductor nanocrystals. The reactions are taking place in a high-boiling coordinating solvent and the nucleation phase is strictly separated from the growth phase [48]. The particles are harvested by their precipitation due to the adding of a poor solvent [65].

Sol-gel and polyol reactions are comprised of different processes following each other. First precursors have to hydrolyse and condensate to form a sol. This sol is further subjected to further condensation leading to an inorganic polymerisation forming a gel. Since all reactions are carried out at room temperature the final crystalline state of the particles is obtained by heat treatments leading to drying and thermal decomposition of the gel [3, 48]. Polyol methods can be counted to the sol-gel reactions in which the solvents are polyols like diethylene glycol. These processes harvest a large amount of iron oxide particles with defined shapes, a good control of the size distribution and have the advantage that the polyol solvents also act as stabilisers for the produced particles. The elevated temperature leads to higher crystallinity of the formed particles. However, comparable to the co-precipitation method parameters like the solvent, the temperature, the pH, the concentration and nature of the precursors and the agitation level have to be adjusted for best results [3].

Micelles are used to obtain a narrow size distribution and small sizes of nanoparticles. For this way of synthesis, surfactants are dispersed in water or organic media leading to dispersed normal micelles or reversed micelles, respectively. Reversed micelles contain a constraint volume of water in which the reaction for the preparation of the nanoparticle can take place. Depending on the ratio of surfactant to oil and to water different shapes of nanoparticles can be obtained [48]. The biggest drawback of this method is the low amount of particles that can be produced and the costs of the chemicals for the micelle production.

Hydrothermal and High-temperature Reactions Hydrothermal reactions are performed in aqueous environment in reactors or autoclaves under a pressure higher than 138 bar and temperatures above 200°C. These reactions involve the hydrolysis and oxidation or the neutralisation of mixed metal hydroxides [3]. A high level of size and shape control as well as monodispersity can be obtained by thermal decomposition methods. Using this method iron organic precursors are decomposed using organic solvents and surfactants

[3, 6, 9, 48, 49]. The thermal decomposition methods have the disadvantage that only low amounts are produced. Furthermore, the particles are made in organic solvents but have to be used in aqueous environment, which means that their surface has to be treated for them to be stable in aqueous solutions [3]. During these transformation processes they often aggregate and of a low amount of particles harvested even more is lost.

Pyrolysis is the process called when chemical precursors decompose to a solid compound and the unwanted side products evaporate away. Usually a wide range of sizes is obtained leading to the development of modifications to obtain uniform sizes and shapes. Using this method different kinds and shapes of nanoparticles can be obtained. These include metals, metal oxides and semiconductors as nanowires, nanorods and triangular nanoprisms [4, 48].

Vapour Deposition For this process the precursors are vapourised and subjected to a vapour deposition reactor where they adsorb on a substance which is kept at elevated temperatures. Here they will either decompose or react with other gases and vapours to form the desired nanoparticles. This process can be divided into chemical and physical vapour deposition, depending on the preparation of the vapour [48].

Flow Injection Synthesis is a method to prepare magnetite nanoparticles using flow injection synthesis techniques. The reagents are continuously or segmentedly mixed under a laminar flow regime in a capillary reactor [3].

Light-induced Shape Change mechanisms of metal nanorods have also been reported. Prepared nanoparticles are subjected to laser pulses leading to their shape transformation. Applying this method nanodots have been made from nanorods or nanodisks from nanoparticles [48].

For the last two methods special apparatus for the preparation of nanoparticles is needed and often these methods are not suitable for the preparation of large amounts of spherical iron oxide nanoparticles.
The variety of preparation methods leads to a variety in the properties of the obtained iron oxide particles. The outcome are particles which could have the same size range but have different magnetisation values due to higher crystallinity [5]. This makes it even more important to find methods of the metrology of MNPs to be able to compare literature data and also to be able to compare self-manufactured MNPs. The particles manufactured in this thesis are prepared using the polyol method together with the co-precipitation method. The diethylene glycol acts as the solvent and also as a stabiliser coating the particles *in situ*. The high temperature which can be obtained this way leads to a better crystallinity and therefore higher magnetisation compared to general aqueous co-precipitation [3].

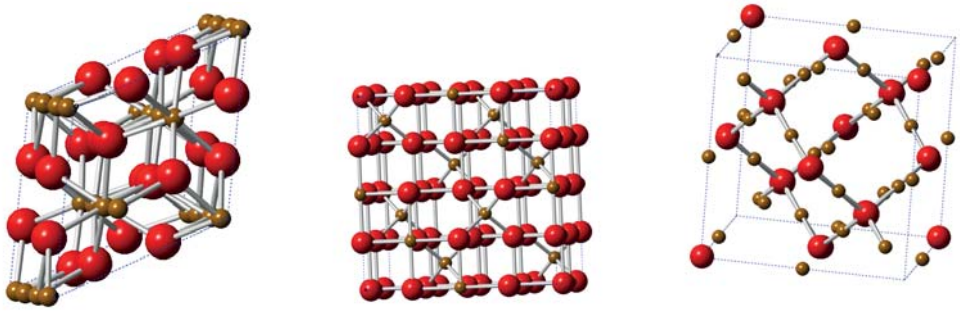

(a) α-Fe_2O_3 (haematite) (b) γ-Fe_2O_3 (maghemite) (c) Fe_3O_4 (magnetite)

Figure 2.8.: Crystal structures of α-Fe_2O_3 (haematite), γ-Fe_2O_3 (maghemite) and Fe_3O_4 (magnetite) in comparison; red = oxygen; brown = iron

2.1.3. Magnetic Nanoparticle Chemistry

Iron Oxide Chemistry

Iron is the second most abundant element on earth following aluminium and the fourth most in the earth shell. The important iron ores are haematite (α-Fe_2O_3), magnetite (Fe_3O_4), limonite ($FeO(OH)\cdot xH_2O$), and siderite ($FeCO_3$). Subjected to humid air the white shiny metal is quickly oxidised to iron (III) hydroxides. This oxidation process leads not to a preservative layer, since it splinters from the bare metal giving space for new reaction processes [70].
There are three different types of iron oxides, FeO, Fe_2O_3 and Fe_3O_4, which all tend to form non stoichometric phases. Iron (II) oxide (FeO) is unstable at lower temperatures and dissociates into Fe and Fe_3O_4. It is a black, pyrophorous substance with a NaCl structure in its crystalline phase. The structure of the brown, water containing iron (III) oxide FeO(OH) depends on its formation. This can be done either by the hydrolysis of iron (III) chloride solutions at higher temperatures or through the oxidation of iron (II) hydroxide. At higher temperatures FeO(OH) turns into the red brown α-Fe_2O3, haematite (Figure 2.8 (a)). Another form of iron (III) oxide, the γ-Fe_2O_3, maghemite (Figure 2.8 (b)), is formed by the gentle oxidation of Fe_3O_4, magnetite, or the heating of γ-FeO(OH), lepidokrokite. Both iron (III) oxides differ in their crystal structure. Haematite has an corund crystalline structure where the oxygen ions are tightly packed in a hexagonal constitution and the iron (III) ions are located in the octahedral interstice (Figure 2.8 (a)). Maghemite shows a cubical organisation of its oxide ions in which the iron (III) ions are randomly located in the octahedral or tetrahedral cavities (Figure 2.8 (b)). Both iron (III) oxides are reddish brown.
Fe_3O_4, magnetite, is a mixed Fe(II)-Fe(III) oxide (Figure 2.8 (c)). The iron (II) ions are located on the octahedral spaces whereas one half of the iron (III) ions are arranged on the tetrahedral spaces and the other half in the octahedral interstice of the cubical tightly packed oxygen ions. Its crystals are black coloured.

All crystal structures of iron oxides have in common the tight cubical constitution of the oxide ions. The differences are the amount and ratio of the iron ions. If all octahedral interstices are occupied by iron (II) ions, one obtains the optimal structure for FeO. If only a small amount of these iron (II) ions is substituted by iron (III) ions the defect structure of the iron (II) oxide will be obtained. Fe_3O_4 is formed, if this substitution progresses until two thirds of all iron ions are iron (III) and their arrangement is tetrahedral. The substitution of the residual iron (II) ions with iron (III) ions leads to γ-Fe_2O_3, maghemite. The easy conversion of one iron oxide into the other is possible because no change has to occur in the crystal structure. Only the rearrangement of ions is necessary in their tetrahedral and octahedral coordination. This is also the reason for their lack of stoichiometric composition and the complexity of the FeO system.

Fe^{2+} Ions form in aqueous solutions in the absense of other complexing substances hexacoordinated aqua complexes $[Fe(OH_2)_6]^{2+}$, which are pale greenblue in color. Due to the potential of Fe^{3+}/Fe^{2+} (0.771 V), molecular oxygen can transform iron (II) into iron (III) ions under acidic conditions:

$$Fe^{2+} + \tfrac{1}{2}O_2 + 2H^+ \rightleftarrows 2Fe^{3+} + H_2O \qquad E^0 = 0.46\ \text{V}$$

In basic solutions this oxidation potential is even more favourable:

$$\tfrac{1}{2}Fe_2O_3 \cdot 3H_2O + e \rightleftarrows Fe(OH)_2 + OH^- \qquad E^0 = -0.56\ \text{V}$$

Fe^{3+} Ions are hydrolysed and/or form complexes in water:

$$[Fe(H_2O)_6]^{3+} \rightleftarrows [Fe(H_2O)_5(OH)]^{2+} + H^+$$
$$[Fe(H_2O)_5(OH)]^{2+} \rightleftarrows [Fe(H_2O)_4(OH)_2]^{+} + H^+$$
$$2[Fe(H_2O)_6]^{3+} \rightleftarrows [Fe(H_2O)_4(OH)_2Fe(H_2O)_4]^{4+} + 2H^+$$

The direction of the equilibrium depends on the formation constant of the metal hydroxo complex. To initiate the formation of polynuclear clusters of metal hydroxo complexes, the equilibrium needs to be shifted to the right of the equation. This can be done by neutralising the formed acid. The so formed clusters act as seeds for the further condensation of the metal hydroxo complexes until they get large enough to precipitate as hydrated oxides. Further dehydration of these complexes leads to the formation of crystalline oxides [67]. The process of condensation of aquohydroxo complexes is called olation and can be described as

$$[Fe(H_2O)_6]^{3+} + [Fe(H_2O)_5(OH)]^{2+} \leftrightarrows [Fe(H_2O)_5(OH)Fe(H_2O)_5]^{5+} + H_2O.$$

Due to the acidity of the remaining hydroxo ligands the ionisation and condensation of the complexes can proceed further until oxolation occurs:

$$[Fe(H_2O)_5(OH)Fe(H_2O)_5]^{5+} \rightleftarrows [Fe(H_2O)_5(O)Fe(H_2O)_5]^{4+} + H^+$$

If ammonia is added to this iron (III) solution, amorphous iron (III) hydroxide will form and a reddish brown gel will precipitate. Since there is no evidence of the existence of $Fe(OH)_3$, the substance obtained should rather be described as an aqueous iron (III) oxide, $Fe_2O_3 \cdot nH_2O$ [70]. This process is very rapid and finally colloidal gels are formed that contain iron oxides. The overall reaction can therefore be described as

$$2[Fe(H_2O)_6]^{3+} \rightleftarrows Fe_2O_3 + 9H_2O + 6H^{5+}.$$

The condensation of ferrous-complexes (Fe^{2+}) occurs above pH 6 and for ferric-complexes (Fe^{3+}) already at pH above 1. For ferrous- complexes polycationic species have rarely been reported [71].

Hydrolysis of Mixed Ferric-Ferrous Compounds in Aqueous Solutions As mentioned above, the formation of specific iron phases depends on many aspects and one is the ratio of the ferrous and ferric ions in the system. If Fe^{2+} is in two-fold higher molar excess than Fe^{3+}, Fe_3O_4 (magnetite), will be co-precipitated in aqueous solutions. An important property of magnetite is the fast electron hopping between the iron ions in the octahedral sublattice structure. Already in the formation process of the spinel at room temperature, this electron transfer between ferrous and ferric ions is fundamental. It leads to local rearrangements and forces spinel ordering [71]. With the optimal molar ratio being 0.5 the mean particle diameter of 2-12 nm can be accomplished by the optimal conditions of the medium, the pH and the ionic strength, I, in the reaction system. These conditions should be pH 8.5 to 12 and 0.5 to 3 M for the ionic strength [3, 5, 68]. With these conditions magnetite particles can be obtained:

$$Fe^{2+} + H_2O \xrightarrow{\text{deprotonation}} Fe(OH)_x^{2-x}, \tag{2.31}$$

$$Fe^{3+} + H_2O \xrightarrow{\text{deprotonation}} Fe(OH)_y^{3-y}, \tag{2.32}$$

$$Fe(OH)_x^{2-x} + Fe(OH)_y^{3-y} \xrightarrow[\text{pH}>9]{\text{oxidation,dehydration}} Fe_3O_4. \tag{2.33}$$

The overall reaction for the co-precipitation of iron salts is:

$$Fe^{2+} + 2\,Fe^{3+} + 8\,OH^- \longrightarrow Fe_3O_4 + 4H_2O.$$

Under the presence of oxygen magnetite is further oxidised to maghemite [5]:

$$Fe_3O_4 + 4.5\,H_2O + 0.25\,O_2 \longrightarrow 3\,Fe(OH)_3 \Longleftrightarrow Fe_2O_3 \cdot nH_2O.$$

Magnetite is also transformed into maghemite in acidic conditions [3]:

$$Fe_3O_4 + 2\,H^+ \longrightarrow \gamma\,Fe_2O_3 + Fe^{2+} + H_2O.$$

Depending on the pH of the solution different electron and ion transfers are happening. Under acidic and anaerobic conditions the iron (II) ions are desorped from the surface as hexa-aqua complexes leading eventually to the dissolving of the particle. Under alkaline conditions the magnetite on the surface is oxidised. This involves the migration of the iron

(III) ions through the lattice to the surface of the particle leaving cationic vacancies in the lattice structure [3].

Taken together, the chemistry of iron oxides is very complex. Due to the high electron mobility in the spinel of the magnetite, magnetite nanoparticles have an interesting surface chemistry, and are subjected to an interfacial transfer of ions and/or electrons. This leads to their high sensitivity to oxidation and therefore transformation into maghemite as seen above. In consequence, the synthesis needs to be not only pH, temperature and ionic strength controlled but also strictly anaerobic.

Silica Chemistry

To prevent the further oxidation of the iron oxide nanoparticles and to improve the stability of the particle suspension, MNPs are coated with various kinds of organic materials. Coatings have the ability to introduce steric and different kinds of charge repulsion effects between the particles. First silica particles have been introduced in 1968 by Stöber *et al.*. They produced monodisperse nano- and microparticles made of a silica alkoxide monomer [72]. Later on, this production was developed further by the introduction of silane modifications in the silica coatings by using alkyl silanes with different functional groups ($SiR_3(CH_2)_nX$: R = Cl, OCH_3, OC_2H_5, etc; n = 3-17; X = CH_3, CN, CO_2CH_3, etc.) [73]. The introduced silane compounds contained also alkoxy silane groups. These alkoxy groups get hydrolysed and become reactive silanols, which can condense with the silanol -OH groups on the silica particle surface to form siloxane linkages (Figure 2.9) [74]. These groups provide a silica surface with chemical handles for modification with biomolecules making them more attractive for bioapplications [75, 76].

The reaction depicted in Figure 2.9 can be catalysed by heat and the presence of water in which the silanols are formed from the alkoxy groups. The best stability of silica is obtained in neutral or acidic pH conditions with 0.05 M NaCl [74].

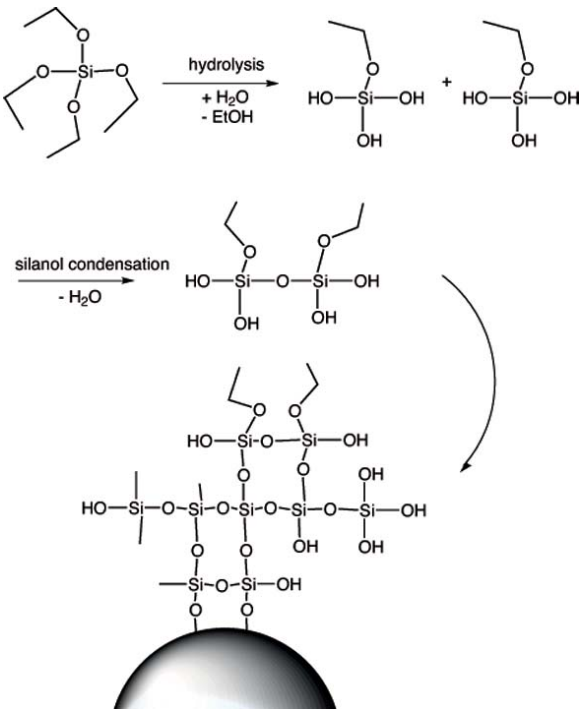

Figure 2.9.: Condensation of silane compounds, e.g. tetraethoxysilane, to form silica coatings

Techniques for Functionalisation

For the further usage of MNPs a functionalisation with either catalytic active species, drugs, specific binding sites or other functional groups is necessary. Sometimes the functionalisation of nanoparticles is also called vectorisation, if the functionalisation is carried out with specific vectors for biological targets, like antibodies, aptamers and so forth [3]. This can be accomplished in various ways depending on the reactive groups provided by the coating on the surface of the MNP. There are two strategies for functionalisation, first by the establishment of physical interactions and second by introducing a covalent bond.
Physical interactions rely on electrostatic, hydrophilic/hydrophobic or affinity interactions. These strategies for functionalisation are fairly easy to accomplish but have the drawback of being easy to break due to changes of the nature, pH or ionic strength of the solvent.
Covalent linkage strategies are more complex but provide a stable bond between the particle and its functionalisation. For these linkages functional groups like amino, carboxylic acids, aldehyde, alkyne, active hydrogen or sulfhydryl groups or mixtures of them have to be provided on the surface of the particle. This can already be accomplished in choosing the right coating material. PEG as well as silanes are available with different chemical handles for further functionalisation [49].
There are a variety of direct chemistries for each different functional group and a few will be mentioned. Another way of introducing a covalent bond is the use of bioconjugate reagents, which can be zero-length crosslinkers, like N-(3-Dimethyl-aminopropyl)-N′-

ethylcarbodiimide hydrochloride (EDC) (Figure 2.10) or the Schiff-Base formation following a reductive amination. They can also be bifunctional crosslinkers having the ability to either have the same reactive group on both ends (homobifunctional), or different reactive groups (heterobifunctional). Using crosslinkers, spacers of various lengths between the particle and its functionalisation can be introduced [74].
For direct chemistries active hydrogens on the particle surface can be coupled with amine groups on the target through the Mannich reaction [49]. Aldehyde groups can be reacted with amine or hydrazide groups to form Schiff-Bases which can be reduced to form a secondary amino bond [74]. This technique is one technique to couple antibodies site directed to nanoparticles. To do so the sugar groups of poly-clonal antibodies have to be reduced to obtain the aldehyde groups. The advantage of this procedure is that the antibodies are primarily bound to the MNPs oriented at the Fc-region leaving their antigen-binding site un-affected. The disadvantage is the use of sodium cyanoborohydride for the reduction of the Schiff-Base, which is very toxic. Sulfhydryl groups can be coupled using maleimide or pyridyl disulfide groups on the targets creating thioether or disulfide bonds [49, 74]. Their disadvantage is the easy cleavage of the bonds under reductive conditions. Alkynes can react with azides via click chemistry. This type of reaction needs a Cu-catalysis [49]. This reaction type is very specific and can be carried out under mild conditions for biomolecules. Furthermore, the formed bonds are highly stable. However, the Cu-catalyst shows severe side effects if not fully removed for *in vivo* applications [49]. Another new way of functionalisation uses bioorthogonal chemistry making it possible to first administer the affinity ligand, like an antibody, and then couple the particle to the antibody *in vivo* [49, 77]. Using this approach the antibody can first bind to its target and is then coupled to the nanoparticle leaving its orientation during the coupling of no relevance for its functionality [78]. This technique uses an irreversible Diels-Alder reaction between a tetrazine on the particle surface and a dienophile, like norbornene or trans-cyclooctene, which is bound to the according affinity molecules [77].
Amino groups on the particles can be functionalised using different chemical approaches. Direct conjugation can be accomplished using for example anhydrides, succinimidyl esters, epoxides and isothiocyanates. These techniques lead to stable linkages except for the isothiocyanate and are applicable to the conjugation with small molecules [49]. For the functionalisation with biomolecules the use of crosslinkers is common since this way offers more control over the orientation and the preserving of the biological activity of the affinity ligand.

Amine and carboxyl groups can be activated and crosslinked with each other using carbodiimide chemistry creating an amide bond. The advantage of this linker is the straight forward chemistry and the commonness of amine and carboxy groups in biological molecules, which made these chemicals the most frequently used crosslinking agents [74]. Carboxy groups are activated with this chemistry by using EDC creating an o-acylisourrea active intermediate. Unfortunately, this intermediate is not very stable and can easily be cleaved off in a competing reaction by hydrolysis [74]. To circumvent this obstacle the intermediate can be stabilised by the reaction with N-hydroxysuccinimide (NHS) or N-hydroxysulfosuccinimide (sulfo-NHS) as shown in Figure 2.10. Their disadvantage is the possible poly-

merisation of the biomolecules or particles [49]. This can be prevented using a two step activation protocol. First the ligand is activated by adding both chemicals, then the amino-particle is added in excess for conjugation.

For all reactions dealing with the functionalisation of nanoparticles the success depends strongly upon keeping the particles stable dispersed throughout all conjugation steps [74]. This means particularly to establish the right buffer system for the reactions to take place.

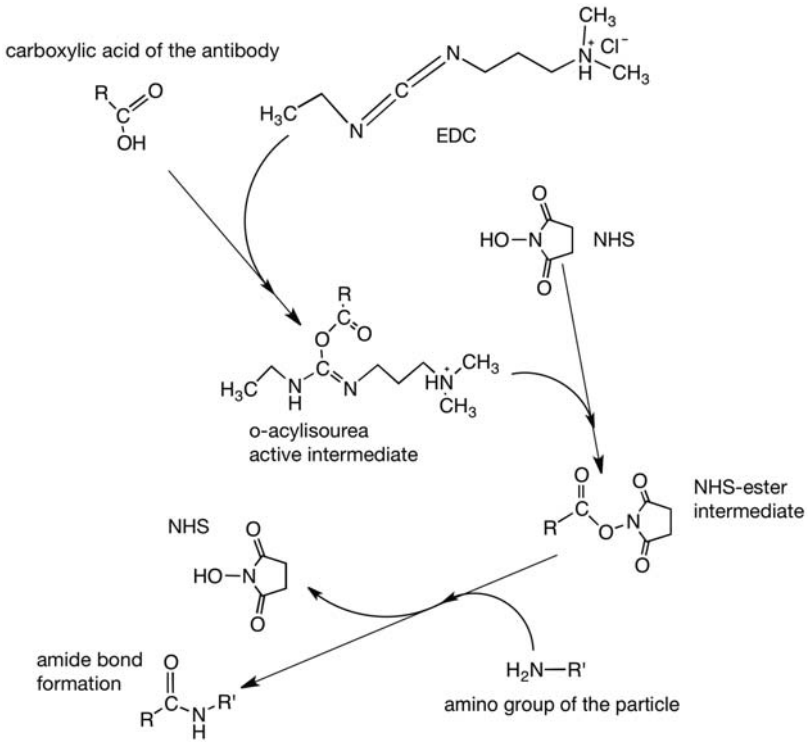

Figure 2.10.: Reaction of EDC and NHS to couple proteins to an amino group on a particle surface leading to a secondary amide bond

Using these techniques particles have been conjugated with various ligands, like small molecules, peptides, aptamers, proteins and antibodies [49]. For therapeutic applications antibodies like monoclonal antibody (mab) A7, herceptin, rituxan, anti-transferrin, anti-annexin V, anti-vascular cell adhesion molecule-1 (VCAM-1), anti-E-selectin, anti-myosin, anti-humanIgG, mab 610, anti-epidermal growth factor (EGFR), anti-carcinoembryonic antigen (CEA) have been applied so far for functionalisation [3, 4, 7, 49].

2.2. Magnetic Nanoparticles in Nuclear Magnetic Resonance

2.2.1. Fundamentals

Interaction of MNP with a Static Magnetic Field

The influence on the homogeneity of an external main magnetic field and, hence, indirectly the impact on relaxation times are shown in Figure 2.11 for ferromagnetic/superparamagnetic nanoparticles (Figures 2.11 (a) and (b)) with a total magnetisation M. The ferromagnetic/ superparamagnetic nanoparticle is fully aligned with the external field. Figure 2.11 (b) shows the contour lines of the magnitude of the magnetic field and Figure 2.11 (a) the distortion of the homogeneity of the external field B_0. The colour scheme indicates the degree of disturbance of the B_0 field. Brighter areas indicate higher disturbances; darker areas indicate weaker perturbation of the external magnetic field. The degree of disturbance was normalised to the corresponding maximum value (Figure 2.11).

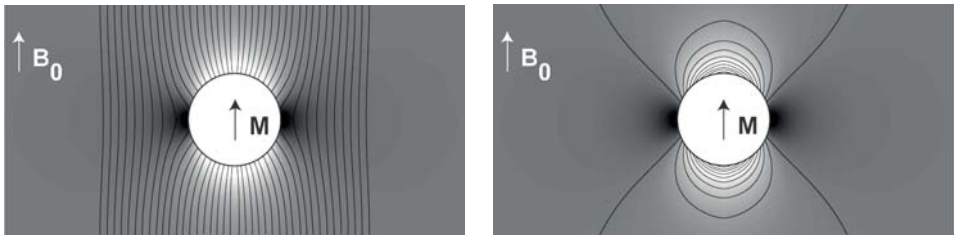

(a) (b)

Figure 2.11.: The figure shows the magnetic field of a superparamagnetic dipole moment of single domain particle. Shown are the magnetic field lines (a) and the contour lines of the magnitude of the magnetic field (b). **M** indicates the direction of the magnetisation vector and $\mathbf{B}_0$ the external homogeneous magnetic field. The lighter shadings denote higher disturbances whereas the darker areas indicate lower disturbances. Adapted from [79].

Nuclear Magnetic Resonance

Certain atomic nuclei possess a permanent magnetic dipole moment, which derives out of their nuclear spin and the gyromagnetic ratio, γ, a characteristic constant for every nuclei. The most important example for medical and biological application is the hydrogen nucleus ^{1}H in water molecules. For the proton ^{1}H the gyromagnetic ratio is ~ 42.6 MHz T^{-1} and its nuclear spin equals $\frac{1}{2}$. In a static main magnetic field $\vec{B}_0$, the magnetic dipole moments are pointed either in direction of the main field (lower energy state) or in the opposite direction (higher energy state). At body temperature, the two states are populated by the nuclear spins according to a Boltzmann distribution with a higher population in the lower state. This difference in occupation numbers of the two energy states leads to the measurable net magnetisation $\vec{M}_0$ (Figure 2.12 (a)). Both orientations are linked to slightly different

energy states, which are called nuclear Zeeman-levels; the energy gap is proportional to the magnitude of the main magnetic field B_0:

$$\Delta E_m = \gamma \hbar B_0 = \hbar \omega_0 \tag{2.34}$$

Since ΔE_m is also proportional to the larmorfrequency,

$$\omega_0 = \gamma B_0, \tag{2.35}$$

transitions between the two energy states can be achieved by applying a time varying magnetic field perpendicular to the main magnetic field $\vec{B}_0$. The frequency of this perturbing magnetic field is given by ω_0. For a typical magnetic resonance imaging (MRI) device with a B_0 field of 3 T, a radiofrequency of 127.8 MHz is needed to flip the net magnetisation vector of the nuclei out of its initial orientation. Nuclear resonance imaging devices used for small samples are commercially available up to field strengths of more than 20 T, resulting in a radiofrequency of more than 900 MHz.

If a perturbing magnetic field with the adequate frequency, ω_0, and duration, τ_p, is irradiated perpendicular to the main magnetic field, the magnetisation vector, $\vec{M}_0$, will be flipped a certain angle (Figure 2.12 (b)). The flip angle, α, is given by

$$\alpha = \gamma B_{RF} \tau_p, \tag{2.36}$$

with the amplitude of the perturbing field, B_{RF}. Thus, the flip angle can be tuned by changing the time of B_{RF} or its amplitude. The pulses applied to rotate the magnetisation $\vec{M}_0$ by each angle are called after their flip angle, 90° pulse or 180° pulse, for example.

The magnetisation $\vec{M}_0$ can be split into two components: the longitudinal magnetisation $\vec{M}_z$, which is parallel to the main magnetic field $\vec{B}_0$, and into the transverse magnetisation $\vec{M}_{xy}$, which is perpendicular to it (Figure 2.12 (b)). The 90°pulse results in the synchronisation of the molecular magnetic moments, $\vec{\mu}$, to yield a macroscopic transverse magnetisation M_{xy}, which is equal in magnitude to the main magnetisation M_0. Since $\vec{M}_{xy}$ is a precessing magnetisation in the x-y plane, it can be described as a common (phase coherent) precession of a „spin package of atomic nuclei“. The free induction decay (FID) of this „spin package“can be detected with a detector coil immediately after the application of the radio frequency pulse. The signal arises from this rotating magnetisation in the x-y plane.

Relaxation Processes

In real spin systems the magnetisation returns to its equilibrium after an excitation pulse due to molecular movement and chemical exchange processes. These movements cause an

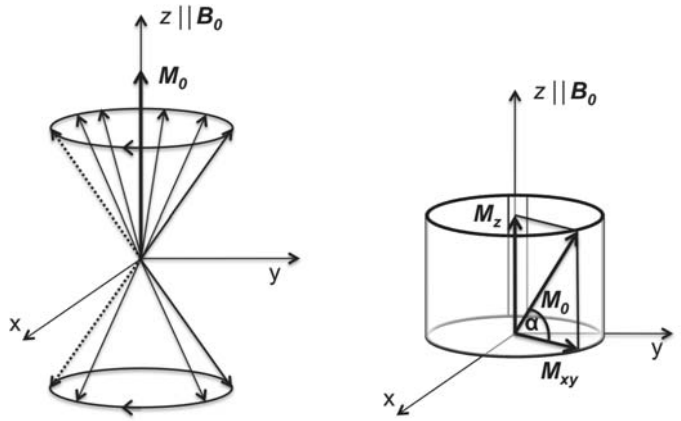

Figure 2.12.: Illustration of the origin of the nuclear net magnetisation $\vec{M}_0$ of hydrogen spins in a main magnetic field $\vec{B}_0$. (a) The Boltzmann distribution of an ensemble of hydrogen nuclei is allowed on two precession cones. In thermal equilibrium the occupation number of the state of lower energy is somewhat higher than that of the state of higher energy leading to the net magnetisation $\vec{M}_0$. (b) Definition of the transversal and longitudinal magnetisation; As the net magnetisation $\vec{M}_0$ precesses in the stationary frame around the z axis, it can be split into two components; the transversal magnetisation $\vec{M}_{xy}$ and the longitudinal magnetisation $\vec{M}_z$.

additional fluctuating magnetic field, which is different from nucleus to nucleus and has to be added to the external magnetic field. This additional magnetic field causes changes in the magnetisation, which are called relaxation. There are two different relaxation processes: the spin-lattice relaxation and the spin-spin relaxation.

Spin-Lattice Relaxation The spin-lattice relaxation describes the recovery of the magnitude of the original longitudinal magnetisation M_0 in the static magnetic field B_0, after the application of the radio frequency pulse. The perpendicular part of the additional fluctuating magnetic field to the main magnetic field causes transitions between the different Zeeman-levels. This mechanism allows the spin system to gain and lose energy until the Boltzmann distribution of the spins is restored. The lattice, which means all the atoms and molecules the nuclei contain, forms the energy storage for this mechanism. The regrowth of the net longitudinal magnetisation is characterised by the T_1 relaxation time, which is given by

$$M_z(t) = M_{z,0}\left(1 - e^{\frac{-t}{T_1}}\right), \tag{2.37}$$

with the magnetisation $M_{z,0}$ in equilibrium state [80, 81]. T_1 is defined as the time after the radio frequency pulse of 90° required for the magnetisation M_z to reach 63% of the original magnetisation $M_{z,0}$.

Spin-Spin Relaxation The spin-spin relaxation describes the decay of magnitude of the transverse magnetisation M_{xy}. Right after the 90°pulse exists a coherent transverse magnetisation. Due to dipole-dipole interactions this phase coherence is irreversibly lost and the transverse magnetisation decreases with the transverse relaxation time T_2. In this relaxation process, the parallel component of the fluctuating magnetic field to the main magnetic field causes a change in the precession frequency of the spins and therefore changes the phase of each spin. Thus, right after excitation all spins point in the same direction, but shortly afterwards, some spins precess faster than others around the direction of the B_0 field. The spins fan out, are dephasing, and M_{xy} is decreasing. This relaxation process is compared with the spin-lattice-relaxation solely effected by entropy mechanisms and no energy exchange occurs. The decay magnitude of the magnetisation M_{xy} is given by

$$M_{xy}(t) = M_{xy,0}\left(e^{\frac{-t}{T_2}}\right), \tag{2.38}$$

with the magnitude of the initial transversal magnetisation $M_{xy,0}$. T_2 is defined as the time duration until 63% of the transversal magnetisation is lost.

Typical samples in magnetic resonance experiments are large compared to single atoms or molecules, each with one or several individual spins. Therefore not only fluctuating local magnetic fields, but also spatial inhomogeneities of the main magnetic field $\vec{B}_0$, for example, caused by manufacturing imperfections, contribute to the transverse relaxation. This leads to a faster decay of M_{xy} than expected. These time independent field inhomogeneities provoke an additional phase shift and therefore the T_2' relaxation process, or the secular term of the T_2 relaxation time. Since these inhomogeneities are constantly present it is possible to invert the T_2' relaxation process, using the so called spin echo pulse sequence. The overall de-phasing of the transverse magnetisation can be described as the T_2^* decay:

$$\frac{1}{T_2^*} = \frac{1}{T_2} + \frac{1}{T_2'}. \tag{2.39}$$

Both, T_1 and T_2 relaxation processes are executed independently and simultaneously. At the field strengths used in MRI, the duration of the T_1 relaxation process depends on the magnetic field strength of B_0, whereas the T_2 relaxation process is almost B_0-independent [82]. The T_2 relaxation process rather depends on the magnetic dipole-dipole interactions, on the diffusion constant of the protons and on the field inhomogeneities. In most cases, the T_2 relaxation time is shorter than the T_1 relaxation time. An imperfect magnetic main field or high magnetic dipole moments of e.g. superparamagnetic nanoparticles can cause magnetic inhomogeneities. Consequently, the observed transverse relaxation time (T_2^*) is even shorter than the natural T_2 relaxation time caused by spin-spin interactions.

Contrast Agents

Contrast agents for MRI should have an influence on at least one of the following parameters: the spin density, ρ, the relaxation times, T_1 and T_2, on the diffusion, D, on the flow (perfusion) and on the susceptibility χ [11]. The spin density relates to the fraction of protons which contribute to the NMR signal. Diffusion and perfusion during an nuclear magnetic resonance (NMR) measurement lead to the motion of spins and their de-phasing resulting in a spin incoherence. Both parameters can hardly be influenced by contrast agents. Susceptibility and the relaxation times are of more importance. Every matter has a magnetic susceptibility meaning its ability to become magnetised in the presence of an external magnetic field. The susceptibility is therefore also useful to categorise the magnetisms of matter into: diamagnetism ($\chi < 0$), paramagnetism ($\chi > 0$) and ferromagnetism/superparamagnetism ($\chi \gg 0$, including ferri- and antiferrimagnetism) [11]. Iron oxides are widely used as superparamagnetic contrast agents due to their strong magnetic properties in medical imaging [54, 83, 84, 85]. The field strength in commonly used MRI scanners is sufficient to saturate the magnetisation of superparamagnetic particles. Hence, the orientations of all dipole moments of the particles are aligned with the field. Due to the high susceptibility of the superparamagnetic particles large local field inhomogeneities are generated (Figures 2.11 (a) and (b)). This leads to large local field gradients, which accelerate the de-phasing of the proton spins. A strong reduction of T_2 relaxation time and a relatively small influence on T_1 relaxation time are the consequences [8].

Superparamagnetic iron oxides can be doped with manganese ions for better sensitivity in their function as contrast agents [86]. Among various crystalline polymorphous iron oxides, maghemite (γ-Fe_2O_3) and magnetite (Fe_3O_4) are the one with the greatest interest in biological and medical applications [20].
Pure metals as core material like Fe and Co have the advantage of a high saturation magnetisation [87, 88]. However, their oxidative stability is lower and the toxicity is higher compared to iron oxides. To circumvent these obstacles some particles are made of an elemental iron core and an artificial ferrite shell (Fe@M-Fe_2O_4, M=Fe, Mn, Co) combining biocompatibility with almost no hysteresis [89].

2.2.2. Relaxivity and Relaxation Rate of Magnetic Nanoparticles

Relaxivity (r_1, r_2) measures the ability of any kind of MNPs to influence either longitudinal relaxation time T_1 (r_1) or transverse relaxation time T_2 (r_2) or both of the surrounding water proton spins. It is measured *in vitro* and represents the relaxation enhancement of water protons by the MNP or contrast agent at a 1 mM concentration [90]. Relaxivity of a compound depends mainly on the type of tissue, the material of the particle and the magnitude of the main magnetic field B_0. Transverse relaxivity of superparamagnetic nanoparticles can be as high as 148 $mM^{-1}s^{-1}$ for Feridex, a commercially available MRI contrast agent [91], whereas the longitudinal relaxivity can be far below 30 $mM^{-1}s^{-1}$ [54]. The longitudinal

relaxivity of manganese oxide based paramagnetic agents for example, is in the range of 10-20 mM $^{-1}s^{-1}$ as determined in 1% agarose gel [92]. Hence, relaxivity can be used to characterise contrast agents in MRI for the study of specific tissue areas or simply to achieve a better image quality. NMR relaxivity can also be measured to gain information about the linkage between functionalised nanoparticles and biological material. The relaxation rates R_1 and R_2 are quantities, which are derived from the reciprocals of the corresponding longitudinal (T_1) and transverse (T_2) relaxation time. The relation between concentration of the MNP, the relaxivity and thus the change in relaxation time is linear as follows [93, 94]:

$$R_1 = \frac{1}{T_1} \propto r_1 \times c \tag{2.40}$$

$$R_2 = \frac{1}{T_2} \propto r_2 \times c. \tag{2.41}$$

The relaxation rates are influenced by the diffusion velocity of protons and hence by the molecule structure. Fat, as an example, has a larger molecule structure than water and thus a slower diffusion velocity than water. This results in a larger relaxation rate and thus in a shorter relaxation time. The introduction of relaxivites and relaxation rates allows the characterisation of different agents with regard to their increase of contrast in magnetic resonance imaging. The ratio of both relaxation rates r_1 and r_2 at different field strengths gives also hints about the agglomeration state of the particles [95]. For small particles an increase in the ratio indicates agglomeration of the particles.

2.2.3. Inner and Outer Sphere Relaxation Theory

The origination of the different contrasts (T_1- and T_2-weighted) obtained with MRI can be explained using two different relaxation theories of the water protons surrounding the according contrast agent. The first theory is called inner sphere theory, the second outer sphere theory. Both are additive and contribute to the according T_1 and T_2 relaxation times. The sphere in this case refers to the coordination sphere of the underlying metal ions.

Inner Sphere Relaxation

The inner sphere relaxation theory refers to the chemical exchange mechanism which occurs upon the binding of a water molecule to the primary or inner coordination sphere of a metal ion. This exchange leads to a contribution of the proton relaxation rate which is based on the magnetic influence of the ion and the efficiency of the chemical exchange [11]. The chemical exchange between the metal ion and the bound water leads to interactions between the ion (electron) and the proton (nuclear). The resulting rapid relaxation is further transferred to the proton pool through water exchange mechanisms [96]. This mechanism depends on the amount of water molecules which are able to bind to the inner

sphere and on their residence lifetime in the bound state. There is a direct proportionality between the contribution to the relaxation rate and the amount of bound water molecules. Furthermore, the longer the water protons can stay in the bound state the slower the rate of the inner sphere relaxation will be. This relaxation mechanism holds mostly true for paramagnetic ions, since here the inner sphere of the ion is free accessible for the water. The relaxation of the water protons in the presence of paramagnetic ions can be expressed by the Solomon-Bloembergen-Morgan equations [11, 97]. These equations state that the reciprocal of both relaxation times, T_1 and T_2, can be derived out of the sum of two terms. The first term contributes the dipole-dipole interactions and the second term the scalar interaction.

The dipole-dipole term describes the distance related field interactions between the water proton and the unpaired electron of the metal ion. This interaction in turn depends on the following factors:

- the total electron spin of the metal ion,
- the distance between the proton and the ion,
- the motion of the rotational and translational tumbling of the water-ion complex,
- the lifetime of the bound water molecule, also known as the chemical exchange time,
- the electron spin-relaxation time and
- the Larmor frequencies of the proton and the electron.

The scalar term represents the exchange interaction between the metal ion electrons and the water proton spins which is caused by the chemical bonds between them.

Outer Sphere Relaxation

If a water molecule only comes as close as the secondary or outer coordination sphere of a metal ion this contribution to the proton relaxation rate is called outer sphere relaxation [11, 54, 98]. Therefore, the distance between the proton and the particle is important [99]:

$$\tau_D = \frac{r'^2}{D}, \tag{2.42}$$

where D is the diffusion coefficient and r' the radius of the magnetised material as the distance of the closest approach. The closer the proton gets the greater the effect on the outer sphere relaxation rate. At the same time its translational diffusion time, τ_D, increases and the probability of the interaction between the metal ion and the protons and therefore the influence on the relaxation time increases as well. The relaxation rate $R_{2,OS}$ can therefore be expressed for weakly magnetised material [99], like paramagnetic nanoparticles, at high magnetic fields as

$$R_{2,OS} = \left(\frac{4}{9}\right) V_{PM}\,\tau_D\,(\Delta\omega_r)^2\,, \tag{2.43}$$

V_{PM} is the volume fraction occupied by the magnetised material and $\Delta\omega_r$ the mean angular frequency shift at the distance r from the proton to the magnetic center of the paramagnetic particle which corresponds to the radius of the particle [99]. At high fields, τ_D decreases with an increase in the environmental mobility of the protons leading to a lengthening in the outer sphere relaxation time. Thus, large viscosity of the medium or large molecules adjacent to the particle will decrease mobility and increase the relaxation rate [11]. For superparamagnetic nanoparticles the contribution of the inner sphere relaxation is almost negligible and the mechanism of outer sphere relaxation has been transferred to them with some modifications [3]. The interaction of the proton spins with the magnetic moment of the particle has been described by Freed in his outer sphere model. These equations can be transferred to the outer sphere relaxation of superparamagnetic particles if the transversal relaxation time of the electron is exchanged by the Néel relaxation time of the particle. If the translational diffusion time is much shorter than the Néel relaxation time, τ_N, Freed′s equations reduce to the equations of Ayant [3].
In an external magnetic field the influence of the magnetic moment of the particle on the spins of the protons depends on the time of the proton in its near proximity as well as on the preccesion period of the spins. This means if the global correlation time τ_C,

$$\frac{1}{\tau_C} = \frac{1}{\tau_D} + \frac{1}{\tau_N}, \tag{2.44}$$

is longer than the precession period of the spins the fluctuation of the correlation time is averaged by the precession of the proton spins and the influence of the superparamagnetic particle on the relaxation time is inefficient. If the correlation time is shorter than the precession period of the spins, the spins are able to get influenced by the superparamagnetic relaxation and the relaxation time of the system is efficiently influenced [3].
Since the outer sphere relaxation depends on the Néel relaxation time of the superparamagnetic particle (Equations 2.43 and 2.44) it also depends on the anisotropy energy of the particle and therefore on its crystal structure (Equation 2.4). Concluding that for large superparamagnetic crystals (d $\geq$ 10 nm) with a very high anisotropy constant, the anisotropy energy is much larger than the thermal energy and therefore the direction of the magnetic moment will stay aligned with the easy axis. Thereby, the precession of the electron magnetisation will be forbidden in a simplified model [3]. In small crystals (d $<$ 10 nm) the opposite happens and the electrons can precess as well.

2.3. Magnetic Nanoparticles as Detectors

2.3.1. Fundamentals

As has been explained in the outer sphere relaxation the influence on the T_2 relaxation time of protons depends also on the size of the superparamagnetic particle. The next paragraphs refer to superparamagnetic nanoparticles with increasing size, but the iron content of the sample stays the same. The explanation of the theory starts with many small particles and ends up with a few larger particles. Furthermore, this theory applies to strongly magnetised particles, which are defined by a large dephasing of the surrounding protons during the echo interval in an applied CPMG sequence:

$$\tau_{CP} < \frac{1}{\Delta\omega_r}, \tag{2.45}$$

where τ_{CP} is half the interval between successive 180° pulses in the CPMG sequence and $\Delta\omega_r$ is the root mean square of the angular frequency shift of the protons at the distance r (the radius of the particle) compared with a point infinitely far away [100]. If the particles are small enough that

$$\tau_D < \frac{1}{\Delta\omega_r} \tag{2.46}$$

the theory of the **motional averaging regime** can be applied.

$$\tau_D = \frac{r^2}{D}, \tag{2.47}$$

where r is the particle radius and D the water diffusion coefficient, that means that τ_D is the diffusion time needed of a water molecule to cover a distance of $\sqrt{2r}$ in any direction. In the motional averaging regime the relaxation rate is given by

$$\frac{1}{T_2} = \left(\frac{4}{9}\right) V_{MNP} \tau_D \left(\Delta\omega_r\right)^2, \tag{2.48}$$

where V_{MNP} is the volume fraction of the MNPs. Equation 2.48 holds true as long as the relaxation is not interrupted by a refocusing echo-pulse.

If the particles become larger their magnetic moments increase as well, making them more susceptible to the external magnetic field. The theory of the **static dephasing regime** can be applied. In this theory, the magnetic moments of the protons are motionless in a nonuniform magnetic field which is created by the randomly distributed dipoles of the MNPs. This places a limit on the relaxation rate increase and therefore on the T_2 relaxation time decrease, which can be reached in the absence of an refocusing pulse [100]. For

spherical particles, the relaxation rate of the protons in the static dephasing regime can be described as

$$\frac{1}{T_2^*} = \pi \frac{\sqrt{15}}{9} V_{MNP} \Delta\omega_r. \tag{2.49}$$

In this case $\Delta\omega_r$ is given by

$$(\Delta\omega_r)^2 = \left(\frac{4}{5}\right) \gamma^2 \frac{\mu^2}{r^6}, \tag{2.50}$$

with μ being the magnetic moment of the particles and γ the proton gyromagnetic ratio.

From a practical point of view, magnetic particles of this size would be the best contrast agents for T_2 weighted images. Since they have the most influence on the proton spin relaxation due to a more pronounced lack of the refocusing of the proton spins by the 180°pulse.

In the next regime the particle size increases further. The field inhomogeneity the protons experience is getting larger and the surface of the particle is also increasing giving the protons more time during their diffusion to experience the magnetic field of the particle. Since τ_D is further increasing the proton spins close to the MNPs experience a higher inhomogeneity. However, since the iron content stays the same less particles are present and less protons undergo this experience. This means that most of the proton spins in the sample only experience a weak field inhomogeneity of the magnetic nanoparticle. Therefore, the refocusing of the proton spins during T_2 relaxation acquisition gets easier to accomplish the bigger the particles are, since most of the protons are not influenced by the magnetic nanoparticle. This regime is called the **echo limited regime** where the partial refocusing model applies [31, 100].

Vuong et al. have performed simulations for NMR relaxation measurements of the above mentioned regimes with CPMG sequences and derived a development of the T_2 relaxation time over the particle size [31]. In Figure 2.13 all three regimes of the evolution of the T_2 relaxation time with the particle volume can be seen. First, the motional averaging regime where the T_2 relaxation time is decreasing with the increase of the particle volume. Second, the static dephasing regime where the influence of the magnetic nanoparticles on the T_2 relaxation times is most pronounced concluding that this is the best size regime for T_2 contrast agents. When the T_2 relaxation time increases again with the particle size, the particles are in the third regime, the echo limiting regime. In all cases the iron content stays the same.

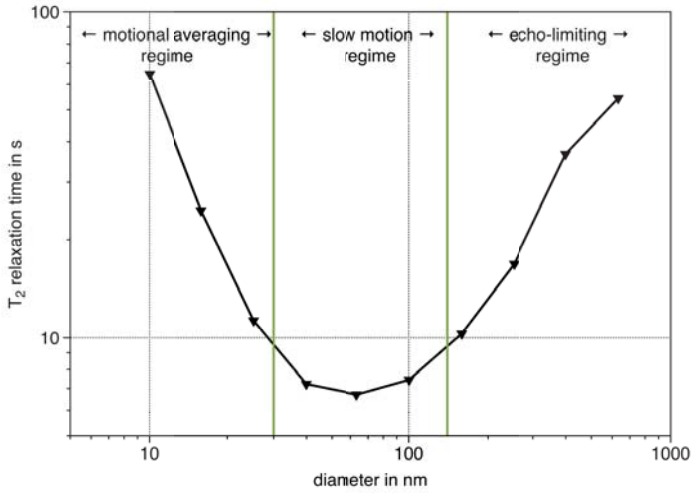

Figure 2.13.: Simulation of the dependence of the T_2 relaxation time on the diameter of magnetic nanoparticles according to [31]

2.3.2. T_2 Relaxation Time Measurements for Detection

The phenomenon of the changing T_2 relaxation time with the volume of the magnetic nanoparticle was also observed for the aggregation of magnetic nanoparticles. Muller et al. examined the influence on the relaxation rate, R_2, when particles of 50 nm diameter are aggregating, and saw a decrease of 25% in R_2 when the sample was left in the magnetic field [101]. If the sample was removed from the magnet and then reinserted, the relaxation rate returned to its initial value to decrease again with time. When the aggregation of smaller superparamagnetic nanoparticle cores occurs, the effect on the transverse relaxation time of the water protons is enhanced, because of an increase of the secular part of the transverse relaxation rate (Equation 2.39) [102]. The effects appearing after the aggregation of the superparamagnetic nanoparticles are two-fold: first, there are those related to the structure of the cluster and to the magnetic field distribution around it (T_2 and T_2^*); second, there are those limited to the inner part of the cluster (T_1). Since the aggregation of superparamagnetic particles mainly influences the outer sphere relaxation of the water protons and not the inner sphere relaxation, it does not affect the T_1 relaxation time in the same manner as the T_2 relaxation time [102]. This change in the T_2 relaxation time does not only hold true for the aggregation of magnetic nanoparticle but also for the clustering of magnetic nanoparticles due to specific binding partners. Figure 2.14 shows the magnetic field of a superparamagnetic particle with a functionalisation of ligands of a specific target (a) and with the target bound to the ligand on the particle (b). As illustrated, the bound target shields the water molecule from the influence of the magnetic field of the magnetic nanoparticle. This can be transferred to the clustering of MNPs due to according binding partners.

Figure 2.15 shows the progression of the T_2 relaxation time of the incubation of nanopar-

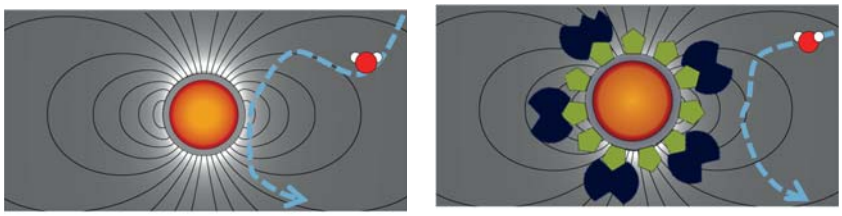

(a) (b)

Figure 2.14.: Magnetic field of a superparamagnetic nanoparticle with ligand functionalisation for a specific target (a) and with bound targets (b)

ticles (d = 100 nm) with their target at different ratios obtained by NMR relaxation measurements. There is a clear increase of the T_2 relaxation time, if the ratio of the target to the nanoparticles (in this case their iron content) is ideal for the clustering of the particles due to their target. If the target concentration increases further the T_2 relaxation time decreases again, but stays above the initial value, since all ligands on the surface of the particle are bound with a target which shields the water protons from the magnetic field of the particle as shown in Figure 2.14 (b) [103].

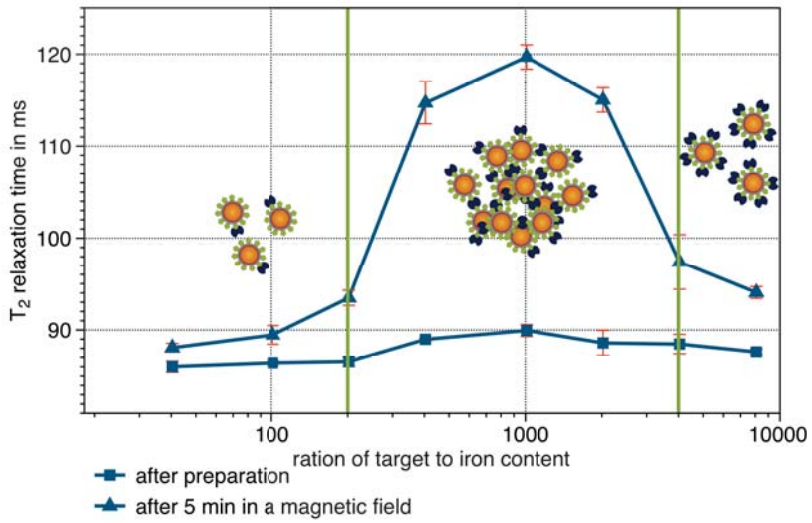

Figure 2.15.: Evolution of the T_2 relaxation time upon the incubation of nanoparticles (d = 100 nm) with different ratios with their target measured with NMR relaxation measurements; Shown are the T_2 relaxation times right after mixing of the samples and after the incubation in the magnetic field of the relaxometer. At the maximum of the T_2 relaxation time the ratio of target to nanoparticle is the best for the clustering of the particles. If the concentration of the target is further in creased the T_2 relaxation time decreases again, but stays above the initial value due to the bound targets (after [103]).

Using these observations a new detection method was developed based on the increase in the T_2 relaxation time of water protons, when MNPs are clustering, and on the indepen-

dence of T_1 to the clustering of the MNPs [104]. By using this method not only DNA and proteins, but also bacteria, viruses or even specific cells like tumour cells have been detected [32, 103, 104, 105, 106, 107, 108].
Others have shown that besides the size of MNPs also the size and valency of the target is crucial for the detection limit of the method [103]. Two sizes of particles with variable target analytes (the valencies and the sizes were different) were investigated under the use of a single molecular recognition system. For small MNPs (30 nm) the sensitivity improved using a bigger target and a higher valency of the target, whereas bigger MNPs (1 μm) were more sensitive to small and low valency targets. Small MNPs show a decrease in T_2 relaxation time whereas bigger MNPs show an increase (Figure 2.13). Next to the fact that high concentrations of the analyte will saturate the receptors and prevent further crosslinking and reduce the sensitivity, the aspect of the valency of the particles has also to be carefully considered. If the agglomerates get to big, this could lead to their precipitation [106].
To take advantage of these phenomena, particles with an improved T_2 relaxivity and diagnostic magnetic resonance devices (DMR) are being developed. The first device for point of care diagnostics using DMR consisted of permanent magnets with B_0 up to 21.7 MHz ($\approx$ 0.5 T) and a μNMR chip containing a 2$\times$4 planar micro coil array on a glass substrate, eight multiplexed measurements of 5-10 μl samples were possible [109]. Its detection limit was 1 pM, similar to the detection method of Baudry et al. where optical measurements for the determination of the target protein concentration were used [110]. The device was further improved by reducing the sample volume to 1 μl, so that the signal to noise ratio would be higher [111]. Furthermore, an automated feedback system was added to track and compensate for temperature drift, and a mobile device was used to facilitate the control of the system and to share the data over wireless networks [112]. The detection limit for cells was reduced to 2 cells/μl. To reduce the risk of false positive results the incubation time from 30 min was decreased to 5 min. With this it is possible to obtain results in less than 60 min. The first application on human tumour samples was very promising. An accuracy of 96% compared to standard of care procedures was achieved [113]. Besides these clinical application some experiments have been done with bacteria and viruses as targets. Particles of different sizes (d = 1000 nm and 30 nm) functionalised with an antibody to the Tag peptide have been used to target the influenza virus. Using a magnetic field induced aggregation and valency enhancement method for the detection they were able to reduce the T_2 relaxation time by 250 ms [107]. *Staphylococcus aureus*, *Bacillus Calmette-Guérin*, as a surrogate for *Mycobacterium tuberculosis* have been detected using the NMR T_2 relaxation time method [111, 112]. *Bacillus Calmette-Guérin* has been detected using so-called cannon balls which are magnetic nanoparticles made of iron core and a thin iron oxide shell functionalised with an monoclonal antibody. The sensitivity was increased by washing the sample from unbound cannon balls and at the same time increasing the concentration of the bacteria on a filter system [111]. *S. aureus* was targeted using magnetic nanoparticles functionalised with an anti-vancomycin antibody which recognises specifically D-alanyl-D-alanine moieties in the bacterial cell membrane. Using these particles and an DMR device approximately 10 bacteria were detected in a 2 μl (= $5{\cdot}10^3$ cells/ml) sample. With the same DMR measurements the detection of avidin was also performed using

magnetic nanoparticles with bound biotin. The particles had a hydrodynamic diameter of 36 nm and were able to detect 1 nM avidin in a 2 μl sample using a 0.2 mM Fe concentration of magnetic nanoparticles.

2.3.3. Quality Control in the Beverage Industry

As described before, the change in the T_2 relaxation time of aqueous samples upon binding of targets to magnetic nanoparticles in the sample is useful for the detection of small molecules, proteins, tumour cells, or pathogens [32]. Another field of application could be the quality control in the cosmetic or food and beverage industry. In the beverage industry the detection of beer spoiling bacteria is very important. These bacteria are not dangerous to the human health, but lead to a change of the taste, the colour or the texture of the beverage [114]. These spoilage bacteria for beer are for example *Lactobacillus brevis*, *Lactobacillus lindneri*, *Megasphaera cerevisiae* [115].

For the production of alcohol-free beverages the absence of *Saccharomyces cerevisae* is of great importance. The general detection of quality spoilage bacteria in the beverage industry uses the detection via cultivation of the samples, via immuno assays using antibodies against the bacteria or via reverse transcriptase polymerase chain reactions (RT-PCR) [116, 117].

Bacterial Cultivation is the oldest method to detect bacteria. A sample is filtered using membrane filtration to concentrate the bacteria. The bacteria stay on the membrane and are subsequently cultivated plating the membrane on a cultivation dish. Depending on the bacteria different cultivation conditions are used to determine the strain of bacteria. This procedure can take 3 to 10 days.

Immuno Assays use specific antibodies to detect the target bacteria. The most common are enzyme linked immunosorbent assays (ELISA) where the specific antibodies are targeted by fluorescent labelled antibodies. This fluorescence is detected photometrically. Additionally, quick tests are also used. The sample has to be filtrated as for the bacterial cultivation and the time for the test takes about one hour including the filtration step.

RT-PCR is the most specific and sensitive test available. The bacteria are detected through the amplification of messenger RNA (mRNA) using specific probes. It is necessary to purify the sample before the detection. The detection itself takes about one to two hours.

All methods mentioned have to be done by trained personnel and need laboratory equipment. If small or medium sized breweries want to control the quality of their beverages they usually need to take samples and have to have them examined by external laboraties. To be more flexible and faster in their production especially in the summer months a new

method for a rapid, specific and sensitive detection is needed. The NMR T_2 relaxation time method is a good approach. The measurement can be carried out by untrained personnel and no laboratory equipment is needed. The magnetic nanoparticles specific for the target bacteria have to be mixed with the sample and the mixture has to be supplied to the NMR relaxometer measurement system. As the first target for the beverage industry *S. cerevisae* was chosen [35]. Commercial antibodies are available, which can be coupled to MNPs for the detection using NMR T_2 relaxation time measurements. Figure 2.16 shows a schematic drawing of a *S. cerevisae* cell with a bound MNP via an antibody specific binding.

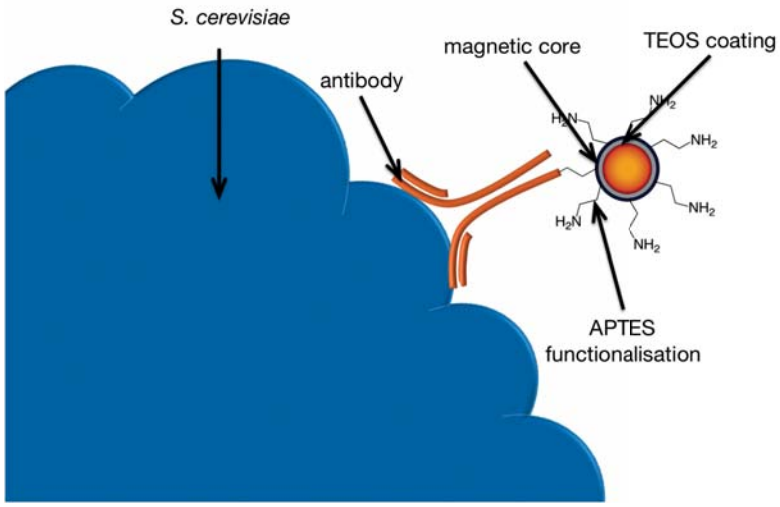

Figure 2.16.: Schematic drawing of a magnetic nanoparticle functionalised with an antibody binding to a *S. cerevisae* cell. Sizes are not to scale.

3. Material and Methods

This chapter presents the preparation of the MNPs using a co-precipitation method combined a the polyol method, their functionalisations including their characterisations according to their size, their core, their surface and their magnetism. Their size has been characterised using dynamic light scattering (DLS) and transmission electron microscopy (TEM). TEM was also used to characterise the core together with Mössbauer spectroscopy. The surface of the particles was characterised using Fouriertransformed infrared (FT-IR) spectroscopy and the measurements of the zeta potential in dependence of the pH of the solution. The magnetism was determined by M(H) measurements, magnetic particle spectroscopy (MPS), NMR-D profiles and relaxivity measurements. Furthermore, the characterisation of the applied antibodies and their targets as well as the conducted NMR relaxation measurements are described.

All chemicals and the equipment are listed in Appendix B.

3.1. Particle Synthesis

The core of the particles was prepared by a co-precipitation method combined with a polyol method using a chemical synthesis reactor. With this set-up reproducible and stable cores of magnetic nanoparticles were prepared. In order to increase the stability of the magnetic nanoparticles, two layers of coating were applied. First, the core of the particle was fabricated using the co-precipitation method combined with a polyol-method. Second, the first layer made of tetraethoxysilane (TEOS) was subsequently applied using the method by Massart et al. [68]. Afterwards, a second coating was applied using (3-Aminopropyl)triethoxysilane (APTES) for functionalisation with amino groups. An overview of the structures of the nanoparticles during the synthesis steps is shown in Figure 3.1. For the detection of avidin and *S. cerevisiae* the MNPs were finally functionalised with the respective antibodies.

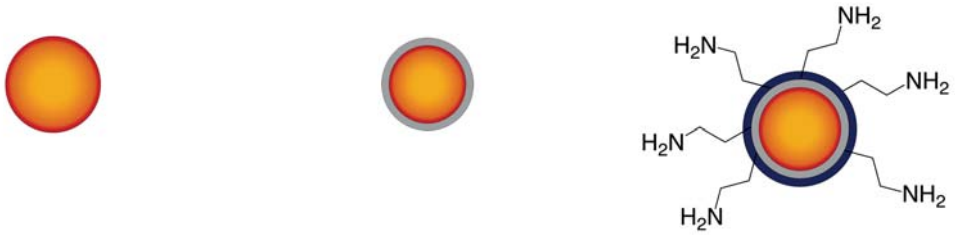

(a) magnetic core of the particle (b) particle core with first TEOS coating (c) particle core with TEOS coating and APTES functionalisation

Figure 3.1.: The three stages in the preparation of the magnetic nanoparticles until they are ready for the final functionalisation with antibodies

For the synthesis of magnetic nanoparticles with a very narrow size distribution and a size of 8±2 nm the protocol from Forge et al. was applied with minor modifications [118].

45 mmol $FeCl_2 \cdot (H_2O)_4$ were dissolved in 37 mmol 45% $FeCl_3 \cdot (H_2O)_6$ solution and the mixture was added to the chemical reactor. The stirring speed of the reactor was set to 150 rpm until the end of synthesis. 300 ml of diethylene glycol were added under stirring. The solution was then purged with nitrogen throughout the reaction. The pressure of the nitrogen was set to 0.5 mbar and the reactor was heated to 170 °C for 1.5 h. After reaching this temperature and further equilibration at this temperature for 15 min, 15 g of NaOH-pellets were quickly added. The suspension turned black immediately and was kept at 170 °C for 1 h. Afterwards the reaction was cooled to 80 °C. The liquid was poured from the reactor into a beaker and the particles were magnetically separated using a NeFeB permanent magnet (N45, l x b x h = 8 x 4 x 1 cm^3) for 2.5 h. After the particles were separated from the solution, the supernatant was carefully removed using a pipette and the particles were redispersed in 250 ml 1 M HNO_3 using a magnetic stirrer. This washing step was repeated 4 times each with 250 ml 1 M HNO_3. After the last separation the particles were resuspended in 80 ml of deionised H_2O to remove most of the strong acidic environment and stirred at room temperature overnight. The next day, the black suspension was sonicated in a water bath at room temperature for 45 min and afterwards centrifuged at 16'700 rcf at 21 °C for 1 h. The supernatant containing the MNPs was carefully removed with a pipette. To make sure only small particles were collected, a volume of around 5 ml was left in the centrifugation tube. The particles were characterised by performing iron content determination, DLS and Zeta potential measurements as well as FT-IR and Mössbauer spectroscopy, M(H) and relaxivity measurements.

With the use of the chemical synthesis reactor the temperature, the stirring speed and the time duration were regulated for each step of the protocol. The protocol used for each reaction is shown in Figure 3.2. Since the dissolving of the NaOH pellets is an exothermic

reaction the reactor temperature rises shortly, but is regulated by active cooling of the oil temperature in the reactor mantle until 170 °C is reached again. This short period of raised temperature is not critical to the reaction.

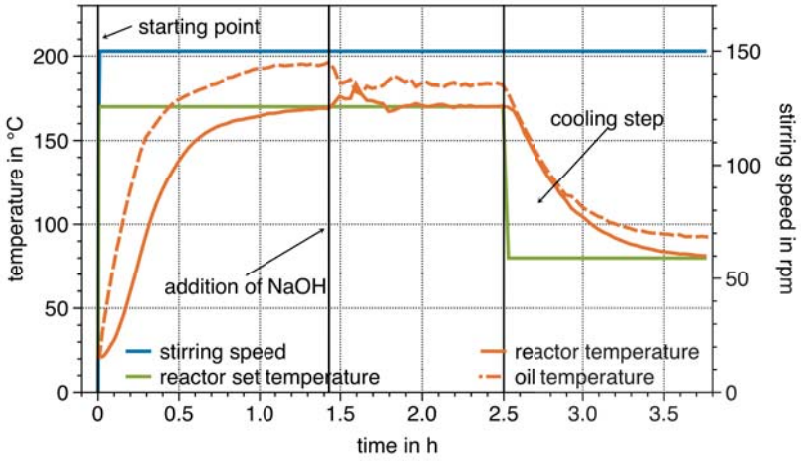

Figure 3.2.: protocol for the chemical synthesis reactor settings for the manufacturing of magnetic nanoparticles; shown are the temperatures of the oil in the reactor mantle (oil temperature), the set temperature of the reactor, the temperature inside the reactor (reactor temperature) and the stirring speed

3.2. Coating and Functionalisation

3.2.1. Tetraethoxysilane Coating

To protect the MNPs from further oxidation, an inorganic shell made from silica was chosen. To prepare this shell the particle suspensions were reacted with TEOS. After determination of the iron content in the nanoparticle suspension a volume of 40 ml - 60 ml was taken, 2 volume equivalents of H_2O_{dd} was added and the mixture was heated to 50 °C under nitrogen flush and stirring. After the temperature was reached and the reaction mixture was equilibrated, 2 mol equivalents of TEOS compared to the iron content were dissolved in 10 ml $EtOH_{96\%}$ and added dropwise to the heated MNP suspension. The reaction was carried out at 50 °C under nitrogen atmosphere for 24 h. Afterwards the suspension was homogenised in a sonication bath for 45 min. The particles coated with TEOS (MNP-TEOS) were washed using a ultrafiltration device. The first two washings were done with 140 ml H_2O_{dd} and 10 ml of $EtOH_{96\%}$ to improve the solubility of unreacted TEOS. For the last two washings only 140 ml H_2O_{dd} were applied. The concentrated nanoparticle suspension with TEOS coating (MNP-TEOS) was removed from the ultrafiltration device and centrifuged at 4'500 rcf at 21 °C for 45 min. The supernatant was collected carefully using a pipette and leaving about 5 ml of particle suspension to prevent a contamination with bigger agglomerates. Particles were characterised by application of the same methods as for the naked

particles.

3.2.2. Functionalisation

(3-Aminopropyl)triethoxysilane Functionalisation

(3-Aminopropyl)triethoxysilane (APTES) was used to obtain functional groups on the MNP-TEOS for the covalent coupling of binding moieties. For the reaction with APTES the pH is critical and should be kept around pH 2-3. 10 ml - 15 ml of MNP-TEOS were used and 2 volume equivalents of H_2O_{dd} were added. To this suspension 1 ml of 1 M HNO_3 was added to keep the pH low. Subsequently, the amount of APTES added was 0.8 times the mol amount of the iron content of the MNP-TEOS solution. Everything was stirred and the pH was checked. If it was too high (pH $>$ 3), it was adjusted using 1 M HNO_3. The reaction was heated up to 70 °C under nitrogen flush and stirring and incubated at this temperature for 2 h. Afterwards the suspension was subjected to a sonication bath at room temperature for 45 min and then washed using a ultrafiltration device. The suspension was washed 4 times using H_2O_{dd} which was added to a total volume of 140 ml each time. The particles (MNP-APTES) were centrifuged and characterised using the same procedures as for MNP-TEOS.

Antibody Functionalisation

Antibodies were purchased from http://www.antibodies-online.de and the host was in both cases rabbit (anti-avidin antibody: ABIN116964; anti-*S. cerevisiae*-antibody: ABIN260785). Both antibodies were prepared and handled according to manufacturer's instructions and diluted to 10 mg/ml anti-avidin antibody and 1 mg/ml anti-*S. cerevisiae*-antibody.

Anti-avidin Antibody Functionalisation was carried out using the EDC/NHS activation of the carboxygroups on the surface of the antibody. To 300 μl 10 mg/ml anti-avidin-antibody 33.61 μl 10 mg/ml NHS and 89.56 μl of 5 mg/ml EDC were added, giving a molar ratio of NHS to EDC of 1.25 and a mass ratio of NHS to antibody of 1.86. NHS was dissolved in dimethylsulfoxide (DMSO) and EDC in 50 mM sodium borate buffer (50 mM boric acid, 50 mM sodium tetraborate, pH 8.17) right before addition to prevent early hydrolysis. After an incubation in a shaker at room temperature for 10 min, 1'565 μl of 229 mM Fe MNP-APTES were added giving a mass ratio of MNP to antibody of 6.67. The volume of the reaction was increased to 5 ml using a 50 mM sodium borate buffer, pH 8.17. The reaction was performed on a rotating wheel for 2 h at room temperature. Subsequently, ultrafiltration was performed with a 300 kDa cut-off to remove unreacted reagents and antibodies. The ultrafiltration cell was filled up to 40 ml with blocking buffer (10 mM Na_2HPO_4, 1% BSA w/v, pH 7.4) 4 times. The supernatant was removed and stored at 4 °C until further use.

These MNP were named anti-av MNP.

Anti-*S. cerevisiae* Antibody Functionalisation was carried out in the same way as the functionalisation with the anti-avidin antibody, only with different volumes due to the 1 mg/ml stock concentration of the anti-*S. cerevisiae* antibodies. Briefly, to 300 μl 1 mg/ml anti-*S. cerevisiae*-antibody 3.36 μl 10 mg/ml NHS and 8.96 μl of 5 mg/ml EDC were added. After an incubation in a shaker at room temperature for 10 min 156.46 μl of 229 mM Fe MNP-APTES were added. The volume of the reaction was increased to 5 ml using a 50 mM sodium borate buffer, pH 8.17. The reaction was performed on a rotating wheel at room temperature for 2 h. Subsequently, ultrafiltration was performed to remove unreacted reagents and antibodies with a 300 kDa cut-off. The cell was filled with blocking buffer (10 mM Na_2HPO_4, 1% BSA, pH 7.4) up to 40 ml 4 times. The supernatant was removed and stored at 4 °C until further use. These MNP were named anti-*S.c.* MNP.

3.3. Core Characterisation

3.3.1. Iron Content

The iron content was determined with the *Fe Spectroquant kit* (Merck). For each determination of the iron content the calibration curve was measured using a freshly prepared 50 mg/l $FeCl_3$ solution according to manufacturer instructions. The working range of the kit was given by the manufacturer between 0.01 - 5 mg/ml. Since the particle suspensions exceeded this range the particles were dissolved in fuming HCl in an appropriate amount to meet this criteria. The ratio was usually 1:10. The dissolved particle HCl solutions were diluted further in H_2O_{dd} with factors between 1:100 and 1:1000 to match the working range of the assay.

3.3.2. Mössbauer Spectroscopy

Measurements were carried out with liquid and freeze-dried magnetic nanoparticles in a self-made Mössbauer spectrometer. Samples of MNP in diethylene glycol were applied to a Mössbauer sample holder, frozen in liquid nitrogen and measured at 4.2 K. These samples were also measured at 298 K with and without an applied magnetic field of 750 mT after mixing them with a two component glue and letting them air-dry at room temperature over night. MNP in aqueous solutions were lyophilised and also given into a sample holder and measured at 4.2 K and at 298 K. The iron density was around 5 mg/cm^3 and the sample in the sample holder was $\approx$ 5 mm thick.

3.3.3. Electron Diffraction Pattern

Measurements were carried out during the acquiring of TEM images. The particle suspensions were diluted to 10 mM Fe concentration. 5 μl of the particle suspensions were applied to a 300 mesh grid coated with carbon for the naked MNPs or to a 300 mesh grid coated with a holey carbon film (2 nm thickness) for the coated MNPs and anti-av MNPs with and without avidin. Subsequently, the particles were air-dried at room temperature. Besides the acquisition of images the electron diffraction pattern was also visualised of the core of the particles to proof the existence of iron oxide crystals. This was achieved by adjusting the magnetic lenses in a way that the back focal plane of the lenses is placed on the imaging apparatus rather than the imaging plane.

3.4. Size Characterisation

3.4.1. Transmission Electron Microscopy

The diameter of the core of the MNPs and the structure of the coated and functionalised particles was determined by TEM. The preparation procedure of the MNP is described in section 3.3.3. Images were taken with a JEM100 CX at 100 kV with different magnifications. The obtained images were digitalised at different resolutions. The size distribution of the cores of the MNPs was determined with the image processing program *ImageJ* with the feature *Analyze Particles*.

3.4.2. Dynamic Light Scattering

The size distribution of the hydrodynamic diameter of the nanoparticles in suspension was determined using DLS. The fabricated MNPs were characterised at the different steps of synthesis using the determined mean hydrodynamic diameter from number and intensity weighted size distributions. For the determination of the hydrodynamic diameter the particle suspensions were diluted 1:100 in H_2O_{dd} and measured directly using standard micro cuvettes. The measurement protocol consisted of an equilibration time of 60 s at 21 °C and of a repetition of 30 runs, each run taking 10 s. The repetition of 30 runs was chosen to minimise the measurement error of the device and therefore to achieve better statistics.

3.5. Surface Characterisation

3.5.1. Zeta Potential

For the determination of the Zeta potential at different pH, the MNP of all manufacturings stages were first diluted to 10 mM Fe in a volume of 1 ml using 1 mM NaCl. The pH was adjusted to the desired value using concentrations of 10 mM and 100 mM of KOH and HNO_3. Finally, the volume was adjusted with 1 mM NaCl to a total volume of 1.5 ml. After incubation at room temperature for 30 min the pH was verified and adjusted if necessary. The Zeta potential was determined using the *high concentration Dip cell* from Malvern. Both, pH and Zeta potential, were recorded to determine the pH stability of the particle suspension.

3.5.2. Fouriertransformed Infrared Spectroscopy

A sufficient amount of the particle suspension (500 μl - 2 ml, depending on the iron content of the sample) was frozen using liquid nitrogen and subsequently quickly transferred for lyophilisation. They were freeze-dried over night and measured directly after preparation to prevent hydration. FT-IR-spectroscopy was performed using a KBr-pellet preparation. For the pellet preparation, the KBr was dried at 120 °C over night to remove any residual traces of water. 100 mg of the dried KBr were pestled together with the dried MNP preparation using an achat pestle and mortar until a fine homogeneous powder was produced. The pellet was pressed with 125 kN.

3.6. Magnetic Characterisation

3.6.1. M(H) Measurements

Determination of the magnetisation of the particles was done using M(H) measurements. Fresh naked MNPs and two months old MNPs were freeze-dried over night and weighted before they were mixed with glue using a wooden tooth pick and glued into a plastic straw. Of the two naked magnetic nanoparticles 6.91 mg and 5 mg, of the MNP-TEOS 6.73 mg and of the MNP-APTES 7.24 mg were used. The M(H) measurements were performed from -3.5 T to 3.5 T. The obtained data was analysed using a simple model of a log-normal distribution of single domain particles. Starting with this log-normal distribution the mean value of the particle volume and subsequently the diameter and the magnetisation of the naked and two months old particles was calculated.

3.6.2. Magnetic Particle Spectroscopy

Preparations of MNPs were diluted to 10 mM Fe using 10 mM HNO_3. For the measurements the MNPs were further diluted 1:1 with deionised water. All measurements were done at 25 mT.

3.6.3. NMR-D Profiles

NMR-D profiles of the T_1 relaxation time were measured of naked MNP and MNP-TEOS one week after preparation. First, the concentration of the MNP suspensions was determined. Second, the particles were diluted to approx. 1 mM Fe for the T_1 relaxation time at 20 MHz and 60 MHz to be between 15 ms - 100 ms. The shorter the time the faster the determination of the NMR-D profile. The exact iron concentration of the samples was noted before each measurement and 200 μl of each sample were taken for the profiling. Measurements of the NMR-D profiles were carried out at 37 °C using a Fast Field Cycling NMR Relaxometer. NMR-D Profiles were taken from 0.015 MHz - 40 MHz. To increase the range of the NMRD-profiles, the measurement at 60 MHz was added to the profiles. The data was fitted using a self made software to calculate the diameter of the particles, their magnetisation and information about their anisotropy energy [3].

3.6.4. Relaxivity Determination

The relaxivity, r_2, of the manufactured MNPs was determined by the measurement of the T_2 relaxation time of the solvent and of different concentrations of the MNP suspensions at 21.7 MHz ($\approx$ 0.5 T). From the T_2 relaxation time the relaxation rate, R_2^{obs}, was calculated. All relaxation rates were corrected by the relaxation rate of the solvent, $R_2^{solvent}$. Then they were plotted against the iron concentration, c_{Fe}, of the suspensions. The slope of this curve is the relaxivit, r_2, of the MNPs

$$R_2 = \frac{1}{T_2} \tag{3.1a}$$

$$r_2 = \frac{R_2^{obs} - R_2^{solvent}}{c_{Fe}}. \tag{3.1b}$$

3.7. Antibody Functionality and Purity

3.7.1. Dot Blot Analysis

For the verification of the performance of the anti-avidin and the anti-*S. cerevisiae* antibodies a dot blot experiment was conducted. 137.05 mg *S. cerevisiae* was suspended in 5 ml radioimmunoprecipitation assay (RIPA)-buffer containing 50 μl 100 mM phenylmethylsulfonyl fluoride (PMSF) and 10 μl 0.5 M dithiothreitol (DTT) and lysed with sonication for 1 min with 25% maximum power. It was kept on ice until use. Avidin, streptavidin and fluorescein isothiocyanate (FITC)-avidin were prepared according to manufacturers instructions. 5 μl of the yeast lysate, the avidin and streptavidin and 2.5 μl of the FITC-avidin were dotted on prewetted nitrocellulose membranes which were cut into eight stripes, four stripes for each primary antibody and its dilutions. The membranes were dried again at room temperature to fixate the proteins on the membranes. Afterwards the membranes were blocked with 5% skim milk powder in TBS-T at room temperature for 1 h or at 4 °C for 12 h. Subsequently, the membranes were washed 3 times with 50 ml TBS-T for 10 min and incubated with the primary antibody (anti-avidin or anti-*S. cerevisiae* at dilutions 1:100, 1:500, 1:1'000, 1:1'500 and 1:2'000 in 0.28 ml/cm^2) in TBS-T at room temperature for 1 h or at 4 °C for 12 h. The washing procedure was repeated and the secondary antibody (anti-rabbit) was applied at a dilution of 1:50'000 in 0.7 ml/cm^2 in TBS-T at room temperature for 1 h. After repeating the washing steps the membranes were incubated with ECL substrate for 5 min and the chemiluminescent signal was detected using a CCD camera.

3.7.2. SDS-PAGE

SDS-PAGE was performed under reducing conditions to validate the purity of the commercial antibodies. Gels were made of 5% acrylamide stacking gels and 10 % acrylamide separating gels according to Laemmli [119]. The antibodies were diluted to 1 mg/ml in phosphate bufferd saline (PBS) and 10 μl of each antibody was mixed with 10 μl of a twice concentrated sample buffer and incubated at 95 °C for 5 min. The total amount of 20 μl was loaded to the gel. For the run of the stacking gel 10 mA and for the separating gel 25 mA were applied. 10 μl of the prestained protein molecular weight marker were applied. Electrophoresis was carried out until the bromphenol blue front reached the bottom of the gel. The gels were stained with Coomassie Blue and destained with the destaining solution (67.5% H_2O_{dd}, 7.5% acetic acid and 25% methanol).

3.8. Relaxation Measurements

NMR relaxation measurements were performed at 21.7 MHz ($\approx$ 0.5 T). To determine the best size range for relaxation measurements commercial particles of different sizes were

investigated. The particles were SHP-10 (10 nm) and SHP-30 (30 nm) from Ocean Nanotech, FluidMag-D (50 nm) and FluidMag-Streptavidin (100 nm) from Chemicell GmbH. All particles were diluted using PBS (with 0.1% Tween 20 and 0.1 mg/ml BSA) to obtain equal concentrations of iron. T_2 relaxation time was measured continuously over 1 h without removing the sample from the magnet. Each T_2 relaxation time was determined using the Carr-Purcell-Meiboom-Gill (CPMG) pulse sequence with a echo time of 3 ms.

3.8.1. Avidin and Anti-Avidin-MNP System

FITC labeled avidin was used to visualise the interaction of avidin with the antibodies on the MNPs using fluorescence microscopy. FITC-avidin was prepared according to manufacturers instructions using PBS to give a final concentration of 2 mg/ml.
The anti-av MNP solutions were diluted to 2.2 mM Fe using PBS. 20 μl of this dilution were added to provided FITC-avidin samples of different concentrations and volumes were adjusted using PBS to give a total volume of 400 μl. The final concentrations of FITC-avidin ranged from 0.1 μg/ml to 200 μg/ml. Figure 3.3 shows a schematic drawing of the titration and the subsequent splitting of the samples for the parallel measurements of T_2 relaxation time and DLS.

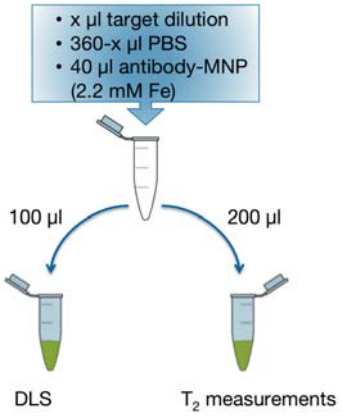

Figure 3.3.: Titration scheme for the detection of avidin and streptavidin using anti-avidin MNPs; the used concentrations are listed in Table 3.1

As a negative control all experiments were carried out with streptavidin instead of FITC-avidin. Used concentrations of FITC-avidin and streptavidin and the resulting ratio of the target to Fe ratio are given in Table 3.1. It was taken caution that the amount of antibody-MNP was equal in all preparations. This is important to prevent a change in the T_2 relaxation time due to a different MNP amount present in the solution.

With one half of the sample preparations the T_2 relaxation time was measured at 21.7 MHz ($\approx$ 0.5 T). After all samples were measured the first one was mixed again, the T_2 relaxation time was recorded and afterwards the sample was left in the magnet. T_2 relaxation time

target concentration in μg/ml	0.1	0.2	0.5	1	
avidin to Fe ratio	$6.8{\cdot}10^{-12}$	$1.4{\cdot}10^{-11}$	$3.9{\cdot}10^{-11}$	$6.8{\cdot}10^{-11}$	
streptavidin to Fe ratio	$7.5{\cdot}10^{-12}$	$1.5{\cdot}10^{-11}$	$3.7{\cdot}10^{-11}$	$7.5{\cdot}10^{-11}$	
target concentration μg/ml	2	5	10	20	40
avidin to Fe ratio	$1.4{\cdot}10^{-10}$	$3.4{\cdot}10^{-10}$	$6.8{\cdot}10^{-10}$	$1.4{\cdot}10^{-9}$	$2.7{\cdot}10^{-9}$
streptavidin to Fe ratio	$1.5{\cdot}10^{-10}$	$3.7{\cdot}10^{-10}$	$7.5{\cdot}10^{-10}$	$1.5{\cdot}10^{-9}$	$2.9{\cdot}10^{-9}$
target concentration μg/ml	60	80	120	160	200
avidin to Fe ratio	$4.1{\cdot}10^{-9}$	$5.4{\cdot}10^{-9}$	$8.1{\cdot}10^{-9}$	$1.1{\cdot}10^{-8}$	$1.4{\cdot}10^{-8}$
streptavidin to Fe ratio	$4.5{\cdot}10^{-9}$	$6.0{\cdot}10^{-9}$	$8.9{\cdot}10^{-9}$	$1.2{\cdot}10^{-8}$	$1.5{\cdot}10^{-8}$

Table 3.1.: Concentrations of targets in μg/ml and the resulting ratios of mM target to mM Fe as used in the titration experiments of target to anti-avidin MNPs; M(avidin) = 66 kDa; M(streptavidin) = 60 kDa

was measured again after 5 min and after 15 min of incubation in the magnet. Finally, the samples were mixed one more time and the T_2 relaxation time was recorded again. This procedure was repeated for every sample. For better comparison, the measured values for the T_2 relaxation times were normalised for each titration curve to the T_2 relaxation time of a antibody-MNP preparation without the addition of targets. All measurements were done in triplets.

With the other half of the samples DLS measurements were performed to verify the clustering of the MNPs due to the interaction of the coupled antibody with its target. Every sample was measured right after preparation using the standard protocol described in 3.4.2. Afterwards they were incubated on a NeFeB permanent magnet (N45, l x b x h = 8 x 4 x 1 cm^3) for 1 h. The bottom part of each sample was transfered carefully into a micro cuvette to prevent mixing and the hydrodynamic diameter was measured.

For long-term measurements the sample with the most pronounced signal change in T_2 relaxation time was freshly prepared and the T_2 relaxation time was recorded over 12 h every 2 min. In parallel automatic DLS measurements were performed over the same time period every 5 min. The same conditions were chosen for fluorescent microscopy.

3.8.2. *S. cerevisiae* and Anti-*S. cerevisiae*-MNP System

For the detection of *S. cerevisiae* the anti-*S. c.* MNPs were diluted to 2.2 mM Fe in PBS. Baker's yeast was purchased at the local supermarket and resuspended using PBS to give a

concentration of 20 mg/ml. The cell number was determined after diluting the sample to 0.1 mg/ml using a *Neubauer counting chamber*. The number derived out of the mean value of the 4 counting fields was multiplied by 10^4 and the dilution factor to give the cell concentration per ml. The titration experiments and the long-term experiments were carried out in the same way as described in section 3.8.1. The relaxation times were normalised to the the relaxation times detected for the anti-*S. c.* MNP of the same concentration alone, without the yeast. Measurements were done only once. DLS measurements were not made since the yeast cells are too big for a reliable detection via DLS measurements. The binding of the anti-*S. c.* MNP to the yeast cells was visualised using bright field microscope and TEM images. For TEM images the yeast cells were incubated at room temperature with the anti-*S. c.* MNP at a 20 pg Fe to cell ratio for 1 h. Afterwards, they were centrifuged at 10'000 rcf and 10 °C for 5 min, the supernatant was rejected, but a slight brownish colour was observed. The pellet was visible and brown due to the accumulated particles. The cells were washed using PBS and centrifuged again. The pellet was repeatedly brown. The colourless supernatant was rejected again and the cells were fixated by suspension in 3% glutaraldehyde in PBS. The cells were kept at 4 °C until further use.

3.8.3. K562 Cells and MNP System

Cell Culture

K562 cells were cultured at 37 °C, 10 % CO_2 atmosphere with Dulbecco's Modified Eagle Medium supplemented with 5% fetal calf serum and penicillin-streptomycin. For cultivation the cells were splitted every 7 days at a 1:50 ratio. For the relaxation measurements the cells were counted using a *Neubauer counting chamber* and loaded with commercial iron oxide magnetic nanoparticles with a silica coating and functionalised with streptavidin (diameter 100 nm). 10 mg/ml particle suspensions were given directly into the cell culture medium and the cells were loaded over night with 20 pg iron per cell. Afterwards the cells were centrifuged at 300 rcf at room temperature for 5 min. The cell pellets were resuspended in freshly prepared DMEM and the cells were counted again.

Verification of the Interaction between MNPs and Cells

The interaction of the particles with the cells was verified by performing transmission electron microscopy. For this the loaded and unloaded cells were washed with PBS and centrifuged at 300 rcf at room temperature for 5 min and resuspended in fixating buffer (3% glutaraldehyde in PBS, pH 7.2). They were kept at 4 °C until further use.

Relaxation Measurements

NMR experiments were performed using a NMR spectrometer with 250 MHz ($\approx$ 5.87 T). The T_2 relaxation time of K562 cells loaded with streptavidin MNP, unloaded K562 cells and streptavidin MNP alone was determined. 200 μl of loaded and unloaded K562 cells were separately transfered to five 5 mm NMR tubes. Each measurement was done in four replicates. $1.79 \cdot 10^5$ loaded cells and $1.94 \cdot 10^5$ unloaded cells were used for each experiment. For the MNP measurements alone 3.5 μl of streptavidin MNP were diluted in 1.5 ml PBS (with 1% BSA, 0.1% Tween 20) to obtain the same iron concentration compared to loaded K562 cells. T_2 values were obtained after calibration from 15 data points generated with a Carr-Purcell-Meiboom-Gill (CPMG) pulse sequence with echo times of 5 ms for unloaded cells and loaded cells and 1 ms for MNP alone.

4. Results

In the first section of this chapter, the characterisation methods of the manufactured magnetic nanoparticles and their results are presented. In the second section the purity of the applied antibodies used for the detection of avidin and *S. cerevisiae* is proven. Next to this, the sensitivity of the antibodies is also described. The third section supplies results of the relaxation measurements for the proof of principle target avidin using anti-av MNPs. In addition, the results of the detection via relaxation measurements of the application target *S. cerevisiae* with anti-*S. c.* MNP as well as for the loading of K562 cells with commercial MNP are given. Furthermore, results from relaxation measurements using commercial MNP of different diameters leading to the desired size range of 10 nm-15 nm for the manufactured nanoparticles are presented.

4.1. Characterisation of Functionalised Magnetic Nanoparticles

4.1.1. Core Characterisation

Mössbauer Spectroscopy

Mössbauer spectroscopy yields very precise information about the chemical, physical and magnetic properties of a material. The source for this information lies in the recoilless gamma ray emission and absorption of nuclei in atoms, the Mössbauer effect, when they undergo varieties of energy level transitions. These energy levels depend on the surrounding environment of the nuclei. The transition between energy levels is often associated with the absorption or emission of gamma rays. Due to the different electric and magnetic environment of the nuclei these energy levels can be splitted or changed. The differences in resonance depending on the surrounding of the nuclei can only be observed if the recoil of the free nucleus during emission or absorption is overcome. The Mössbauer effect states, that if the atoms are in a solid matrix, like a crystal lattice, the effective mass of the nucleus is much greater and the recoil is not occurring. Therefore, the emitted and absorbed gamma rays have the same energy. Thus, if the emitting and absorbing nuclei are the same, the transition energies are identical and in resonance. This effect is isotope specific. The main nucleus examined using Mössbauer spectroscopy is iron. It can be found in nature in three valence states: Fe^{0}, Fe^{2+} and Fe^{3+}, and in different types of coordination polyhedra (trigonal, tetrahedral, octahedral, for instance).

For the detection of iron oxide with Mössbauer spectra a ^{57}Co source is used which decays

to an unstable ^{57}Fe. This again releases a gamma ray of 14.4 keV which will be completely absorbed by other iron nuclei if they are in a crystal lattice of the identical surrounding environment. Iron nuclei in different environments show resonance if the energy of the emitted gamma ray is varied just a little. This is accomplished by moving the source in an oscillating manner with a speed in the range of mm/s and recording the spectrum in velocity steps. A peak in the Mössbauer spectrum arises where the modulated gamma ray matches the energy of a nuclear transition in the absorber and the absorber itself is able to release a gamma ray. The energy levels in the absorber nuclei are influenced by their surrounding environment and can be modified in three different ways: by the isomer shift, the quadrupole splitting and the magnetic splitting. Taking all three influences together the different iron oxides, especially magnetite and maghemite, can be differentiated.

For the determination of the oxidation state of the manufactured MNPs Mössbauer spectroscopy was performed at two different temperatures and at different ageing points of the magnetic nanoparticles. The first spectra were taken at 4.2 K and 298 K of freshly prepared MNPs in diethylene glycol (Figures 4.1 (a) and (b)). For Figure 4.1 (b) the sample was fixated using a two component glue. Spectra of particles which were previously washed with 1 M HNO_3 at 4.2 K and 298 K are depicted in Figures 4.1 (c) and (d), respectively. Spectra of particles after one week of preparation are presented in Figures 4.1 (e) and (f). Both particle preparations were freeze-dried before the measurements.

The biggest difference between the spectra at 4.2 K is evident between the Figures 4.1 (a) and (c). The shoulder peaks on the left side of the spectra (indicated by asterisk) presenting the presence of magnetite are getting smaller concluding that the magnetite is oxidised to maghemite during the washing process of the particles with 1 M HNO_3 right after their preparation. The spectra at 298 K without an applied magnetic field give no information about the oxidation states of the iron atoms due to the loss of the hyperfine structure (Figures 4.1 (d) and (f)). In contrast, the application of a magnetic field at 298 K results in the reconstitution of the information about the oxidation state of the iron nuclei (Figure 4.1 (b)). The loss of the hyperfine structure and therefore the loss of resonant energy absorption in Figures 4.1 (d) and (f) proves the very small size of the particles. Taken together the Mössbauer spectra reveal the ageing of the MNP by the loss of the magnetite signal and the increase of the maghemite signal over time. At room temperature the applied magnetic field of 750 mT leads to a reconstitution of the spectra presenting a simple method to obtain spectra of single domain particles at ambient temperatures.

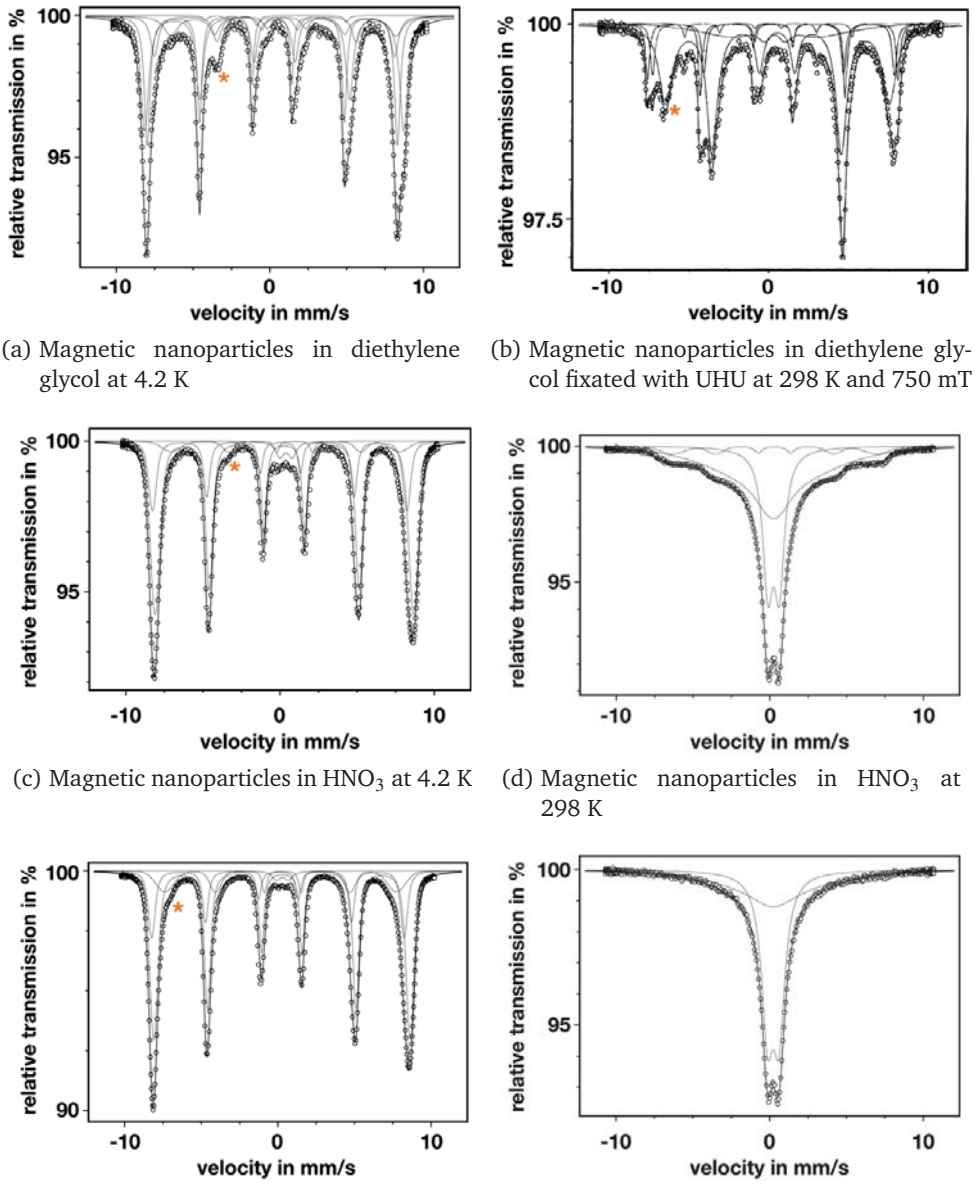

(a) Magnetic nanoparticles in diethylene glycol at 4.2 K

(b) Magnetic nanoparticles in diethylene glycol fixated with UHU at 298 K and 750 mT

(c) Magnetic nanoparticles in HNO_3 at 4.2 K

(d) Magnetic nanoparticles in HNO_3 at 298 K

(e) Magnetic nanoparticles one week after HNO_3 treatment at 4.2 K

(f) Magnetic nanoparticles one week after HNO_3 treatment at 298 K

Figure 4.1.: Mössbauer spectra of magnetic nanoparticles at different times of ageing; (a) and (b) right after manufacturing in diethylene glycol; (c) and (d) after washing with 1 M HNO_3 and lyophilised; (e) and (f) one week old magnetic nanoparticles washed with 1M HNO_3 and lyophilised; (a), (c) and (e) are taken at 4.2 K; (b), (d) and (f) are taken at 298 K; (b) was taken with an applied magnetic field of 750 mT. The asterisks indicate the shoulder peaks from the spectra of magnetite, which diminish with the ageing of the particles.

Electron Diffraction Pattern

High resolution TEM revealed the lattices of the MNPs crystals (Figures 4.3 (b) and (c)). Furthermore, electron diffraction patterns were obtained of the crystals during the preparation of TEM images. These patterns are obtained from the backscattering of the electron beam by crystalline structures in the TEM. The patterns obtained are unique for each type of crystal lattice. Due to the high crystalline structure of the cores of the MNP the electron diffraction pattern obtained is comprised of different rings equalling the ones for iron oxides (Figure 4.2).

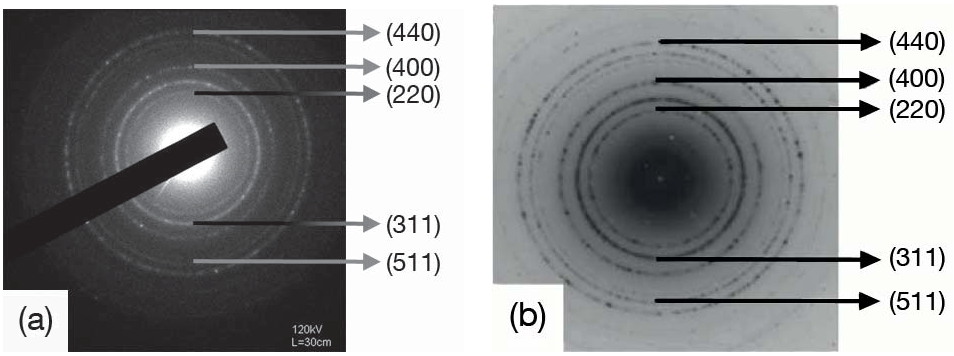

Figure 4.2.: Electron diffraction pattern of a magnetic nanoparticle crystal obtained by transmission electron microscopy (a); The diffraction pattern reveals the expected iron oxide lattice compared to the literature (b).

4.1.2. Size Determination

Core Size by Transmission Electron Microscopy

TEM images of the MNPs were made at the different stages of their manufacturing to visualise the core and the different coatings. Figure 4.3 (a) depicts magnetic nanoparticles after manufacturing with a 50'000x magnification. Figure 4.3 (b) presents particles after the coating with TEOS at a 250'000x magnification and Figure 4.3 (c) MNP with the functionalisation with APTES, which are taken with a 500'000x magnification. They also reveal the lattices of the magnetic nanoparticle crystals. In both images the particles show an even distance from each other. Around the particles a shade of grey different from the background can be seen. These structures depict a coating but lack the crystalline structure of SiO_2. This was verified by obtaining dark-field TEM pictures due to the diffraction contrast from four different positions of the aperture. In these images only crystalline structures are visible and appear bright. By obtaining dark-field and bright-field images and overlaying them, the size of the crystal lattice and of the coating layer, if it is crystalline can be obtained. If the coating is not crystalline there will be no difference in the overlays. Figure 4.4 (b) shows one example of an overlay of four dark-field images of MNP with TEOS and the ac-

cording bright-field image. Compared with the dark field image (Figure 4.4 (a)) there is no difference visible, concluding, the coating applied is not fully condensed TEOS.

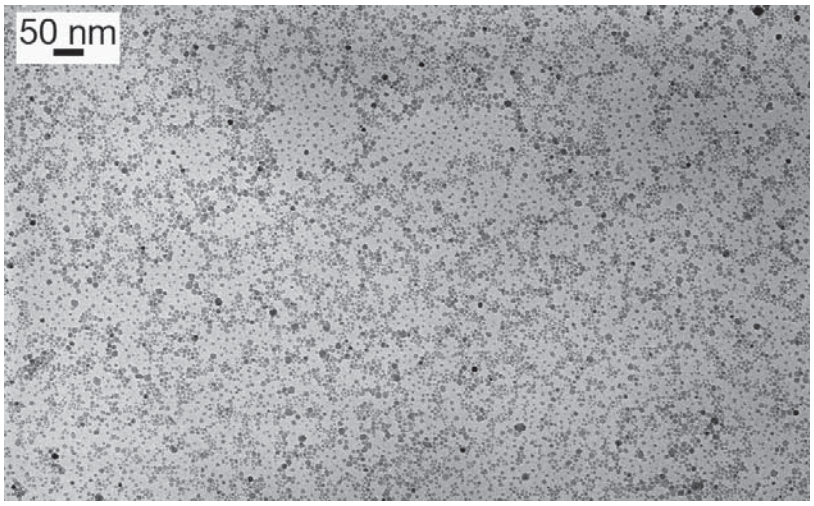

(a) Magnetic nanoparticles after manufacturing (50'000x magnification, 1'500x resolution)

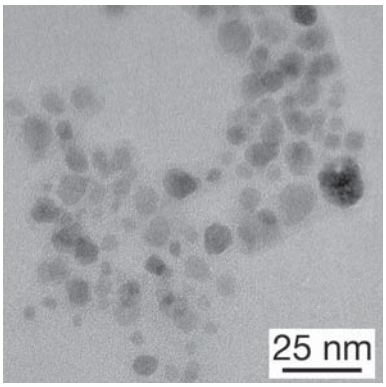

(b) Magnetic nanoparticles with the first coating made of TEOS (250'000x magnification, 2'603x resolution)

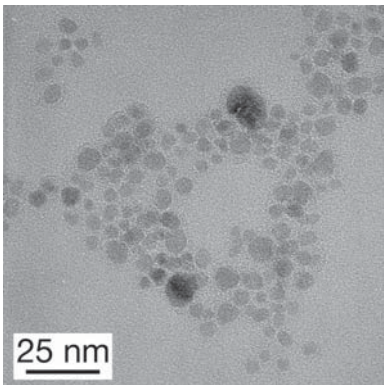

(c) Magnetic nanoparticles with the functionalisation made of APTES (500'000x magnification, 1'200x resolution)

Figure 4.3.: Transmission electron microscopy images of magnetic nanoparticles at the different stages of their manufacturing

Figure 4.5 provides the acquired size distribution of the magnetic cores from Figure 4.3 (a) as obtained by particle analysis using *ImageJ*. The mean core diameter obtained by fitting a log-normal distribution is 5.76$\pm$1.69 nm (n = 3'478).

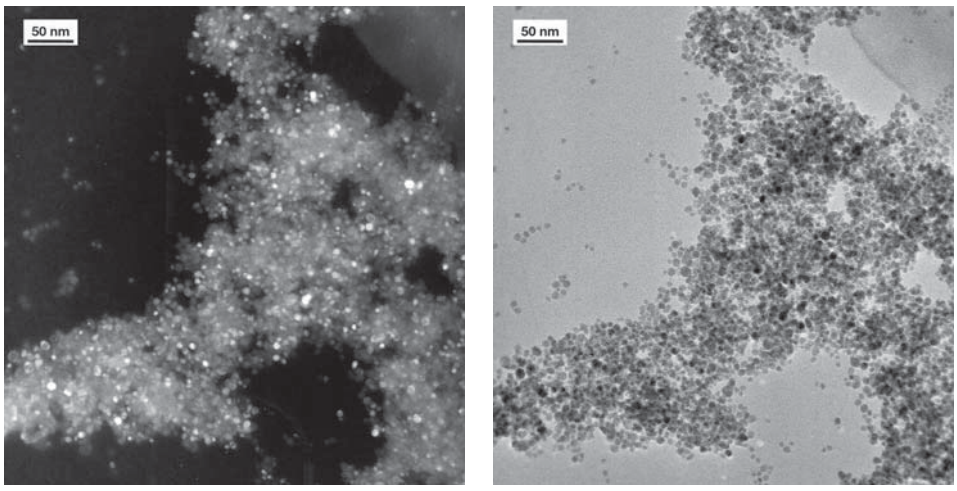

(a) Darkfield TEM image

(b) Overlay of a bright-field and four dark-field TEM image

Figure 4.4.: Darkfield and overlay of a bright-field and four dark-field transmission electron microscopy images of magnetic nanoparticles with TEOS coating and APTES functionalisation (120'000x magnification)

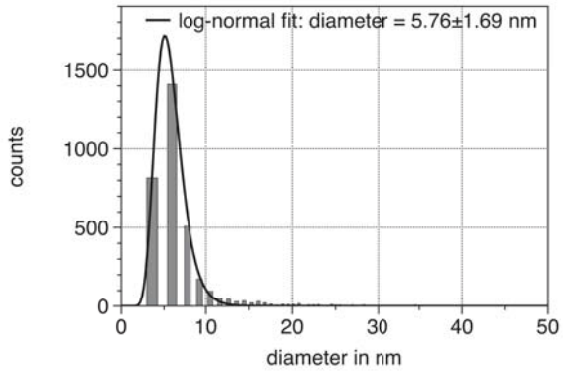

Figure 4.5.: Log-normal distribution of the core sizes of the magnetic nanoparticles obtained by transmission electron microscope images from Figure 4.3 (a) using *ImageJ* (n = 3'478)

Hydrodynamic Size by Dynamic Light Scattering

Dynamic light scattering relies on the Brownian movement of particles in a colloidal solution. A laser beam propagates through this solution and its scattered intensity is measured at different time points leading to the determination of the moving speed of the particles. From the Stokes-Einstein equation the mean radius of the particles is obtained assuming the particles are spheres and non-interacting:

$$R_h = \frac{k_B T}{6\pi\eta D} \tag{4.1}$$

where R_h is the mean hydrodynamic radius of the particles, D their diffusion coefficient and η the shear viscosity of the solvent. From the change of the scattered light with time a correlation function of this scattering can be calculated, which is the basis for the further determination of the hydrodynamic diameter (Figure 4.6).

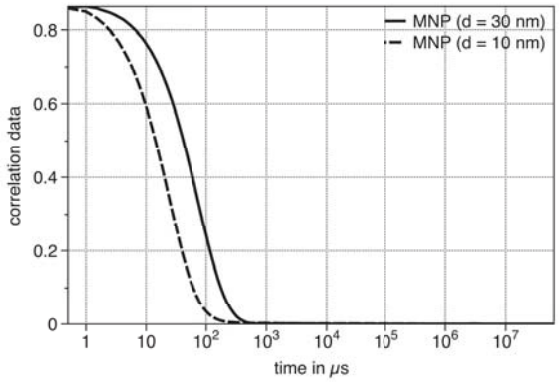

Figure 4.6.: Example for the correlation function of two colloidal suspensions of particles of different sizes

Figure 4.6 depicts the correlation functions of particles with different sizes. The longer the plateau at the start of the function, the bigger is the size of the particle. The steeper the decrease of the function the more monodisperse is the particle solution.

For a non ideal suspension, the correlation function will be fitted with a polynomic function of the second degree

$$log(G) = a + bt + ct^2. \tag{4.2}$$

Parameter b equals the *Z-average* diffusion coefficient, and parameter c is an index for the polydispersity of the suspension. Both parameters together are used to calculate the *polydispersity index* (*PdI*-value):

$$PdI = \frac{2c}{b^2}. \tag{4.3}$$

For an ideal colloidal suspension the PdI value equals 0, for spherical, reasonably narrow monomodal samples it is < 0.1 [120].

Depending on the particle sizes, two different theories are employed. Is the particle much smaller than the wavelength of the laser, Rayleigh scattering is used for the determination of the particle diameter.

According to it the scattering intensity of a particle is proportional to the sixth power of its diameter

$$I = I_0 \frac{1+\cos^2\theta}{2R^2}\left(\frac{2\pi}{\lambda}\right)\left(\frac{n^2-1}{n^2+2}\right)^2\left(\frac{d}{2}\right)^6 \tag{4.4}$$

where I is the intensity of the scattered light, R is the distance to the particle and d is the diameter of the particle. For particles of the same size as the laser wavelength or bigger the Mie-Theory is applied. This theory is also used to convert the obtained intensity distribution into a volume distribution. This distribution again is further converted into a number distribution. The size distribution obtained by DLS measurements will be presented when applicable in the following in two different ways: intensity and number weighted. The intensity weighted size distribution is the fundamental size distribution generated by DLS.

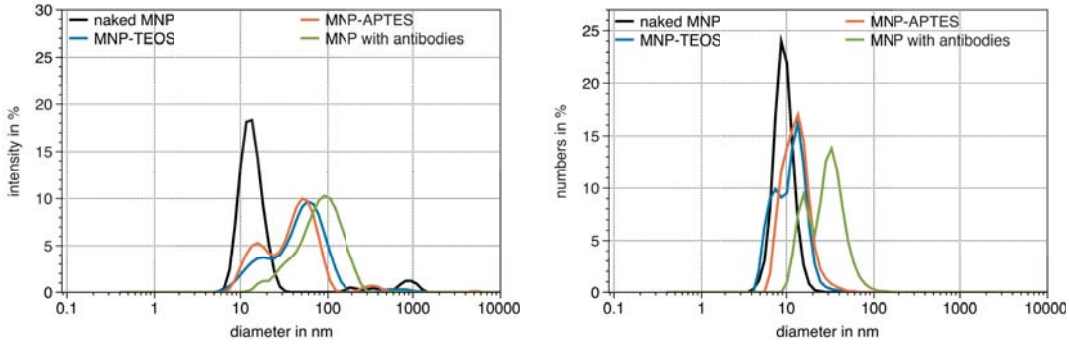

(a) Intensity weighted size distribution (b) Number weighted size distribution

Figure 4.7.: Differently weighted size distributions of the magnetic nanoparticles at the three different stages of manufacturing and functionalised with antibodies obtained by dynamic light scattering measurements; presented are average values for each manufacturing state. Mean values and standard deviations of the diameter for naked MNPs are intensity weighted 14.02 ± 1.81 nm and number weighted 9.73 ± 1.09 nm (n = 3). For MNP-TEOS they are intensity weighted 59.63 ± 18.05 nm, number weighted 11.78 ± 4.09 nm (n = 5). For MNPs-APTES coating the intensity weighted mean diameter is 39.14 ± 18.42 nm and the number weighted diameter is 13.65 ± 3.64 nm (n = 6). For the functionalised MNPs they are 96.6 ± 35.97 nm and 30.14 ± 13.08 nm, respectively (n = 5).

Figure 4.7 depicts intensity (a) and number (b) weighted size distributions of naked MNPs, with TEOS coating and with APTES and antibody functionalisation. The differences between both presentations are first the mean sizes, which decrease from the intensity to the number weighted size distribution, and second the shape of the curves, which are log-normal distributed in the intensity weighted presentation and loose that shape in the number weighted distribution. In both presentations a clear increase in diameter between the different manufacturing stages can be seen. Depicted are average values for n = 3 for the naked MNP, n = 6 for MNP-APTES, n = 5 for MNP-TEOS and MNP with antibodies. This is

due to the fact, that each batch of naked MNP gives two different batches of MNP-TEOS and each batch of MNP with TEOS yields at least one batch of MNP-APTES. The average values were calculated by the software of the DLS instrument. The mean values and standard deviations of the main peaks and the PdI values for all manufacturing stages can be found in Table 4.1. The PdI values range between 0.23 and 0.26 indicating that monodispersity compared to ideal monodisperse suspensions is not yet reached.

preparation	diameter in nm (intensity weighted)	diameter in nm (number weighted)	PdI
naked MNP	14.02 ± 1.81	9.73 ± 1.09	0.24
MNP-TEOS	59.63 ± 18.05	11.78 ± 4.09	0.26
MNP-APTES	39.14 ± 18.42	13.65 ± 3.64	0.23
MNP with antibodies	96.6 ± 35.97	30.14 ± 13.08	0.23

Table 4.1.: Intensity and number weighted size distributions of the different manufacturing states obtained by DLS measurements ; Quantitative data is represented as mean $\pm$ standard deviation (n = 3 for naked MNP, n = 6 for MNP-APTES, n = 5 for MNP-TEOS and MNP with antibodies)

The naked MNP with 9.73 nm mean diameter and the MNP-TEOS with 11.78 give a TEOS-coating of 1.025 nm. The difference in mean diameters between MNP-TEOS and MNP-APTES (13.65 nm) is 1.87 nms giving an additional coating of APTES of 0.94 nm, or altogether a coating of 1.96 nm. The functionalisation with antibodies (mean diameter 30.14 nm) leads to an increase in the diameter of the particles of 16.49 nm or an additional monolayer of antibodies of 8.25 nm thickness. The size of an antibody is of approximately 7 nm [121]. To sum up the particles are coated with a very thin layer of 1.96 nm and are covalently bound with a monolayer of antibodies of 8.25 nm. A schematic drawing is shown in Figure 4.8.

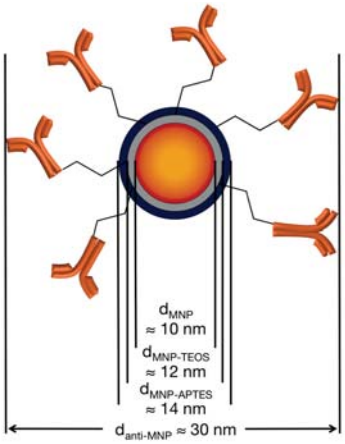

Figure 4.8.: Schematic drawing of a manufactured magnetic nanoparticle with the TEOS coating, the APTES funtionalisation and the functionalisation with antibodies; The hydrodynamic diameters are indicated for every manufacturing step.

4.1.3. Surface Characterisation

Zeta Potential

The Zeta potential describes the electric potential between the bulk dispersion medium and the inter-facial double layer of ions surrounding a dispersed particle. The value of the Zeta potential is related to the stability of a colloidal solution. For absolute values greater than 20 mV, the manufactured batches of MNPs with coating and functionalisation were optical proven to be colloidal stable suspensions. Therefore, the repulsive forces between the particles in the suspension were large enough to withstand aggregation and the particle suspensions showed no visible aggregation after six months.

Figure 4.9 depicts the Zeta potential for the magnetic nanoparticles at the different stages of the manufacturing process. Presented are values of three manufactured batches of naked MNP, of five different batches of MNP-TEOS and of six different batches of MNP-APTES. The change in the Zeta potential of the three manufacturing stages can clearly be seen. The decline of the curve of the naked magnetic nanoparticles lies in the neutral pH range leading to their stability in acidic and alkaline pH ranges. In comparison, the curve of the particles coated with TEOS is shifted to the more acidic pH range creating stability at the neutral pH range. The particles with the functionalisation made of APTES have a zeta potential between both previous manufacturing stages and are like the naked MNPs not colloidal stable at the neutral pH range. The further functionalisation reaction with antibodies is carried out at pH 8.17 making the APTES functionalisation ideal for the preservation of the colloidal stability during functionalisation. The point of zero charge is for naked MNPs pH 6.65, for MNP-TEOS pH 2.85 and for MNP-APTES pH 5.29.

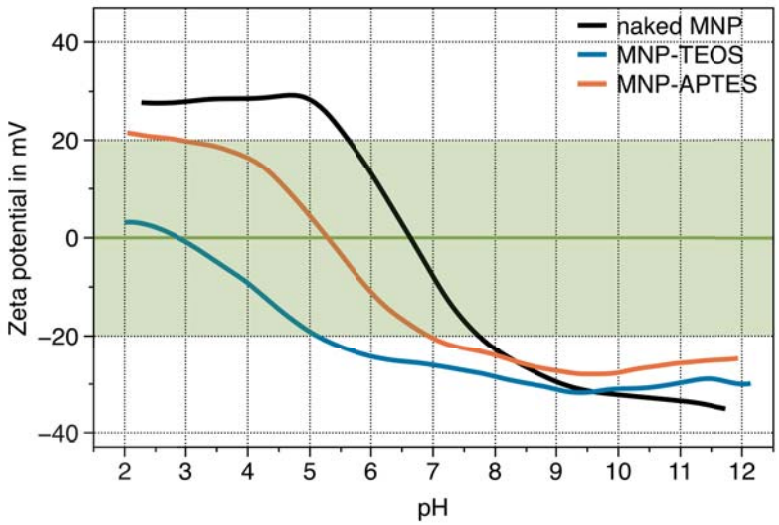

Figure 4.9.: Change of the Zeta potential with the pH of the solution of the manufactured magnetic nanoparticles with different surface modalities; The Zeta potential range where the suspensions are colloidal stable is green highlighted. n = 3 batches for naked particles, n = 5 batches for MNP-TEOS and n = 6 batches for MNP-APTES. Presented are the mean values.

Fouriertransformed Infrared Spectroscopy

Fouriertransformed infrared spectroscopy (FT-IR) detects the surface characteristics of the magnetic nanoparticles. After coating with organic substances like TEOS and APTES this surface modification can be detected due to the vibration and rotation of the molecules under the influence of infrared light [122]. For comparison, Figure 4.10 presents spectra of TEOS and APTES as well as spectra of the particles at the different manufacturing states.

From 3'100-3'650 cm^{-1} and around 1'600 cm^{-1} the stretching vibration of the primary amine stretch and of the hydroxyl group appear in wide bands. However, the absorption of the hydroxyl group is greater than the one caused by the amine groups and therefore the stretching of the amine group cannot be distinguished in the particle preparations due to the hydroxyl group band (Figure 4.10 D). The C-H stretching of the methyl group of the ethanol appearing after the condensation of the silanes is almost not visible as well (2'850-3'000 cm^{-1}). In contrast, the stretching of the C-O bond of the primary alcohol (1'020-1'055 cm^{-1}), of the Si-O-Si bonds (1'075-1'095 cm^{-1}), of the Si-O-C bonds (1'080-1'110 cm^{-1}) as well as the stretching of the Fe-O bonds in the iron oxide lattice (500-700 cm^{-1}) can be seen nicely. The bending vibration of the C-H of the methylene bridge (1'405-1'465 cm^{-1}) can be seen in naked MNPs as well as in the MNP-APTES.

Taken together the FT-IR spectra show, like the Zeta potential measurements, that both silanes, TEOS and APTES, were successfully applied to the MNP. The lack of the pronounced signal of the methylgroups of the ethanol at 2'850-'3000 cm^{-1} (Figure 4.10 B and D) could

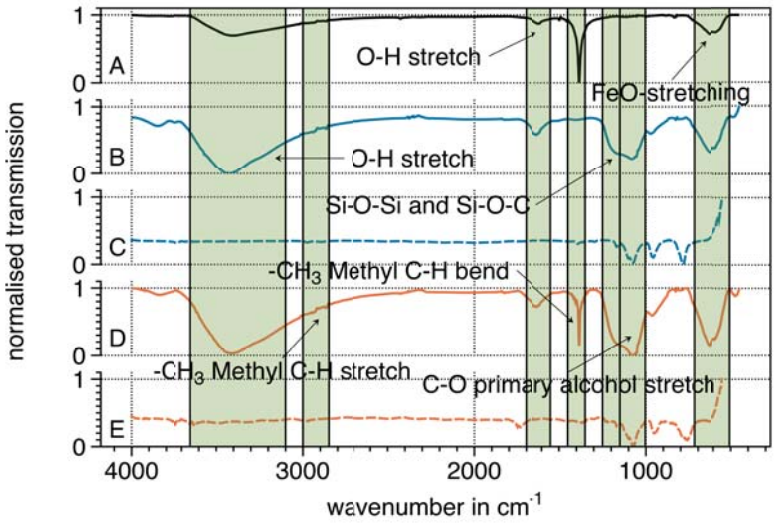

Figure 4.10.: FT-IR-spectra of the manufactured magnetic nanoparticles at the different stages of manufacturing and of the coating material alone; A: magnetic nanoparticles without any coating; B: magnetic nanoparticles with TEOS coating; C: TEOS; D: magnetic nanoparticles with TEOS and APTES coating; E: APTES; For the specific groups the ranges are green highlighted.

be a hint of a silane not fully condensed to SiO_2.

4.1.4. Magnetism and Relaxivity Determination

Magnetisation, Magnetic Moments and Size

M(H) measurements of the magnetic nanoparticles between -3.5 T and 3.5 T were done at all manufacturing stages (Figure 4.11). At a closer look hysteresis seems to appear (inlet Figure 4.11). However, this is an artefact from the measurement process and is not caused by the magnetic nanoparticles. All curves appear, except for the two weeks old particle preparation, in the same value range. The fresh preparation of naked MNPs gives a higher magnetic moment and a higher saturation magnetisation as the two months old preparation. Table 4.2 displays the saturated magnetisation, in two different units for better comparison, and the magnetic moment for each manufacturing state.

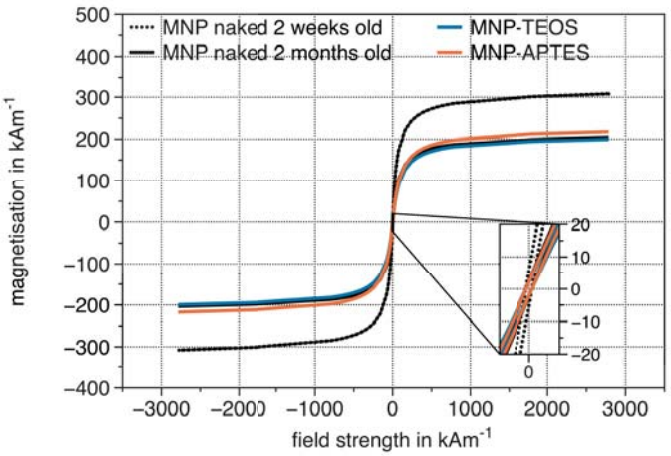

Figure 4.11.: Magnetisation curves of the manufactured magnetic nanoparticles normalised to the weight obtained by M(H) measurements from -3.5 T to 3.5 T

sample	μ_S in μAm^2	M_S in kAm^{-1}	M_S in Am^{2}kg^{-1}
MNP naked 2 months old	289	210	45
MNP naked 2 two weeks old	320	315	63
MNP TEOS	276	205	41
MNP TEOS APTES	324	220	45

Table 4.2.: Magnetic moments and saturated magnetisations of the manufactured magnetic nanoparticles at different stages of their manufacturing as obtained by M(H) measurements from the curves of Figure 4.11.

Magnetic Particle Spectroscopy was carried out for all manufacturing stages of the MNPs at 25 mT. For comparison the spectrum for the commercially available contrast agent Resovist is also plotted (Figure 4.12). Since the manufactured particles are small the phase of the measured k^{th} harmonic, stays at first around zero and drops then even below the values for Resovist (bottom figures of Figure 4.12). The amplitude A_k of the manufactured particles starts lower compared to Resovist and decreases faster (upper figures of Figure 4.12).

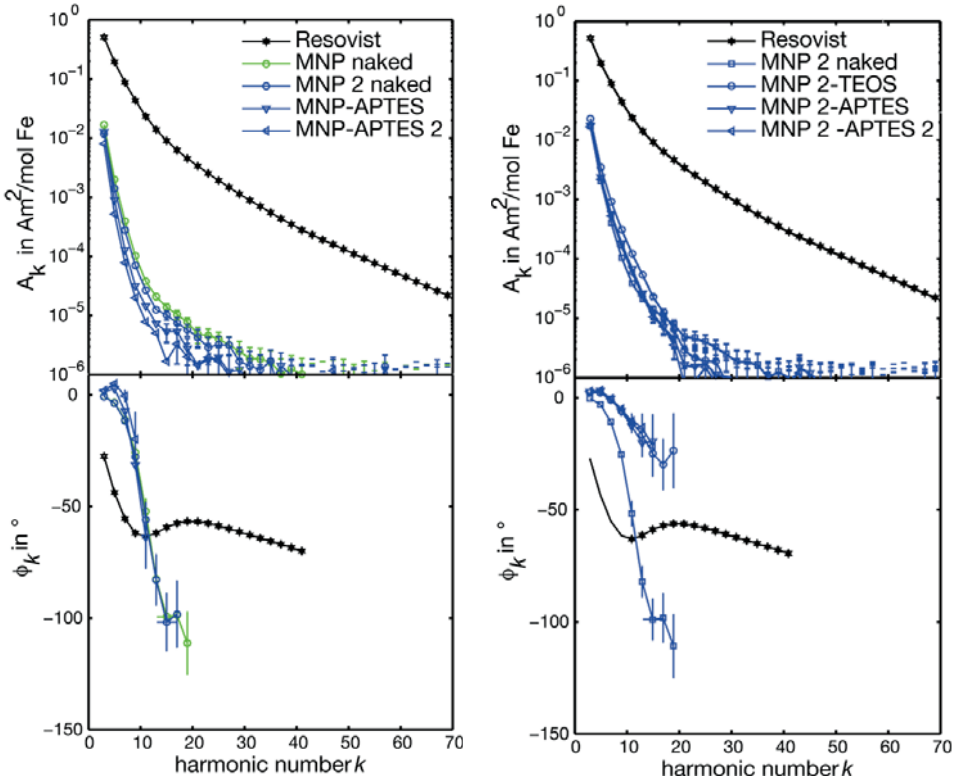

(a) First batch of magnetic particles with different coatings

(b) Second batch of magnetic nanoparticles with different coatings

Figure 4.12.: magnetic particle spectroscopy of different batches of magnetic nanoparticles at different stages of manufacturing

Magnetisation and Size

NMR-D Profiles were taken of naked MNP and of MNP-TEOS after one week of preparation. Figure 4.13 shows profiles of nicely dispersed nanoparticles. For interpretation of the data the fitting algorithm of Laurent et al. was employed [3, 29]. Briefly, as indicated in Figure 4.13 (a), the average radius, r, is described at high magnetic fields from the inflection point of the fitting by

$$\omega_I \cdot \tau_D \sim 1, \tag{4.5}$$

with ω_I being the proton angular frequency and τ_D the translational correlation time. This estimate can be made since here the relaxation rate only depends on τ_D. Due to

$$\tau_D = \frac{r^2}{D}, \tag{4.6}$$

r can be calculated. The saturation magnetisation, M_s, is acquired at high fields from the

relation,

$$M_s \sim \sqrt{\frac{R_{max}}{C\tau_D}}, \tag{4.7}$$

where C is a constant and R_{max} is the maximal relaxation rate. The presence of a dispersion at low fields indicates a low anisotropy energy, E_a, of the crystals.
For the naked MNPs in Figure 4.13, E_a is lower compared to the anisotropy energy of the MNPs with TEOS. The magnetisation of the naked nanoparticles is 78 Am^2kg^{-1} and for the particles coated with TEOS 45 Am^2kg^{-1}. The diameters obtained by the fitting are 10.1 nm for the naked MNPs and 12.4 nm for the MNP-TEOS.

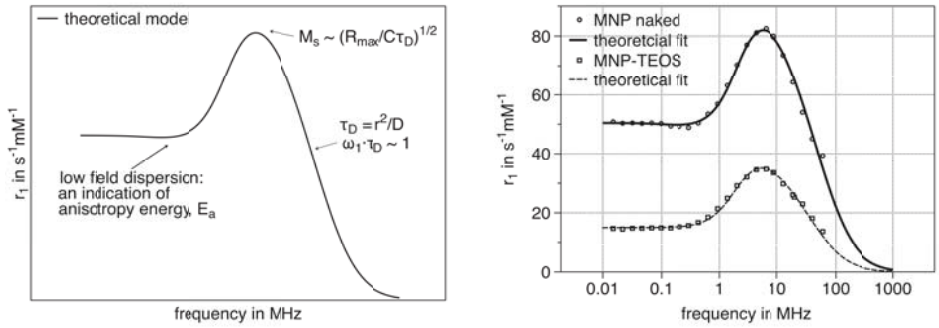

(a) Theoretical model (b) Measured data and fittings

Figure 4.13.: Theoretical model of NMR-D profiles with indicated parameters of the anisotropy energy E_a, the magnetisation, M_s, and the radius, r, obtained from the model (a) [29]; NMR-D profiles of naked magnetic nanoparticles and magnetic nanoparticles coated with TEOS (b)

Relaxivity of Manufactured MNPs

Relaxivity was determined for all manufacturing stages of the MNPs. Figure 4.14 depicts the plot of the relaxation rate of the MNP corrected by the relaxation rate of the solvent against the iron concentration. The slope of this curve equals the relaxivity of the MNP. Table 4.3 lists the relaxivities of the manufactured MNP.

sample	r_2 in $mM^{-1}s^{-1}$
MNP naked	23
MNP TEOS	49
MNP TEOS APTES	55

Table 4.3.: Relaxivities of the different magnetic nanoparticle preparation stages; Data obtained from slopes of curves like Figure 4.14.

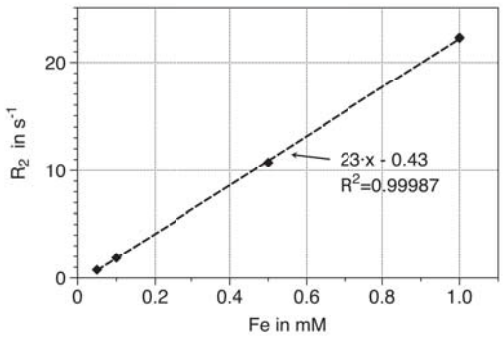

Figure 4.14.: Determination of the relaxivity of manufactured magnetic nanoparticles

4.2. Validation of Antibody Functionality

To proof the function and purity of the antibodies used for the detection of avidin and *S. cerevisiae* Dot Blot analysis (Figure 4.15) and SDS-PAGE (Figure 4.16) were performed.

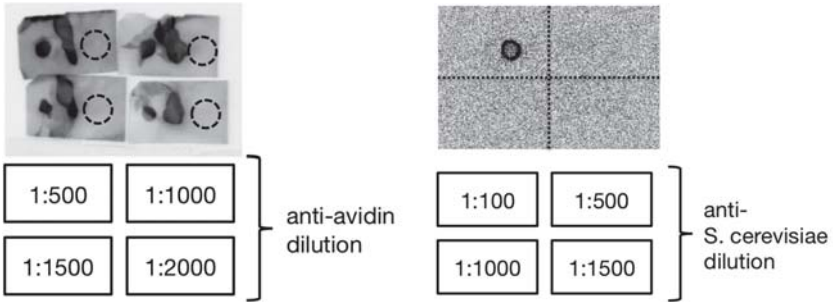

(a) Anti-avidin antibody (b) Anti-*S. cerevisiae* antibody

Figure 4.15.: Dot Blots for the verification of the functionality of the antibodies

Figure 4.15 depicts Dot Blots for anti-avidin and anti-*S. cerevisiae* antibodies. Both antibodies were tested in different dilutions to increase the chance of getting a chemiluminescence signal. For the anti-avidin antibody, avidin, FITC-avidin and streptavidin were dotted from left to right on nitrocellulose membranes (Figure 4.15 (a)). Clearly visible is the chemiluminescent signal for avidin as well as for FITC-avidin but no signal for streptavidin providing the proof of no cross-reactivity of the antibody with streptavidin. The signal in the Dot Blot for the anti-*S. cerevisiae* antibody is weaker compared to the signals of the anti-avidin antibody. The anti-avidin antibody gives signals down to a 1:2'000 dilution, whereas the anti-*S. cerevisiae* antibody gives a weak signal at a 1:100 dilution. This finding indicates a better performance of the anti-avidin antibody over the anti-*S. cerevisiae* antibody.

The performed SDS-PAGE of both antibodies proves their purity (Figure 4.16). No BSA has been added to the proteins by the manufacturer for their stabilisation. The bands in lane

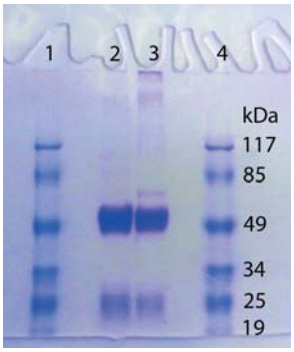

Figure 4.16.: SDS-PAGE of both antibodies for the verification of their purity; lanes 1 and 4: protein standard ladder; lane 2: anti-*S.cerevisiae* antibody; lane 3: anti-avidin antibody

2 and 3 at 25 kDa comprise the short chains of the antibodies. The bands above 49 kDa are the longer chains of the antibodies [123]. The bands hardly visible in lane 3 above the prominent band are most probably due to rearrangements of long and short chains of the antibody after the disulfide bonds have been broken during the sample preparation for SDS-PAGE.

4.3. Relaxation Measurements

4.3.1. Avidin Anti-Avidin-MNP System

Titration

For the determination of the most suitable parameters for the incubation of the antibody-MNPs with their targets and their best ratio the T_2 relaxation times were recorded right after preparation of the samples, after mixing, after 5 min and 15 min of incubation in the 0.5 T magnetic field of a relaxometer of 21.7 MHz and after mixing one more time. The results for the FITC-avidin and anti-av MNP are shown in Figure 4.17 (a) the results for the negative control with streptavidin instead of FITC-avidin are shown in Figure 4.17 (b). The difference in the development of the T_2 relaxation times can clearly be observed. Whereas the data for the incubation with streptavidin stays at a constant level, the T_2 relaxation time for the incubation with FITC-avidin decreases down to 50% right after preparation to increase again during the incubation in the magnetic field. For both setups the differences in the T_2 relaxation times between the preparation and the incubation of 15 min in the magnetic field are shown in Figure 4.17 (c). As expected the difference for the incubation with streptavidin is less then 20%. In contrast the difference for the incubation with avidin goes up to over 60% suggesting a specific interaction between the FITC-avidin and the anti-av MNPs. In this set-up, 5 μg/ml corresponding to a molar ratio of FITC-avidin to Fe of $3.4 \cdot 10^{-4}$ is the concentration of FITC-avidin leading to the largest difference in the

T_2 relaxation time between the preparation of the sample and 15 min of incubation in a magnetic field. However, at a FITC-avidin concentration of 2 μg/ml, which corresponds to a molar ration of FITC-avidin to Fe of $1.4 \cdot 10^{-4}$, a difference of 25% in the T_2 relaxation time between the measurement after preparation and 15 min incubation time in the magnet can already be seen.

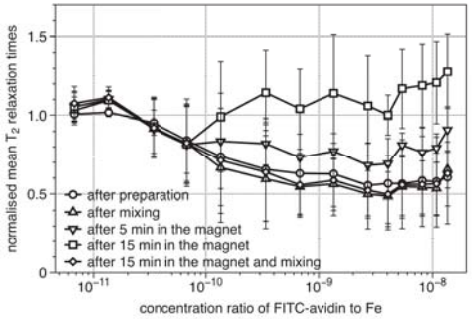

(a) Normalised T_2 relaxation times of anti-avidin MNPs incubated with FITC-avidin

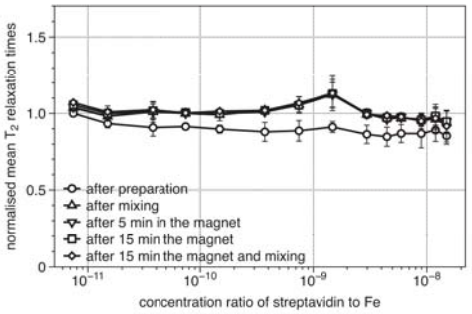

(b) Normalised T_2 relaxation times of anti-avidin MNPs incubated with streptavidin

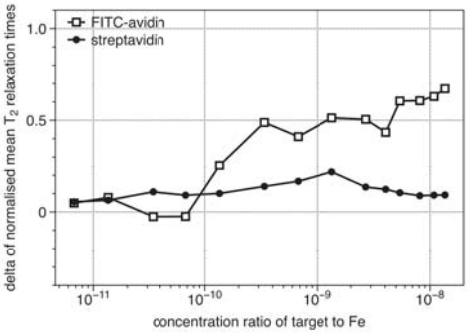

(c) Differences of normalised T_2 relaxation times for the incubation with FITC-avidin and streptavidin

Figure 4.17.: Normalised T_2 relaxation times of anti-avidin-MNPs incubated with different concentrations of FITC-avidin and streptavidin after different parameters for incubation; (c) depicted are the differences between the preparation of the sample and after 15 min of incubation in the magnetic field of a relaxometer at 21.7 MHz ($\approx$ 0.5 T) of anti-avidin MNPs incubated with streptavidin or FITC-avidin.

Parallel to these T_2 relaxation time measurements the size distribution was also recorded using DLS measurements (Figure 4.18). DLS measurements were performed before (Figures 4.18 (a) and (c)) and after the incubation of the samples on a NeFeB magnet at room temperature for 1 h (Figures 4.18 (b)) and (d)). Shown are intensity weighted DLS measurements for the incubation with different concentrations of FITC-avidin (Figures 4.18 (a) and (b) and streptavidin (Figures 4.18 (c) and (d)). By comparing the DLS data of the incubation of anti-av MNP with avidin and streptavidin, the size distribution stays constant for the reactions with streptavidin leading to the assumption that the size of the particles was not influenced by the incubation with streptavidin nor the incubation with streptavidin

on the magnet (Figures 4.18 (c) and (d)). Conversely, an increase in the size distribution of the incubation with FITC-avidin can be seen. This increase appears for the increase in the FITC-avidin concentration as well as for the incubation on the NeFeB magnet (Figure 4.18 (a) and (b)).

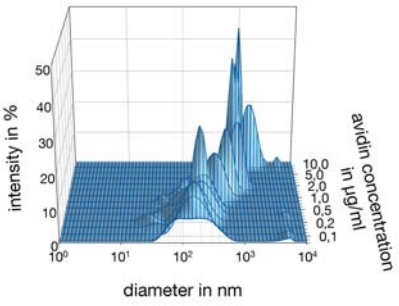

(a) Titration with FITC-avidin before the incubation on a magnet

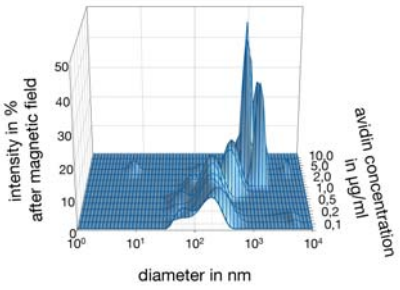

(b) Titration with FITC-avidin after the incubation on a magnet

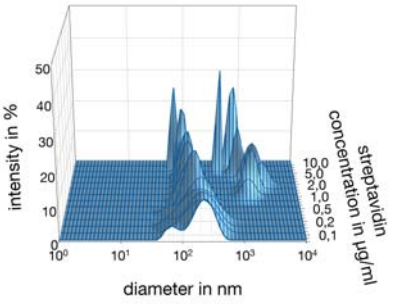

(c) Titration with streptavidin before the incubation on a magnet

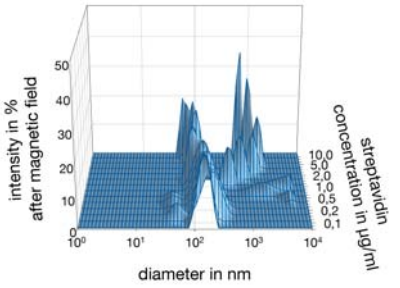

(d) Titration with streptavidin after the incubation on a magnet

Figure 4.18.: DLS measurements of the titration of FITC-avidin ((a) and (b)) and streptavidin ((c) and (d)) with anti-avidin MNPs; (a) and (c) are intensity weighted size distributions before the incubation on a NeFeB magnet at room temperaure for 1 h. (b) and (d) are the according size distributions after the incubation on a NeFeB magnet; concentrations of FITC-avidin and streptavidin are the same of the titration curves shown in Figure 4.17.

Long-term Measurements

The concentration of the targets leading to the most prominent change in T_2 relaxation time was chosen for long-term measurements of the T_2 relaxation time and of the cluster size using DLS measurements. In Figure 4.19 (a) the according intensity weighted size distribution is shown for one of the avidin long-term measurements. Figure 4.19 (b) shows the course of the T_2 relaxation time over 12 hours for the incubation of the anti-av MNP with FITC-avidin and streptavidin (both 40 μg/ml).

These long-term experiments measured in triplicate proof the results of the titration exper-

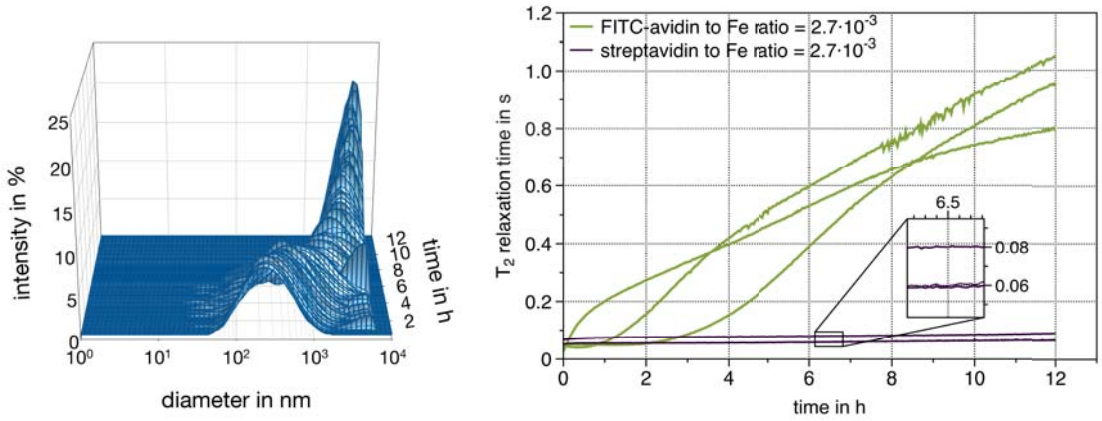

(a) Intensity weighted size distribution over 12 h

(b) T_2 relaxation time over 12 h

Figure 4.19.: Time course of the intensity weighted size distribution (a) and the T_2 relaxation time (b) for the long-term measurement of FITC-avidin and streptavidin with anti-avidin MNPs; For the dynamic light scattering measurement one example is shown for the T_2 relaxation time measurements three measurements for each set-up.

iments, since the T_2 relaxation time for streptavidin stays in a constant range whereas the T_2 relaxation time for FITC-avidin increases over time (Figure 4.19 (b)). The DLS measurements emphasise the increase of the cluster size over time (Figure 4.19 (a)) for the incubation of the anti-av MNP with FITC-avidin. Avidin is a tetramer made of four equal subunits. Therefore, four antibodies can bind to one avidin molecule and the particles can cluster due to the binding of avidin.

FITC-avidin Cluster Visualisation

Clusters of anti-av MNPs due to the incubation with FITC-avidin in a ratio of $2.7 \cdot 10^{-3}$ FITC-avidin to Fe were visualised using fluorescence microscopy (Figure 4.20 (a)) and TEM (Figure 4.20 (b)). The clusters can nicely be seen in the overlay of the bright field and the fluorescence microscope image. In fluorescence images with the lowest level of FITC-avidin no clustering could be seen. It is hard to distinguish clusters with MNPs and without in the TEM image due to the low concentration of MNP in the sample.

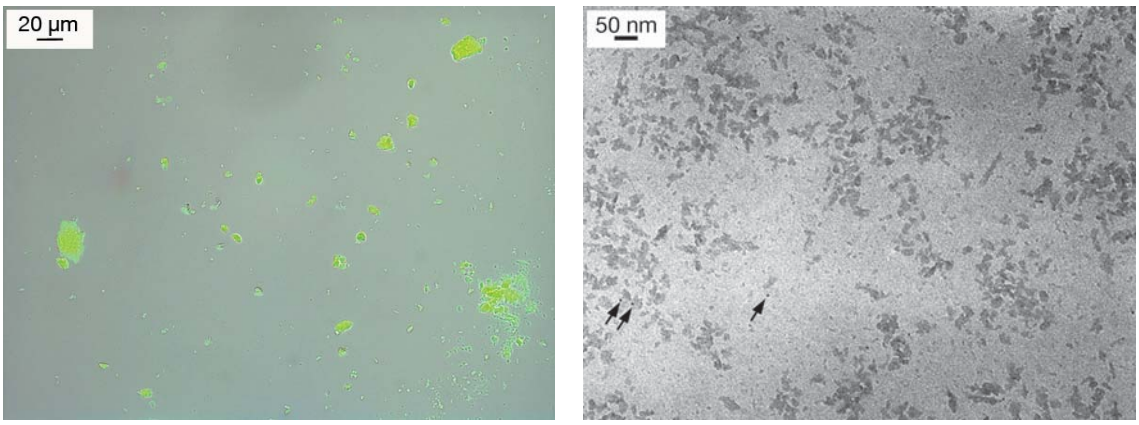

(a) Fluorescence microscope image (b) Transmission electron microscope image

Figure 4.20.: Fluorescence microscope and transmission electron microscope images of clusters of anti-avidin magnetic nanoparticles due to the incubation with FITC-avidin in a ratio of $2.7{\cdot}10^{-3}$. Overlay of bright field and FITC-fluorescence picture (a); transmission electron microscope image of the clusters (b); The arrows point to magnetic nanoparticles in the clusters.

4.3.2. *S. cerevisiae* Anti-*S. cerevisiae* MNP System

Titration

Anti-*S. c.* MNP were titrated with *S. cerevisiae* at a wide concentration range (factor of 10^8). The biggest differences that could be observed were in the higher cell to Fe concentration ratio range starting at a ratio of yeast cells to μmol Fe per ml of $4{\cdot}10^8$ (Figure 4.21). Here, an increase of the relaxation time compared to the relaxation time of the anti-*S. c.* MNP alone of more than 60% can clearly be seen. At the ratios lower than this the change in the T_2 relaxation time is less than 20%. These observations indicate that with this set-up $4{\cdot}10^8$ yeast cells in 1 ml can be detected with anti-*S. c.* MNP at a Fe concentration of 1 mM (= 1 μmol/ml). However, the measurements were conducted only once and a repetition is planned at higher concentrations.

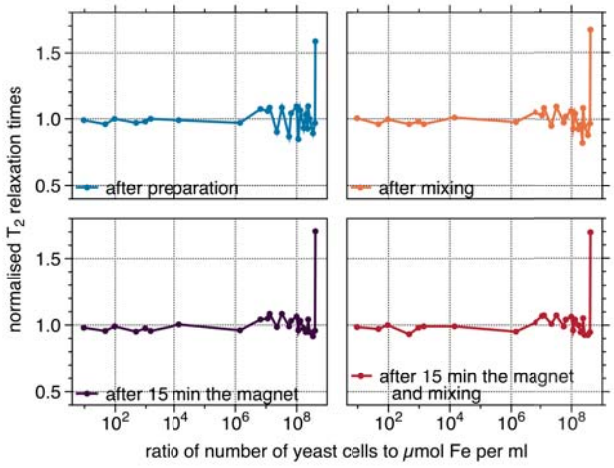

Figure 4.21.: Normalised T_2 relaxation times of the titration of yeast to anti-*S. cerevisiae* magnetic nanoparticles

Long-term Measurements

Long-term experiments were performed under the same conditions as for the incubation of anti-av MNPs with FITC-avidin and streptavidin (Section 4.3.1). For a better indication of a change in T_2 relaxation time due to the binding of anti-*S. c.* MNPs measurements were also performed of cells alone and anti-*S. c.* MNPs alone. There is no significant change of the slope of the T_2 relaxation time of *S. cerevisiae* incubated with anti-*S. c.* MNPs. The settling of the cells with the anti-*S. c.* MNP during the measurement can not be detected. However, this can be seen in the slope of the T_2 relaxation time of the *S. cerevisiae* cells alone. Thus, the long-term measurements show no hint of the binding of the anti-*S. c.* MNPs to the yeast cells.

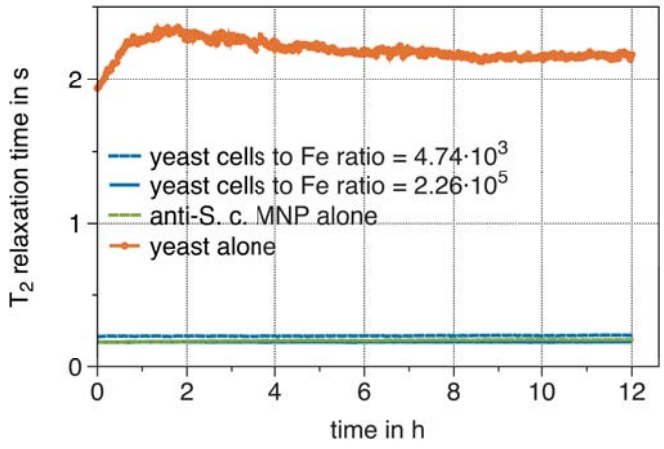

Figure 4.22.: Long-term measurements for 12 h of anti-*S.cerevisiae* magnetic nanoparticles incubated with yeast at different ratios, of anti-*S.cerevisiae* magnetic nanoparticles and of yeast alone

S. cerevisiae Cluster Visualisation

Due to its size of 2.5 μm - 5 μm yeast can be observed with a standard microscope using a 20x magnification. To visualise cluster formation between single yeast cells, samples were taken from long-term measurement of yeast cells incubated with anti-*S. c.* MNPs at a cell to Fe ratio of $2.3{\cdot}10^5$ (Figure 4.22) and of yeast cells without the incubation of magnetic nanoparticles (Figures 4.23 (a) and (b), respectively).
On comparison, both microscope images show clusters of *S. cerevisiae* cells. Some of the cell aggregates in Figure 4.23 (a) seem to be made of different layers compared to 4.23 (b), where they seem to be all in the same plane. This suggests tentatively that some cell aggregates could have been formed because of the incubation with anti-*S. c.* MNPs.

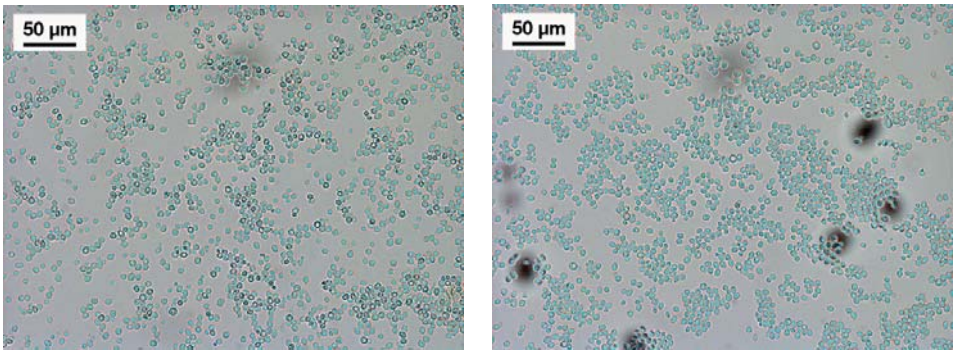

(a) With anti-*S. cerevisiae* magnetic nanoparticles

(b) Without anti-*S. cerevisiae* magnetic nanoparticles

Figure 4.23.: Microscope pictures of cells of *S. cerevisiae* with the incubation of anti-*S. cerevisiae* magnetic nanoparticles at a cell to Fe ratio of $2.3{\cdot}10^8$ (a) and without the incubation with anti-*S. cerevisiae* MNP (b)

Figure 4.24 shows the clustering of the *S. cerevisiae* cells due to the binding to anti-*S. c.* MNPs. This provides proof for the finding in the microscope images (Figure 4.23).

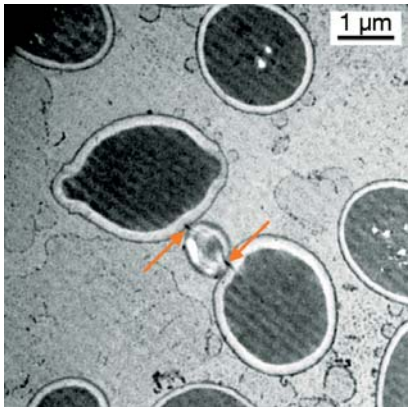

Figure 4.24.: Transmission microscope image of cells of *S. cerevisiae* with the incubation of anti-*S. cerevisiae* magnetic nanoparticles at a cell to Fe ratio of $2.3 \cdot 10^8$; Arrows indicate magnetic nanoparticles.

4.3.3. K562 Cells MNP System

Measurements with K562 cells and streptavidin MNP confirmed that cells incubated with nanoparticles lead to different T_2 relaxation times compared to particles, which were not incubated with cells (Table 4.4) [79]. The data is represented as mean ± standard deviation out of 5 measurements each done in 4 replicates (n = 20).

sample	T_2 in ms
streptavidin MNP in buffer	17.60 ± 0.81
K562 cells	435.83 ± 113.87
K562 loaded with streptavidin MNP	268.88 ± 18.53

Table 4.4.: T_2 relaxation times for streptavidin magnetic nanoparticles in buffer, K562 cells and K562 cells loaded with streptavidin magnetic nanoparticles (20 pg Fe/cell); Quantitative data is presented as mean ± standard deviation (n = 20).

K562 Cell Cluster Visualisation

TEM images were obtained to verify the origin of the change in the T_2 relaxation time due to the incubation of K562 cells with magnetic nanoparticles (Table 4.4). Figure 4.25 clearly shows that the particles are not internalised by the cells. The particles are on the outside of the cells and hold in place via microvilli. These microvilli are only at one pole of the cell and not evenly distributed around the cell. These experiments prove the change of the T_2 relaxation time due to the binding of MNP to the cells.

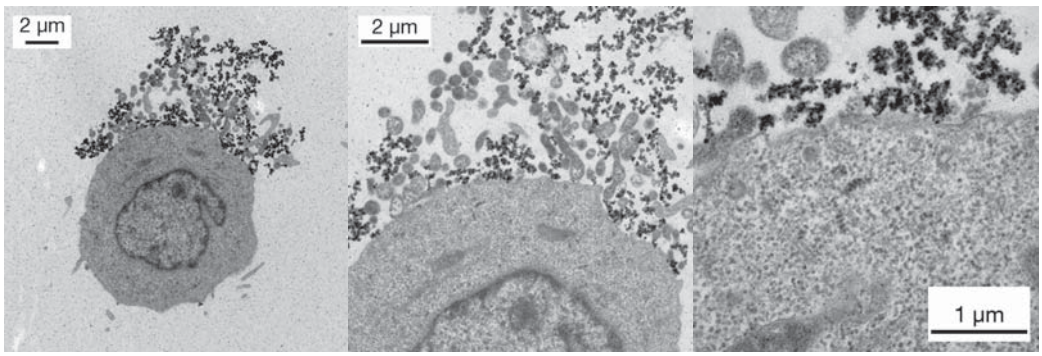

(a) 7,100x magnification (b) 16,500x magnification (c) 55,000x magnification

Figure 4.25.: Transmission electron microscope images of different magnifications of K562 cells loaded with streptavidin magnetic nanoparticles

4.3.4. Commercial Particles of Different Sizes

Figure 4.26 depicts the development of the T_2 relaxation time of MNPs with different sizes at the same iron concentration in a relaxometer of 21.7 MHz ($\approx$ 0.5 T). As the curves show, particles with a diameter of 100 nm aggregate in a static magnetic field over 1 h. Smaller magnetic nanoparticles (diameters $\leq$ 50 nm) give a constant signal over 1 h. For further use of MNP for relaxation measurements for the detection of targets the diameter of the particles should therefore be smaller than 50 nm.

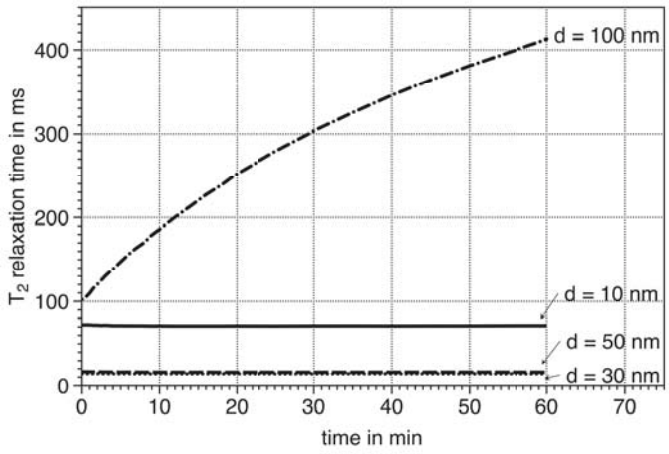

Figure 4.26.: Influence of a static homogeneous magnetic field of $\approx$ 0.5 T of a relaxometer at 21.7 MHz on the clustering of magnetic nanoparticles with different diameters observed by the change of the T_2 relaxation time. Particles with a hydrodynamic diameter of 100 nm tend to aggregate in the magnetic field leading to an increase in the T_2 relaxation time.

5. Discussion

5.1. Manufacturing of Magnetic Nanoparticles

The *suitable diameter of magnetic nanoparticles* for NMR T_2 relaxation time measurements was determined by measuring the T_2 relaxation time of commercial nanoparticles with different diameter at 21.7 MHz ($\approx$ 0.5 T) over one hour (Figure 4.26). Particles with a diameter of 100 nm showed an increase in their T_2 relaxation time, which was not caused by a clustering induced by binding partners. They solely agglomerated due to the magnetic field which causes them to align into energetically more favourable chains or circles [1]. Hence, a false positive result will be obtained in the detection measurements. Gravitational aspects have to be considered as well. The larger the particles are, the more they are not colloidal stable and they gravitate. This movement leads to a change in the T_2 relaxation time and gives false positive results as well. Particles with a diameter of 10 nm, 30 nm and 50 nm showed no increase of the relaxation time. A diameter of approximately 10 nm was chosen for the application of NMR T_2 relaxation measurements due to three reasons. First, to keep the attraction between the particles due to an applied magnetic field as low as possible. The agglomeration of MNPs due to a homogeneous field depends on their magnetic moments. Equation 2.8 shows that the magnetic moment of a MNP is proportional to its volume. Thus, by making the MNPs small their dipol moments are decreased. Second, if a thin coating is applied, the overall diameter of particles with a core size of 10 nm will not increase to a size where they are subjected to gravitational forces again. Third, if they are small, the clustering of the particles caused by the binding to the targets will also take longer, compared to larger particles which will be sooner influenced by the magnetic field upon clustering. Due to this fact, the manufactured particles were tailored to have a core diameter of approximately 10 nm.
For this purpose the particles were manufactured using the *co-precipitation method combined with the polyol method* with diethylene glycol as the polyol. Particles obtained by thermal decomposition methods have a better monodispersity and better crystal structures due to the higher temperatures applied and the homogeneous shapes, but have the severe drawback that only small amounts can be produced and the transformation from the organic media to aqueous solutions leads to a high loss of particles due to agglomeration. With the co-precipitation method combined with the polyol method the tailoring of the size worked well, the particles were colloidal stable and monodisperse and a fairly large amount was produced with one batch [3]. The size of the particles was controlled by a nucleation burst of a few seconds at high temperatures, to obtain many nucleation sites, which had the possibility to grow evenly to a size of about 10 nm over a time period of two

hours. The cooling time lead to some growth as well, but since the energy of the system was reduced, the rate of addition of precursors to the nuclei was also reduced [48]. The use of non-aqueous environments for the preparation of magnetite particles also prevented their oxidation to maghemite. Mössbauer spectra showed the presence of magnetite particles right after manufacturing in diethylene glycol (Figure 4.1 (a)). Diethylene glycol is a coordinating organic solvent and therefore prevents the oxidation of the magnetite particles to maghemite. Additionally, the use of diethylene glycol also inhibited the aggregation of the newly formed particles during manufacturing. It acted as a surfactant and bound to the surface of the particles building up a steric hindrance. Hence, the particles did not aggregate. During the peptising of the particles by washing them with 1 M HNO_3 to transfer them to aqueous media, this steric coating was exchanged for an electrostatic barrier, leaving a negative charge on the particle surface (Figure 4.9). Finally the high reaction temperature induced a good crystal growth, which was observed in the lattice structures in high resolution TEM images (Figures 4.3 (b), (c)).
A *coating* made of TEOS was chosen since it stabilises the particles against aggregation sterically and leaves hydroxy groups on the surface of the particles. Particles once coated with TEOS can be functionalised with different chemicals to leave different functional groups for various conjugation techniques [74]. APTES was chosen for the *functionalisation with amino groups* to keep the overall particle size very small, since the layer produced by this functionalisation will only be made the most of two layers of APTES. Since it is also a silane it will covalently bind to the already applied TEOS coating.
The antibodies were coupled to the MNP-APTES using *carbodiimid chemistry*, since the chemicals needed for this bioconjugation technique are not harmful. This chemistry could lead to the wrong orientation of the antibodies on the MNPs making them unable to bind to their target and their polymerisation can also occur. However, the chance of the polymerisation of the antibodies is very low, if a two step procedure, like the one in this thesis, is used and the amino groups, in this case the MNPs, are provided in excess. In contrast, for example, the method of reduction amination leads to the correct orientation of the antibodies on the MNPs, since the antibodies are bound to the MNPs via their sugar residues bringing them in the correct position on the particles for target binding. However, the chemical needed to reduce the Schiff base, sodium cyanoborohydride, is very toxic.

5.2. Characterisation of Manufactured Magnetic Nanoparticles

5.2.1. Core Characterisation

The iron oxide of the core of the manufactured MNPs was characterised by *Mössbauer spectroscopy*. Due to magnetic interactions, the hyperfine structure of the iron oxide is splitted, called Zeeman-splitting, and the spectrum of the sample shows a sextett structure (Figure 5.1) [2]. This splitting is proportional to the magnetic field close at the nuclei and is dependent on the temperature.

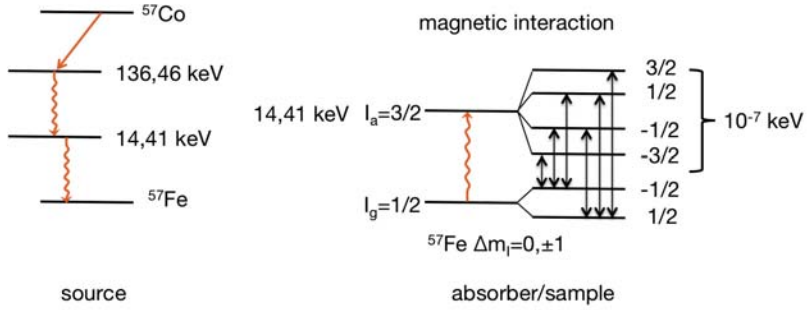

Figure 5.1.: Magnetic interactions leading to the evolution of the hyperfine structure in magnetic iron oxides

The fact that there are two different iron ions in the lattice leads to a shifting of two sextetts. This shift is called isomerism and originates from the iron (II) ions at the B-sites. The isomer shift is most prominent for the iron ions alone (Figure 5.2) but can be seen in the spectra of iron oxides containing iron (III) and iron (II) oxides as well (Figure 5.3).

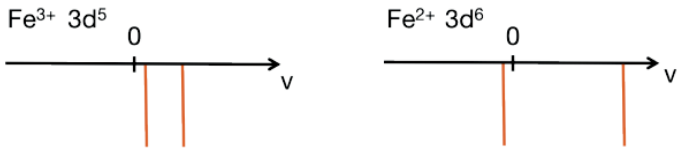

Figure 5.2.: Schematic Mössbauer spectra of iron (III) ions (left) and iron (II) ions (right)

Right after manufacturing the obtained spectrum was identical to magnetite. In magnetite, the iron ions are distributed over the A- and B- sites of the lattice in a specific way. Iron (III) ions can be found at the A-sites. Half of the B-sites are occupied by iron (III) ions and iron (II) ions leading to a free electron which can change its location between the different B-sites (Section 2.1.3). This leads to a reduction in the relative transmission of the B-sites in Mössbauer spectra (Figure 5.3).

During the oxidation of magnetite to maghemite this second sextett decreases and finally disappears, since iron (II) ions are oxidised to iron (III) ions. This fact was seen during the preparation of the particles. Right after production in diethylene glycol, the second sextett for magnetite was still seen very clearly (Figure 4.1 (a)). After the particles have been washed with 1 M HNO_3 to peptise them for the stable colloidal aqueous solution, only a hint of the second sextett was seen (Figure 4.1 (c)). After one week in this acidic environment, all the magnetite had been oxidised to maghemite (Figure 4.1 (e)).

The difference between the Mössbauer spectra taken at 4.2 K and at 298 K verified the superparamagnetic behaviour of the particles. Due to their small size, the splitting of the hyperfine structure into sextetts was not seen at 298 K (Figure 4.1 (c) and (d)). The time frame of Mössbauer spectroscopy is in the order of a few nanoseconds for ^{57}Fe spectra. Particles smaller than 10 nm have a much faster superparamagnetic relaxation time and therefore a Zeeman-splitting of the hyperfine structure can not be seen. This superparamagnetic

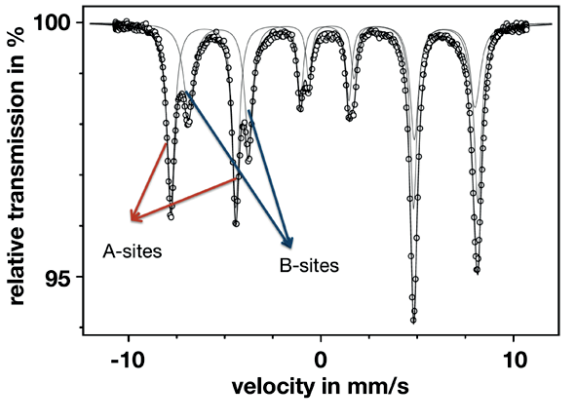

Figure 5.3.: Origin of the second sextett in Mössbauer spectra of magnetite; Iron (II) and iron (III) ions occupy the B-sites of the lattice each to one half. The free electron of the $3d^6$ orbital of the iron (III) ion is free to jump between the B-sites.

relaxation can be reduced by applying a static homogeneous magnetic field. Mössbauer experiments were carried out with the sample placed inside a static homogeneous magnetic field of about 0.75 T. According to M(H) measurements (Figure 4.11) approximately 90% of the manufactured MNPs have fully aligned magnetic moments. Thus the hyperfine structure can be detected at room temperature (Figure 4.1 (b)). The relative area of the sextetts is a lot smaller compared with the spectra at 4.2 K, since the particles are so small and not all of them are aligned in the magnetic field, thus, leading to a broadening of the spectrum [2].
The iron oxide nature of the manufactured particles was also shown by *electron diffraction pattern* and compared with electron diffraction patterns of the literature. Both showed the same pattern (Figures 4.2 (a) and (b)). The crystal lattice was seen in *TEM images* of high magnification and emphasises the importance of the high temperature during the preparation of the MNPs to obtain nice crystal structures (Figures 4.3 (b), (c)).

5.2.2. Size Determination of the Magnetic Nanoparticles

Determination of the Core Diameter

In this work, the size of the particles was determined by different techniques. It was determined using TEM images and DLS measurements. Additionally, it was calculated from the M(H) measurements of the particles as well as from NMR-D profiles. Table 5.1 sums up the results for the size of the core of the particles.

The sizes obtained by TEM and M(H) measurements are in good agreement with each other whereas DLS and NMR-D profiles both determined a larger diameter of the particles. Both TEM and M(H) regard the core size of the particles (Table 5.1).

method	diameter in nm
TEM	5.76 ± 1.69
DLS (number weighted)	9.73 ± 1.09
(DLS (intensity weighted)	14.02 ± 1.81)
M(H)	6.4 ± 0.3
NMR-D profile	10.1

Table 5.1.: Diameters of the core of the particles obtained by different methods

In *TEM image analysis*, the diameter of each single particle is measured and morphological information is provided at the same time with the size information. The disadvantage is the clustering of the particles which can occur during the sample preparation. To be able to obtain TEM images, the particles have to be dried on the grids since the TEM is performed in high vacuum. During this drying process the particles could aggregate and thereby cause artefacts. However, due to the low concentration needed and the surface charge of the particles, they were nicely dispersed on the grids. In *M(H) measurements*, only the core diameter is obtained by fitting a Langevin function to the obtained curve, since only the core of the particle contributes to the measured magnetisation (Figure 4.11). For the fitting of the data the saturation magnetisation has to be taken into account (Equation 2.8). For the naked particle this fitting is done including a measurement uncertainty of 10% due to the weighing uncertainty of the sample for M(H) measurements. This measurement uncertainty can account for the difference to the results for the size obtained by TEM image analysis. The possible agglomeration during sample preparation due to drying of the sample has to be kept in mind while analysing M(H) data.
Using *DLS measurements* the hydrodynamic diameter can be obtained very quickly in a few minutes. The measurements are done in the liquid environment of the samples and represent large ensembles of the particles and not just a few. However, the sizes obtained by DLS measurements are larger compared to the sizes obtained by TEM image analysis. There are various reasons for that. First, the solvent for the measurements has to be chosen correctly to circumvent possible hydratation artefacts and ion shells around the particle. Since the naked particles are strongly negatively charged (Figure 4.9), they are surrounded by a hydratation layer which is bound very tightly due to the charge. If the chosen solvent has an suboptimal pH or ionic strength the impact can be significant. Second, the concentration of the sample has a great influence on the results of the measurements as well. If the sample is too dense and, like MNPs, also coloured, this can lead to large artefacts in the measurements. Third, the refractive index of the sample has to be determined exactly for best measurement results. Fourth, in DLS measurements larger particles are always more prominent in their detection than smaller particles [124]. To reduce this artefact the diameter of number weighted size distributions is calculated from the intensity weighted size distributions taking this size shift into account. This can be seen in the difference between the intensity and the number weighted size distribution of the naked magnetic nanoparti-

cles (Table 5.1). These are in turn results from cumulant analysis of the autocorrelation function themselves. Therefore it is always important not only to rely on the mean values given by the DLS system, but to look at the observed size distributions. Hence, the obtained diameters by DLS measurements can be used as a hint for the real diameter, but most likely are larger compared to the true size obtained by TEM image analysis [124].
The diameter obtained by *NMR-D profiles* is the largest of the determined ones. This technique solely relies on fitting the data to theoretical models. It is suitable for diameters of less than approximately 20 nm and particles which are not agglomerating in a magnetic field [29]. However, these models underlie some assumptions. First, the exchange energy between the magnetic nanoparticles is larger than any other energy term. Second, the theory is based on an uniaxial system, where the Néel relaxation time is much shorter than the reorientation time of the particle in this system. This holds only true for perfect monodisperse particles with a diameter of less than approximately 20 nm. In contrast the manufactured naked MNPs are not perfectly monodisperse according to their PdI values of 0.23 explaining the larger calculated diameter of the particles. Third, it is assumed that all electronic spin levels have the same Nèel relaxation time, which is only partially true if all spin states have the same occupation probability. Therefore, NMR-D profiles can also give only a suggestion of the diameter of the particles, but must always be verified by other methods.

Size Determination of MNP-TEOS, MNP-APTES and anti-MNP

For the determination of the size of MNP-TEOS, MNP-APTES and anti-MNP DLS measurements were used, since the particles are kept in solution leading to a better result for their overall diameter than other methods like TEM image analysis. The diameters observed by number weighted size distributions were increasing with the coatings and functionalisations as expected. The intensity size distributions were different in their development. Here, the size of the MNP-APTES seemed to be smaller compared to MNP-TEOS (Figure 4.7 (a) and (b)).

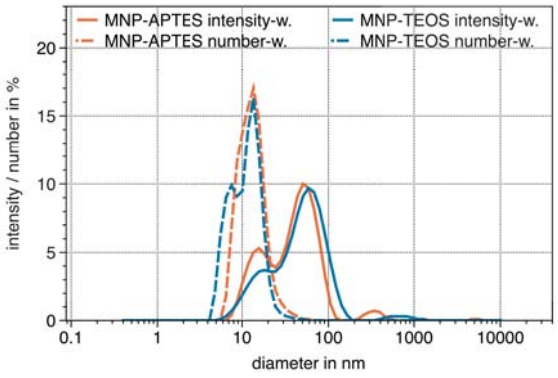

Figure 5.4.: Comparison of intensity and number weighted size distributions obtained by DLS measurements of MNP-TEOS and MNP-APTES; excerpt from Figure 4.7 (a) and (b)

The intensity weighted mean diameter for MNP-TEOS was higher (59.63 nm) than for MNP-APTES (39.14 nm), but the number weighted mean diameter was smaller (11.78 nm) than MNP-APTES (13.65 nm). This can be clearly seen in Figure 5.4. As mentionend before, diameters obtained by DLS measurements are larger, due to the intrinsic property of the method to emphasise bigger over smaller particles. Bigger particles scatter the light more than smaller ones and therefore the intensity of the scattered light is higher for larger particles than for smaller particles. To circumvent this problem the intensity weighted size distribution is calculated to a number weighted size distribution where this fact is taken into account. In Figure 5.4 three peaks can be seen meaning there are three populations and not one with this calculated mean diameter of 39.14 nm. After the intensity is taken into account, the mean diameter is reduced in the number weighted distribution to 13.65 nm. Here, only one peak is observed. However, the MNP-TEOS intensity weighted size distribution shows also three populations with a fraction of even bigger particles in the third population. These bigger size fractions are considered in the mean value of the intensity of 59.63 nm, but disappear in the number weighted distribution of 11.78 nm leading to differences between the mean diameters of intensity and number weighted size distributions. This concludes that the size distributions of DLS measurements should always be considered when using this method. Next to the distributions the PdI-values have to be considered as well. The mean PdI-values for all manufacturing stages are in the same range of 0.23-0.26. A value of zero indicates ideal monodispersity and values below 0.1 samples with a narrow monomodal size distribution [120]. The values above come close, but as can be seen in Figure 5.4 improvement can be done. This can be achieved by further centrifugation steps until the bigger particles are removed. To prevent aggregation during centrifugation the protocol for the additional centrifugation steps would have to adapted to this problem.

To determine the differences in diameters, DLS measurements can be considered relatively reliable. The particles are coated with a thin layer of approximately 2 nm thickness and their diameter is increased by 16.5 nm due to the antibody functionalisation. With the antibodies being approximately 7 nm long [121], this corresponds to a monolayer of antibodies of 8.25 nm thickness. For the applications in the NMR T_2 relaxation time measurements, a thin coating is preferable, for the outer sphere relaxation of the protons to be still applicable. If the coating was too thick the protons would not reach the induced magnetic field of the particles and therefore would not be influenced in their transverse relaxation. Thus, a thin coating improves the signal change in the NMR T_2 relaxation time detection measurements.

5.2.3. Surface Characterisation

FT-IR spectra and Zeta potential measurements showed a successful coating with TEOS and a successful functionalisation with APTES. In the FT-IR Spectra of MNP-TEOS and MNP-APTES transmission bands for TEOS and APTES, respectively, could be seen. The bending vibration of the C-H of the methylene bridge, which can be seen in naked MNPs as well as in the MNP-APTES, could be caused by the diethylene glycol, which has not been washed

off completely after manufacturing.
In the Zeta potential measurements, the point of zero charge (PZC) was shifted from pH 6.65 for naked MNPs to pH 2.85 for MNP-TEOS and then again to pH 5.29 for MNP-APTES. The PZC of the manufactured particles is in good agreement with the PZC for naked magnetite particles which is reported in the literature to be pH 6.8 [3]. The shift to a more acidic PZC for the MNP-TEOS is reasonable since this coating leaves oxide ions on the surface which form hydroxy groups in aqueous solutions. The hydroxy groups tend to be deprotonated, leading to a protonation state only in acidic environments. This leads to the loss of electrostatic repulsion forces since the negative surface charge becomes zero. Figure 4.9 also shows this negative Zeta potential for pH < 5. The amino group in APTES rather leads to a more neutral PZC. Amino groups are able to take up one proton leading to a shift of the pH to the alkaline range. Their pK_a value is usually in the range of 9.0 - 10.7 [74] therefore a PZC would be expected of a rather alkaline value than pH 5.29. The cause could be the amount of APTES taken up by the surface of the particles. It could be too few to raise the pH in such an alkaline condition, but enough to raise it to almost neutral pH. The functionalisation of APTES could therefore be improved, to obtain more amino groups on the surface. The amount of amino groups on the MNP surface could be determined using the ninhydrin assay. If the amount of amino groups already present could be increased, the amount of antibodies coupling to the MNPs could be improved.
The coating of the particles with silica, SiO_2, could not be verified in the TEM images obtained of MNP-TEOS and MNP-APTES (Figures 4.3 (b) and (c)). They revealed a lack of crystallinity in the surface modifications. This was also proven by obtaining dark-field TEM images and bright-field images. The differences between both types of images reveals other crystalline structures than the core of the particles, like, for example, a silica coating. In their overlay, only the iron oxide crystal could be observed but no boundary of crystalline SiO_2 was visible (Figure 4.4). This concludes that the condensation of the silanes was not completed during the coating process. The observed coating is made of silanes which are attached to the particle surface. They condensed to silica in some cases, but not enough to make up a nice crystalline SiO_2 coating of the particles. However, the functionalisation with APTES and the antibodies was still achieved since the binding to MNPs can also be achieved via bound silanes. To achieve further improvements of the particles, the coating procedure has to be adapted to this finding. Parameters to change can be the pH of the solution and/or the temperature. The condensation of silanes is favourable in alkaline conditions. The pH could be adjusted once the reactants have been mixed to prevent early aggregation of the particles. Comparable to the reversibility of the condensation of molecules under the release of water, the condensation with ethanol as the product is reversible as well. To change the equilibrium to favour the condensation process, the product (ethanol) has to be removed from the reaction system. This can be done by working at elevated temperatures (above the boiling point of ethanol, > 78 °C) and removing the evaporated ethanol from the reaction system. If the coating of the particles is refined one has to consider that the NMR T_2 relaxation time method to detect target relies on the outer sphere relaxation of protons. The sensitivity of the method is therefore improved if the coating is as thick as is has to be for the stabilisation but as thin as it can be for the protons to get as close to the

particle to be influenced by the induced magnetic field of the MNPs.

5.2.4. Magnetism and Relaxivity Determination

Magnetism

For a better comparison and discussion, the obtained saturation magnetisations of the M(H) measurements and the NMR-D profiles for the manufactured MNPs are listed in Table 5.2.

Sample	method	M_S (Am^2kg^{-1})	sample age	iron oxide
MNP naked	NMR-D	77.80	fresh	magnetite
MNP naked	M(H)	63.41	4 weeks	magnetite/maghemite
MNP naked	M(H)	41.77	2 months	maghemite
MNP-TEOS	M(H)	41.04	2 months	maghemite
MNP-TEOS	NMR-D	44.7	2 months	maghemite
MNP-APTES	M(H)	44.68	2 months	maghemite

Table 5.2.: Saturation magnetisation of manufactured particles obtained by M(H) and NMR-D measurements 4.11 and 4.13 reported with their age and iron oxide composition obtained by Mössbauer spectroscopy

The highest magnetisation can be observed for freshly prepared MNPs which are made of magnetite as determined by Mössbauer spectroscopy. The saturation magnetisation of bulk magnetite is 92-100 Am^2kg^{-1} [45] and for bulk maghemite 60-80 Am^2kg^{-1} [45]. Both saturation magnetisations are far higher than the magnetisations of the manufactured particles. However, it is known that the saturation magnetisation of nanoparticles is smaller compared to the bulk material. This is caused by the high surface to volume ratio of nanoparticles leaving the ions on the surface without any binding partners. This disrupts the crystal structure leading to a loss of the overall magnetisation [44]. The value of 78 Am^2kg^{-1} is higher than values given in the literature for magnetic nanoparticles which are in the range of 30-50 Am^2kg^{-1} [5]. 41-45 Am^2kg^{-1} given for two months old nanoparticles made of maghemite are in this range (Table 5.2). For a better saturation magnetisation of the coated and functionalised MNP the coating of the particles has to be applied right after peptising in 1M HNO_3. Thereby, the influence of the acidic environment and the ageing process which was observed in Mössbauer spectra can be reduced. Furthermore, the coating procedure should be improved, since the coating obtained was not made of pure silica as expected. If silica is obtained as coating it could be possible to stop the further oxidation process of the particles. Further experiments are necessary for verification keeping in mind the influence of the coating on the NMR T_2 relaxation time measurements.

NMR-D Profiles

The NMR-D profiles show the monodispersity of the naked particles. This is evident in the low field dispersion, which indicates a low anisotropy energy [3]. Since the anisotropy energy is proportional to the volume of the particle (Equation 2.3), a low anisotropy energy can also be compared to a small particle volume and therefore a small diameter. This observation at low magnetic fields is very sensitive as can be seen by comparing the naked MNP and MNP-TEOS NMR-D profile (Figure 4.13). The naked MNPs show a low field dispersion with a calculated diameter of 10.1 nm, whereas the MNP-TEOS do not show a low field dispersion, meaning a higher anisotropy energy, an a calculated diameter of 12.4 nm.

Magnetic Particle Spectroscopy

Magnetic particle spectroscopy was carried out of the manufactured particles and the spectra of a commercial particle suspension was also obtained for a better comparison with known particles. Figure 4.12 shows measurements of different fabrication batches of magnetic nanoparticles and of the contrast agent Resovist. Compared with Resovist, the amplitude of the measured k^{th} harmonic of the manufactured magnetic nanoparticles does not drop as fast, even though the particle sizes should be comparable. The contrast agent Resovist was chosen since the sizes of the particles should be in the same range according to the manufacturer. However, Eberbeck et al. showed that Resovist consists of two populations [125]. 70% are a very small population of 5 nm in diameter and 30% are a bigger population of 20-25 nm in diameter. This fact could explain the different observations in MPS measurements. To be able to compare both particle preparations, one would have to divide both populations of Resovist and measure both populations separately. A comparison of the manufactured magnetic nanoparticles with Resovist would then be more appropriate. The very small phases ($k < 10$) in the phase plot indicate that the magnetic field of the magnetic nanoparticles is able to relax without any energy loss and therefore without the development of heat. Furthermore, this indicates that the magnetic moment of the particles follows the magnetic field instantaneously, which in turn proofs their superparamagnetism. The naked particles have a similiar phase plot, whereas the different batches of coated particles show different curves (Figures 4.12 (a) and (b)). This could mean a yet not very reproducible coating. This property does not seem to influence the surface of the particles, since the Zeta potential and the stability remain equal between the batches. However, it influences their behaviour in the MPS measurements. This proofs again that the coating of the MNPs was not silica. The coating can rather be interpreted as a coating of silanes which are attached to the particles but are not fully condensed and therefore not fully covalently bound to each other. This aspect was also seen in the TEM images (Figures 4.3 (b) and (c)). Hence, the coating method works well, but for a better stability and reliability it still needs to be improved.

Relaxivity

The relaxivity of the manufactured particles increases with the diameter as can be seen in Table 4.3. Naked MNPs have a r_2 of 23 $mM^{-1}s^{-1}$ and MNP-APTES of 55 $mM^{-1}s^{-1}$. This is in accordance with the theory and as expected. Since r_2 stands for the relaxivity enhancement of 1 mM MNPs this means that the effects on the T_2 relaxation time increase with the increase of the coating. This is in agreement with the simulation of the outer sphere theory shown in Figure 2.13. The naked MNPs have a smaller size and therefore a higher T_2 relaxation time than the MNP-APTES. These particles are located in the motional averaging regime leading to a lower T_2 relaxation time. That means their enhancement is larger compared to naked MNPs. This can also be seen in the value for r_2. Contrast agents which are located in the averaging regime have relaxivities of 148 $mM^{-1}s^{-1}$ [91].

5.3. Relaxation Measurements

5.3.1. Antibody Characterisation

For the performance of the relaxation measurements, the antibody performance, in terms of the binding to its target, is of great importance. The SDS-PAGE of both antibodies shows proof that there was no contamination by other proteins which could bind to the MNP-APTES as well. This would have caused less antibodies to be bound to the MNP-APTES and therefore a worse detection of avidin and *S. cerevisiae*. The structure of an antibody is shown in Figure 5.5. The SDS-PAGE revealed only the heavy and light chain fragments of the antibodies or, as in the case of the anti-avidin antibody, a partial reduction of the disulfide bounds. This insufficient reduction during denaturation left some heavy and light chains still attached to each other and causes the weak bands above 49 kDa. There are even complete antibodies which can be seen in the pocket of the stacking gel in Figure 4.16.

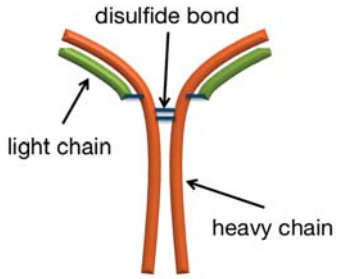

Figure 5.5.: Schematic drawing of an antibody with the heavy and light chains and the disulfide bonds which are reduced using Laemmli's method for denaturating SDS-PAGE

Dot Blot analysis was performed to investigate the affinity and specificity of the antibodies for their target. Both antibodies give a detection signal. However, the signal of the anti-avidin antibody is stronger than the signal for the anti-*S. cerevisiae* antibody (Figure 4.15).

The anti-avidin antibody shows already a good performance at a dilution of 1:2,000 in 0.28 ml/cm^2, whereas the anti-*S. cerevisiae* antibody shows hardly any signal at a dilution of 1:100 in 0.28 ml/cm^2. Furthermore, the specificity of the anti-avidin antibody was also proven for avidin and FITC-avidin but no cross-reactivity to streptavidin. The first two signals belong to the avidin and the FITC-labeled avidin. The area of the streptavidin yields no signal (circles in Figure 4.15 (a)). Thus, streptavidin can be used as negative control for the NMR relaxation measurements for the detection of avidin without a cross-reactivity of the anti-avidin antibody to streptavidin.

5.3.2. Avidin Detection

The detection of avidin was chosen as a proof-of-principle set-up to establish the particle functionalisation with antibodies and to set-up the method for the NMR T_2 relaxation time measurements. FITC-avidin was *titrated* at different concentrations to anti-av MNPs of one concentration and NMR T_2 relaxation time measurements were conducted (Figre 4.17 (c)). The first increase of 25% in the difference in the T_2 relaxation time of the preparation and of the incubation in the magnetic field of 15 min can be seen at a FITC-avidin concentration of 2 μg/ml or at a concentration ratio of FITC-avidin to Fe of $1.35 \cdot 10^{-10}$. This leads to a better concentration limit compared with particles from the literature, since half the concentration of the target can be detected. Compared with others, avidin has been detected using MNPs with a core diameter of 7 nm and a functionalisation with biotin at a magnetic field strength of 0.47 T [112]. The hydrodynamic diameter of the particles after functionalisation without bound biotin was 38 nm. At a Fe concentration of 0.2 mM, which is approximately the one used in this thesis, 70 μg/ml avidin were detected corresponding to a concentration ratio of avidin to Fe of $5.83 \cdot 10^{-9}$. This means the manufactured particles are able to detect half the concentration of avidin compared to the particles from the literature. This better performance could be due to the smaller coating layer of the particles leading to a better influence of the outer sphere relaxation on the protons of the water (Figures 2.14 and 2.13). It has to be mentioned that the measurement volume in the literature were 2 μl whereas in this thesis the volume was 200 μl. This is due to the different measurement set-ups. The smaller volume of the literature made a smaller construction of the spectrometer used for the NMR T_2 relaxation measurements possible. For better comparison the manufactured particles would have to be used in the spectrometer of the literature or the literature particles in the spectrometer used in this work.

The theory of the *outer sphere relaxation* can be seen in the NMR T_2 relaxation time measurements of the FITC-avidin titration to 0.22 mM Fe anti-av MNP as well (Figure 4.17 (a)). The core of the particles has a mean diameter of 5.76 nm obtained by TEM image analysis. This means that the particles are located in the motional averaging regime (Figure 2.13). Therefore upon the start of aggregation, the observed T_2 relaxation time first decreases to subsequently increase again, once the size of the clusters is located in the echo limiting regime. At a concentration ratio of FITC-avidin to anti-av MNP of $2.7 \cdot 10^{-9}$ compared to

the particles without their target, the T_2 relaxation time decreases right after the addition of the target to almost half of the initial value. That means as soon as the particles start to cluster the T_2 relaxation time first decreases. After an incubation period of 5 min in the static magnetic field of the relaxometer, the T_2 relaxation time started to increase. After an incubation time of 15 min in the magnetic field it increased to approximately the original value. The further increase in the T_2 relaxation time is shown in the *long-term measurement* in Figure 4.19 (b).
The *negative control* was conducted using streptavidin as the target. As has been shown by the Dot Blot analysis, the anti-avidin antibodies do not bind to streptavidin. This was also seen in the NMR T_2 relaxation time measurements where no change of the T_2 relaxation time could be seen (Figure 4.17 (b)). There seems to be a small change in the T_2 relaxation time at a molar concentration ratio between streptavidin and Fe of $1.5{\cdot}10^{-9}$. This is in fact caused by a longer incubation time on the bench of over three hours. This sample and the lower concentration samples where measured one after the other, but prepared at the same time to have the same conditions of ingredients in all samples. Each sample was measured after preparation and then each one after the other was incubated in the magnet of the spectrometer for 15 min and the T_2 relaxation time was measured. This lead to a longer overall incubation time for the later samples without purpose. These samples of this concentration range were repeatedly measured right after preparation and incubation in the magnetic field of 15 min and the higher T_2 relaxation time was not verified.
The measurements of the T_2 relaxation time were also accompanied by *DLS measurements* (Figure 4.18). The clustering of the anti-av MNP upon incubation with different concentrations of avidin can be seen as well as no clustering upon the incubation with streptavidin. Since these measurements could not be done while the sample was in a magnetic field, the samples were incubated on a NeFeB magnet at room temperature for one hour. The peaks of the intensity weighted size distributions are shifted to the larger sizes with increasing concentration of avidin. In contrast the peaks for the incubation with streptavidin stay in the same size range. For higher concentration ratios ($> 3{\cdot}10^{-10}$) of streptavidin, as well as avidin, some very sharp peaks are observed at larger diameters. They are more prominent for the avidin measurements after the incubation on the NeFeB magnet. These peaks are due to measurement artefacts caused by the high protein concentrations in the samples (asterisks in Figure 5.6). Such a high concentration of protein leads to light scattering artefacts exceeding the optimal operating conditions for the instrument.

The cluster formation was also visualised using *fluorescence microscopy and TEM*. The clusters of the anti-av MNP with FITC-avidin incubation are shown in the fluorescent image (Figure 4.20 (a)). The imaging of the clusters using TEM reveals hardly any particles which makes it hard to observe a cluster formation. The reason for this could be that the grid used for TEM images is too thin for the preparation of magnetic nanoparticle clusters and broke during preparation. After drying of the MNP clusters and transferring the grid to the TEM most of the thin carbon layers in the grid were already broken or breaking as soon as the electron beam hit them. The few stable regions were loaded with very few particles. Taken together, the particle clusters were too heavy for the grid to remain stable during the

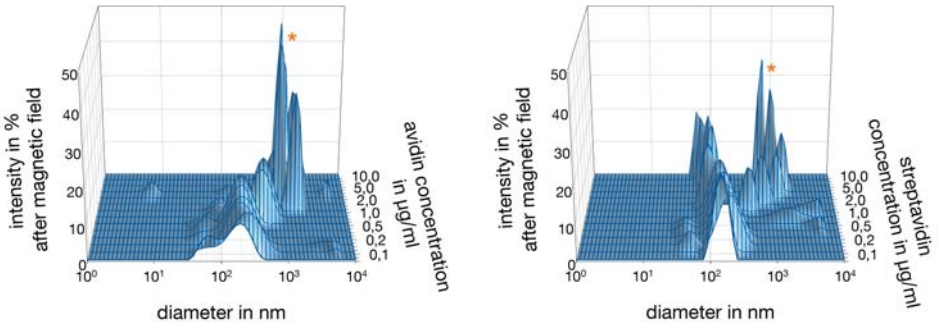

(a) Titration with FITC-avidin after the incubation on a magnet

(b) Titration with streptavidin after the incubation on a magnet

Figure 5.6.: DLS measurements of the titration of FITC-avidin (a) and streptavidin (b) with anti-avidin MNPs; shown are intensity weighted size distributions after the incubation on a NeFeB magnet at room temperature for one hour; concentrations of FITC-avidin and streptavidin are the same of the titration curves shown in Figure 4.17. The asterisks indicate artefact peaks due to high protein concentrations in the samples.

drying conditions or under the electron beam.
To sum up, the results of the anti-av MNP FITC-avidin system are in good agreement with the literature and the set-up used (spectrometer and MNPs) has an even better detection limit by a factor of two.

5.3.3. Detection of *Saccharomyces cerevisiae*

For the detection of *S. cerevisiae* it is important that the change of the T_2 relaxtion time is also induced if *MNPs bind on the outside of cells*. To proof this, NMR T_2 relaxation time measurements with K562 cells were conducted, which were incubated with commercial MNPs (d = 100 nm). These measurements showed a change in the T_2 relaxation time of over 15 times the initial value for the MNPs alone [79]. The origin of the change in the T_2 relaxation time was caused by the binding of the MNPs to the cells as revealed by TEM images (Figure 4.25). Therefore a specific binding of MNPs to a cell via antibodies against a surface protein of the cell should lead to a change in the T_2 relaxation time as well.

Like the *tritration* of FITC-avidin and streptavidin to anti-av MNPs, *S. cerevisiae* was titrated to anti-*S. c.* MNPs. An increase of 1.5 times was seen at a concentration ratio of *S. cerevisiae* to Fe of $4{\cdot}10^8$, meaning that $4{\cdot}10^8$ cells of *S. cerevisiae* were detected with anti-*S. c.* MNPs of a concentration of 1 mM Fe. The titration curve for the detection of *S. cerevisiae* has to be extended to a higher concentration range of yeast of more than 10^8 cells/ml. The results from 10^8 cells/ml should have to be included for better comparison of the already obtained data. The *long-term measurements* of *S. cerevisiae* with anti-*S. c.* MNPs showed no detection over the time (Figure 4.22). Suggesting there is not enough binding to the

cells. To proof the binding *microscope images* were obtained that gave hints of a binding of the yeast cells due to the binding of the anti-*S. c.* MNPs and subsequent clustering (Figures 4.23 (a) and (b)). This finding was verified by TEM images where a clustering of the yeast cells due to anti-*S.c.* MNPs could be seen (Figure 4.24). There is obviously binding of the manufactured MNPs to the cells, but it was in this particular case not enough for a change in the T_2 relaxation time.
In the literature similar organisms and cells have been detected using NMR T_2 relaxation time measurements. *Staphylococcus aureus* has been detected using the same method at a concentration as low as $5{\cdot}10^3$ bacteria/ml [112]. The MNP used were functionalised with vancomycin and had a core diameter of 7 nm and a hydrodynamic diameter with the coatings of 38 nm. This detection limit is a magnitude of 10^5 lower compared to the detection limit of *S. cerevisiae* cells. There are several reasons for this. One reason is the different size of the target organism. The yeast cells are between 2.5-5 μm in diameter, whereas the bacteria are about 1 μm in size. Using the same system, mouse macrophages were detected at a concentration of 100 cells/ml [109]. This leads rather to the assumption that the size of the target is not a reason for the low detection limit. Another reason could be the low binding performance of the antibody. The Dot Blot analysis showed a binding to the yeast cell lysate, but this was very low compared to the performance of the anti-avidin antibody. This caused some MNP to be in-effective in binding and lead to a worse target to MNP ratio, since more anti-*S. c.* MNPs have to be used for the detection of *S. cerevisiae*. Koh et al. showed that targets of large sizes with many valencies for the binding of a possible target show better detection thresholds if they are detected with MNPs of μm size range [103]. They compared MNPs with a diameter of 70 nm and MNPs with a diameter of 1 μm for their detection performance of targets of different sizes (8 nm and 900 nm) and with different valencies. It is hard to compare their findings with the yeast target of 2.5 μm size and a MNP with a hydrodynamic diameter of 30 nm. However, they conclude that the larger target of 900 nm diameter is detected at a better threshold using the larger particles of 1 μm in diameter. By using a 10 times larger MNP they decreased their detection limit of a large target by a factor of 10^{-6}. This approach could lead to a decrease of the detection limit to 10^2cells/ml. This suggests a bigger core and therefore a bigger hydrodynamic radius and a greater magnetic moment would have to be used for a better detection of *S. cerevisiae*. Most probably the low binding efficiency of the anti-*S. cerevisiae* antibodies could be compensated by the use of larger MNPs, since the signal change due to the outer sphere relaxation in the echo limiting regime would be more effective (Figure 2.13).

By the use of an antibody with a better binding efficiency, the MNP would obtain more effective binding sites and the probability of fully functional anti-*S. c.* MNPs would be higher. Whether the functionalisation with better performing antibodies could decrease the detection limit further from the proposed 10^2cells/ml with larger particles to 1 cell/ml is questionable. The larger particles would also lead to a larger surface with a higher density of antibodies per MNP. Therefore, it could be reasonable to say, that a better binding affinity of the antibody to its target could lead to such an decrease. But this needs to be verified. Further experiments would include NMR relaxation measurements with the manufactured particles and the better antibody and by the manufacturing of MNP with a larger core size, its functionalisation with the low performance antibody and subsequent measurements.

6. Conclusion

In this thesis, small magnetic nanoparticles were manufactured and fully characterised for their size, their core material, their magnetisation and surface. They were functionalised with antibodies for the detection of specific bindings based on the change in T_2 relaxation time. This method was applied for the detection of avidin and *Saccharomyces cerevisae*, the later one being of importance for the quality control in the production of alcohol-free beverages.

The theory for the physical and chemical properties of magnetic nanoparticles was described together with the theory of their manufacturing, the chemistry of iron oxides, as well as the coating and functionalisation procedures of magnetic nanoparticles. The magnetic nanoparticles were reproducibly manufactured by the co-precipitation method combined with the polyol method, coated with tetraethoxysilane and functionalised with (3-Aminopropyl)triethoxysilane. They were further functionalised with antibodies using carbodiimide chemistry. The obtained nanoparticles were morphologically characterised, for their surface and for their magnetic properties. For the characterisation various methods were used and compared. The core of the manufactured nanoparticles had the desired diameter of 5.76 ± 1.69 nm as determined by transmission electron microscopy image analysis. Dynamic light scattering revealed a higher hydrodynamic diameter caused by intrinsic properties of the method which is still a good approximation of the diameter obtained by transmission electron microscopy image analysis. This size difference is due to the intrinsic properties of the dynamic light scattering. Both methods have their drawbacks and should be used in tandem for reliable results.

The iron core of the magnetic nanoparticles was characterised with Mössbauer spectroscopy. The particles manufactured were made of magnetite which was oxidised to maghemite despite of the applied coating. The oxidation was seen during an observation period of two months.

The magnetisation had a similiar development. Freshly prepared particles had a saturation magnetisation of 78 Am^2kg^{-1} which is about twice as much as values found in the literature. The inevitable oxidation process of particles of this size lead to a saturation magnetisation of 41 Am^2kg^{-1} which is in accordance with the literature. The magnetisation values affirmed the oxidation of magnetite to maghemite during the preparation of the magnetic nanoparticles as has been seen by Mössbauer spectroscopy.

The magnetic nanoparticles needed a thin coating to be colloidal stable and thus to be appropriate for nuclear magnetic resonance T_2 relaxation time measurements. The coating applied in this thesis was of 1.96 nm thickness as determined by dynamic light scattering measurements and lead to a final hydrodynamic diameter of the magnetic nanoparticles of 13.65 ± 3.64 nm. The increase of the diameter of the magnetic nanoparticles was deter-

mined by dynamic light scattering, since the particles stayed in suspensions for the measurements and aggregation can hardly occur. The thickness of the coating was as thin as needed for a good sensitivity in nuclear magnetic resonance T_2 relaxation time measurements. However, it was made of silanes rather than of silica. The particles are surrounded by a loose structure of silanes, but are colloidal stable for six months. Due to the not fully condensed silanes there seems to be a lack of reproducibility in the intrinsic properties of the magnetic nanoparticles. This was only seen in magnetic particle spectroscopy measurements.

The further functionalisation of (3-Aminopropyl)triethoxysilane coated magnetic nanoparticles was conducted by carbodiimide chemistry. Good and reproducible functionalisations with antibodies were created despite the fact that the coating was not made of silica. The antibodies were applied as a monolayer around the particles, which was determined by the hydrodynamic radius increase of 8.25 nm and antibodies having a size of about 7 nm. The method is fast, reliable and no harmful chemicals are necessary.

The first system to verify the preparation protocol of the magnetic nanoparticles and the detection method was the avidin system. FITC-avidin was detected at a concentration of 1.35 fM FITC-avidin with anti-avidin magnetic nanoparticles of 1 mM Fe iron content using a spectrometer with 21.7 MHz ($\approx$ 0.5 T). This detection level was twice as good as the detection levels for avidin found in the literature. This indicates a better performance of the established set-up compared to the literature. However, the amount of bound anti-avidin antibody to the magnetic nanoparticles needs to be determined for a better comparison with the literature.

The second system was the application of the nuclear magnetic resonance T_2 relaxation time measurements for the detection of *S. cerevisiae*. Here a detection limit of $4{\cdot}10^8$ cells/ml were detected using anti-*S. cerevisiae* magnetic nanoparticles. The successful binding of the magnetic nanoparticles to the yeast cells was observed by bright field and transmission electron microscopy. However, the titration experiments need to be verified. The detection limit is too high for the application in the quality control of the beverage industry and needs improvement to be able to detect one yeast cell per ml. This may be achieved by using antibodies with a better binding affinity, comparable to the anti-avidin antibodies used for the FITC-avidin detection, and/or by preparing particles with a larger core size and therefore a larger magnetic moment leading for this particular target to a better sensitivity in the nuclear magnetic resonance T_2 relaxation time measurements. A larger core size can be achieved by a longer incubation at high temperatures during the preparation, or by increasing the intial amount of iron salts and NaOH pellets added to the reaction system.

A. Abbreviations

anti-Av MNP	anti-avidin antibody magnetic nanoparticle
anti-*S. c.* MNP	anti-*Saccharomyces cerevisiae* antibody magnetic nanoparticle
APTES	(3-Aminopropyl)triethoxysilane
BSA	bovine serum albumin
DLVO theory	Derjaguin-Landau-Verwey-Overbeek theory
DMEM	Dulbecco's modified Eagle medium
DMR	diagnostic magnetic resonance
DMSO	dimethylsulfoxide
DTT	dithiothreitol
EDC	N-(3-Dimethyl- aminopropyl)-N′-ethylcarbodiimide hydrochloride
ELISA	enzyme linked immunosorbent assays
FITC	fluorescein isothiocyanate
FTIR	fourier transformed infrared spectroscopy
IgG	immunglobulin G
MNP	magnetic nanoparticle
MRI	magnetic resonance imaging
NHS	N-Hydroxysuccinimide
NMR	nuclear magnetic resonance
PBS	phosphate buffered saline
PEG	poly-ethylene-glycol
PMSF	phenylmethylsulfonyl fluoride
RIPA	radioimmunoprecipitation assay
RT-PCR	reverse transcriptase polymerase chain reaction
SDS-PAGE	sodium dodecyl sulfate poly-acryl gel electrophoresis
TEM	transmission electron microscopy
TEOS	tetraethoxysilane

B. Material and Equipment

B.1. Chemicals

The following chemicals were used without further purification:

Application	Chemical	Manufacturer
All	doubled deionised water	Siemens Ultra Clear Millipore system
All	Tris Base	Roth
All	Tween 20	Merck
Dot Blot Analysis	Clarity Western ECL Substrate	BIO-RAD
Dot Blot Analysis	nitrocellulose membrane	GE Healthcare
Dot Blot Analysis	Tris-HCl	Roth
Dot Blot Analysis	phenylmethylsulfonyl fluoride (PMSF)	Applichem GmbH
Dot Blot Analysis	skim milk powder	Applichem GmbH
Dot Blot Analysis	SuperSignal West PICO Complete Rabbit IgG Detection Kit	Pierce
FTIR Spectroscopy	KBr	Roth
Iron Content	37% hydrochloric acid	Merck
Iron content	$FeCl_3 \cdot (H_2O)_6$	Merck
Mössbauer Spectroscopy	two component glue plus endfest	UHU
MNP Synthesis	(3-Aminopropyl)-triethoxysilane (APTES)	Sigma-Aldrich
MNP Synthesis	45% $FeCl_3 \cdot (H_2O)_6$ solution	Riedel-deHaen

Continued on next page

– Continued from previous page

Application	Chemical	Manufacturer
MNP Synthesis	anti-*Saccharomyces cerevisiae* antibody	Antibodies online
MNP Synthesis	anti-avidin antibody	Antibodies online
MNP Synthesis	bovine serum albumine (BSA)	BioZym
MNP Synthesis	diethylene glycol	Roth
MNP Synthesis	$FeCl_2 \cdot (H_2O)_4$	Merck
MNP Synthesis	N-(3-dimethyl-aminopropyl)-N′-ethylcarbodiimide hydrochloride (EDC)	Sigma-Aldrich
MNP Synthesis	N-Hydroxysuccinimide (NHS)	Sigma-Aldrich
MNP Synthesis	$Na_2B_4O_7 \cdot (H_2O)_{10}$	Merck
MNP Synthesis	NaOH pellets	Merck
MNP Synthesis	tetraethoxysilane (TEOS)	Sigma-Aldrich
Relaxation Measurements	FluidMag-D (50 nm) and FluidMag-Streptavidin (100 nm)	Chemicell GmbH
Relaxation Measurements	fluorescein isothiocyanate (FITC) -avidin	invitrogen molecular probes
Relaxation Measurements	SHP-10 (10 nm) and SHP-30 (30 nm)	Ocean Nanotech
Relaxation Measurements	SiMag-Streptavidin	Chemicell GmbH
Relaxation Measurements	streptavidin ultra pure	Applichem GmbH
SDS-PAGE	Coomassie Blue staining solution	BIO-RAD
SDS-PAGE	dithiothreitol (DTT)	Applichem GmbH
SDS-PAGE	methanol	Roth
SDS-Page	SM0441 prestained protein molecular weight marker	Fermentas
SDS-PAGE	taurine	Applichem GmbH
SDS-PAGE	sodium dodecyl sulfat (SDS)	Sigma-Aldrich

Continued on next page

– Continued from previous page

Application	Chemical	Manufacturer
SDS-PAGE	98% glycerol	Roth
SDS-PAGE	bromphenolblue	Sigma-Aldrich
SDS-PAGE	30 % acrylamide	Applichem GmbH
SDS-PAGE	N,N,N′,N′-tetramethylethylenediamine (TEMED)	Applichem GmbH
SDS-PAGE	ammonium persulfate (APS)	Applichem GmbH
Zeta Potential	69% salpetric acid	Applichem GmbH

B.2. Buffers

Application	Buffer	Recipe
Dot Blot Analysis	10x TBS	5 M NaCl, 35 mM Tris Base, 165 mM Tris-HCl, pH 7.5
Dot Blot Analysis	RIPA-buffer	BIO-RAD
Dot Blot Analysis	TBS-T	1 x TBS,1% Tween-20
MNP Synthesis	50 mM sodium borate buffer	50 mM boric acid, 50 mM sodium tetraborate, pH 8.17
MNP Synthesis	blocking buffer	10 mM Na_2HPO_4, 1 % BSA, pH 7.4
SDS-PAGE	6x stacking gel buffer	1.35 g Tris Base, 9 ml 1 M HCl, pH 7.5
SDS-PAGE	2x sample buffer	2 ml 6x stacking gel buffer, 4 % SDS, 100 mM DTT, 30% glycerol, bromphenolblue
SDS-PAGE	running buffer	6.005 g Tris Base, 24.43 g taurine, 1 g SDS
SDS-PAGE	destaining solution	67.5 % H_2O_{dd}, 7.5 % acetic acid, 25 % methanol

B.3. Cell Culture Material

Material	Manufacturer
Dulbecco's Modified Eagle Medium (DMEM)	Biochrom AG
fetal calf serum	Biochrom AG
penicillin-streptomycin	Biochrom AG

B.4. Equipment

Application	Equipment	Manufacturer
Cell Culture	Axiovert 200	Carl Zeiss Jena GmbH
DLS	Zetasizer Nanoseries Nano-ZS90	Malvern Instruments
Dot Blot Analysis	Fluor-S MultiImager	BIO-RAD
Dot Blot Analysis	CCD camera Quantix	Roper Scientific Inc.
Fluorescence Imaging	Axioskop 2 MAT mot	Carl Zeiss Jena GmbH
FTIR Spectroscopy	isostatic dry press	P.O.Weber
FTIR Spectroscopy	model 8, size II, 13 mm KBr pellet die	P.O.Weber
FTIR Spectroscopy	Spectrum One	Perkin Elmer
Iron Content	Fe Spectroquant kit	Merck
M(H) Measurements	Fixogum	Marabu
M(H) Measurements	MPMS XL	Quantum Design
Mössbauer Spectroscopy	Alpha 1-2 LO	Christ
MNP Synthesis	2 L AutLab Flex Reactor	HEL Ltd.
MNP Synthesis	Amicon 8200 cell	Millipore
MNP Synthesis	Optima LE-70 ultracentrifuge with rotor SW28	Beckman Coulter
MNP Synthesis	Ultrafiltration disc Biomax 300 kDa	Millipore

Continued on next page

– Continued from previous page

Application	**Buffer**	**Recipe**
MNP Synthesis	Ultrafiltration disc Ultracell 30 kDa	Millipore
NMR-D Profile	Spinmaster FFC-2000	Stelar s.r.I.
Relaxation Measurements	mini-spec systems mq20 and mq60	Bruker
Relaxation Measurements	NMR Spectrometer Avance 250	Bruker
Relaxation Measurements	Research Lab	pure devices
TEM	300 mesh grid coated with carbon	Quantifoil
TEM	300 mesh grid coated with holey carbon film	Quantifoil
TEM	JEM100 CX	Jeol
Ultrasound Treatment	Sonoplus HD 2200	Bandelin
Ultrasound Treatment	UW 2200	Bandelin
Zeta Potential	high concentration Dip cell	Malvern Instruments

List of Figures

List of Tables

Bibliography

[1] R.E. Rosensweig. *Ferrohydrodynamics*. Dover Publications, Inc., Mineola, New York, Jul 1997.

[2] S. Mørup, M.F. Hansen, and C. Frandsen. Magnetic Nanoparticles. In D. L. Editors-in Chief: Andrews, G. D. Scholes, , and G. P. Wiederrecht, editors, *Comprehensive Nanoscience and Technology*, pages 437 – 491. Academic Press, Amsterdam, 2011.

[3] S. Laurent, D. Forge, M. Port, A. Roch, C. Robic, L. Vander Elst, and R. N. Muller. Magnetic iron oxide nanoparticles: synthesis, stabilization, vectorization, physicochemical characterizations, and biological applications. *Chem Rev*, 108(6):2064–2110, Jun 2008.

[4] R. Qiao, C. Yang, and M. Gao. Superparamagnetic iron oxide nanoparticles: from preparations to in vivo MRI applications. *J. Mater. Chem.*, 19:6274–6293, 2009.

[5] A. K. Gupta and M. Gupta. Synthesis and surface engineering of iron oxide nanoparticles for biomedical applications. *Biomaterials*, 26:3995–4021, Jun 2005.

[6] J. Lodhia, G. Mandarano, Nj Ferris, P. Eu, and S. Cowell. Development and use of iron oxide nanoparticles (Part 1): Synthesis of iron oxide nanoparticles for MRI. *Biomed Imaging Interv J*, 6:e12, Apr 2010.

[7] C. Corot, P. Robert, J. M. Idée, and M. Port. Recent advances in iron oxide nanocrystal technology for medical imaging. *Adv Drug Deliv Rev*, 58:1471–1504, Dec 2006.

[8] Q. A. Pankhurst, J. Connolly, S. K. Jones, and J. Dobson. Applications of magnetic nanoparticles in biomedicine. *Journal of Physics D: Applied Physics*, 36(13):167, 2003.

[9] R. Stephen Zachary, M. Kievit Forrest, and M. Zhang. Magnetite nanoparticles for medical MR imaging. *Materials Today*, 14:330–338, 2011.

[10] A. Stroh, C. Faber, T. Neuberger, P. Lorenz, K. Sieland, P. M. Jakob, A. Webb, H. Pilgrimm, R. Schober, E. E. Pohl, and C. Zimmer. In vivo detection limits of magnetically labeled embryonic stem cells in the rat brain using high-field (17.6 T) magnetic resonance imaging. *Neuroimage*, 24:635–645, Feb 2005.

[11] J. K. Kirsch. Basic principles of magnetic resonance contrast agents. *Topics in Magnetic Resonance Imaging*, 3:1, Mar 1991.

[12] B. Gleich and J. Weizenecker. Tomographic imaging using the nonlinear response of magnetic particles. *Nature*, 435:1214–1217, 2005.

[13] J. Weizenecker, Joern Borgert, and Bernhard Gleich. A simulation study on the resolution and sensitivity of magnetic particle imaging. *Phys Med Biol*, 52:6363–6374, 2007.

[14] R.M. Ferguson, K. R. Minard, and K. M. Krishnan. Optimization of nanoparticle core size for magnetic particle imaging. *Journal of Magnetism and Magnetic Materials*, 321(10):1548–1551, 2009.

[15] A. Pankhurst Q., T. Thanh N. K., K. Jones S., and J. Dobson. TOPICAL REVIEW: Progress in applications of magnetic nanoparticles in biomedicine. *Journal of Physics D*, 42:4001, Nov 2009.

[16] G. Baronzio, A. Gramaglia, and G. Fiorentini. Current Role and Future Perspectives of Hyperthermia for Prostate Cancer Treatment. *In Vivo*, 23(1):143–146, 2009.

[17] C. Alexiou, R. Tietze, E. Schreiber, R. Jurgons, H. Richter, L. Trahms, H. Rahn, S. Odenbach, and S. Lyer. Cancer therapy with drug loaded magnetic nanoparticles - magnetic drug targeting. *Journal of Magnetism and Magnetic Materials*, 323:1404–1407, May 2011.

[18] S. C. McBain, H. H. Yiu, and J. Dobson. Magnetic nanoparticles for gene and drug delivery. *Int J Nanomedicine*, 3:169–180, Jan 2008.

[19] W. H. De Jong and P. J. Borm. Drug delivery and nanoparticles: applications and hazards. *international journal of nanomedicine*, 3:133–149, Jun 2008.

[20] J. Chomoucka, J. Drbohlavova, D. Huska, V. Adam, R. Kizek, and J. Hubalek. Magnetic nanoparticles and targeted drug delivering. *Pharmacol Res*, 62(2):144–149, Aug 2010.

[21] M. Anton, A. Wolf, O. Mykhaylyk, C. Koch, B. Gansbacher, and C. Plank. Optimizing Adenoviral Transduction of Endothelial Cells under Flow Conditions. *Pharmaceutical Research*, Jan 2011.

[22] B. Gleich, T. Weyh, and B. Wolf. Magnetic Drug Targeting: an analytical model for the influence of blood properties on particle trajectories. *Applied Rheology*, 18:52023, May 2008.

[23] A. Heidsieck, S. Vosen, K. Zimmermann, D. Wenzel, and B. Gleich. Analysis of Trajectories for Targeting of Magnetic Nanoparticles in Blood Vessels. *Mol Pharm*, Jun 2012.

[24] C. Kilgus, A. Heidsieck, A. Ottersbach, W. Roell, C. Trueck, B. K. Fleischmann, B. Gleich, and P. Sasse. Local Gene Targeting and Cell Positioning Using Magnetic Nanoparticles and Magnetic Tips: Comparison of Mathematical Simulations with Experiments. *Pharmaceutical Research*, Jan 2011.

[25] G. Fonnum, C. Johansson, A. Molteberg, S. Mørup, and E. Aksnes. Characterisation of Dynabeads by magnetization measurements and Mössbauer spectroscopy. *Journal of Magnetism and Magnetic Materials*, 293(1):41 – 47, 2005. Proceedings of the Fifth International Conference on Scientific and Clinical Apllications of Magnetic Carriers.

[26] M. Heyd, M. Franzreb, and S. Berensmeier. Integrierte Produktion und Separation von Biotensiden im Mehrphasenreaktor. *CIT*, 82:111–115, 2010.

[27] J. Hu, G. Chen, and I. M.C. Lo. Removal and recovery of Cr(VI) from wastewater by maghemite nanoparticles . *Water Research*, 39(18):4528 – 4536, 2005.

[28] C. Plank, U. Schillinger, F. Scherer, C. Bergemann, J.-S. Rémy, F. Kroetz, M. Anton, J. Lausier, and J. Rosenecker. The Magnetofection Method: Using Magnetic Force to Enhance Gene Delivery. *Biological Chemistry*, 384:737–747, 2003.

[29] A. Roch, Muller R. N., and P. Gillis. Theory of proton relaxation induced by superparamagnetic particles. *Journal of Chemical Physics*, 110:5403–5411, 1999.

[30] A. Roch, F. Moiny, R.N. Muller, and P. Gillis. Water Magnetic Relaxation in Superparamagnetic Colloid Suspensions: The Effect of Agglomeration. In O. Fraissard, J.and Lapina, editor, *Magnetic Resonance in Colloid and Interface Science*, volume 76 of *NATO Science Series*, pages 383–392. Springer Netherlands, 2002.

[31] Q. L. Vuong, P. Gillis, and Y. Gossuin. Monte Carlo simulation and theory of proton NMR transverse relaxation induced by aggregation of magnetic particles used as MRI contrast agents. *J Magn Reson*, 212(1):139–148, Sep 2011.

[32] J. B. Haun, T. J. Yoon, H. Lee, and R. Weissleder. Magnetic nanoparticle biosensors. *Wiley Interdiscip Rev Nanomed Nanobiotechnol*, 2:291–304, Jan 2010.

[33] G. G. Westmeyer, Y. Durocher, and A. Jasanoff. A secreted enzyme reporter system for MRI. *Angew Chem Int Ed Engl*, 49(23):3909–3911, May 2010.

[34] V. Loureiro and A. Querol. The prevalence and control of spoilage yeasts in foods and beverages. *Trends in Food Science & Technology*, 10(11):356 – 365, 1999.

[35] V. Loureiro and M. Malfeito-Ferreira. Spoilage| yeasts in spoilage. In B. Caballero, editor, *Encyclopedia of Food Sciences and Nutrition (Second Edition)*, pages 5530 – 5537. Academic Press, Oxford, second edition edition, 2003.

[36] Maciej Zborowski. Magnetic formulary. In M. Zborowski and J. J. Chalmers, editors, *Magnetic Cell Separation*, volume 32 of *Laboratory Techniques in Biochemistry and Molecular Biology*, pages 29 – 61. Elsevier, 2003.

[37] C. Kittel. Physical Theory of Ferromagnetic Domains. *Rev. Mod. Phys.*, 21:541–583, 1949.

[38] E. H. Frei, S. Shtrikman, and D. Treves. Critical Size and Nucleation Field of Ideal Ferromagnetic Particles. *Phys Rev*, 106:446–455, 1957.

[39] K. M. Krishnan. Biomedical Nanomagnetics: A Spin Through Possibilities in Imaging, Diagnostics, and Therapy. *IEEE Trans Magn*, 46:2523–2558, Jul 2010.

[40] R. Kötitz, P. C. Fannin, and L. Trahms. Time domain study of Brownian and Néel relaxation in ferrofluids. *Journal of Magnetism and Magnetic Materials*, 149:42–46, 1995.

[41] T. Kim, L. Reis, K. Rajan, and M. Shima. Magnetic behavior of iron oxide nanoparticle biomolecule assembly. *Journal of Magnetism and Magnetic Materials*, 295:132–138, Aug 2005.

[42] D. Eberbeck and L. Trahms. Experimental investigation of dipolar interaction in suspensions of magnetic nanoparticles. *Journal of Magnetism and Magnetic Materials*, 323:1228–1232, May 2011.

[43] Brown W. Thermal Fluctuations of a Single-Domain Particle. *Phys Rev*, 130:1677–1686, 1963.

[44] A. H. Lu, E. L. Salabas, and F. Schüth. Magnetic nanoparticles: synthesis, protection, functionalization, and application. *Angew Chem Int Ed Engl*, 46:1222–1244, Jan 2007.

[45] R.M. Cornell and U. Schwertmann. *The iron oxides*. Wiley-VCH Verlag GmbH & Co., 2nd edition, 2003.

[46] R.J. Hunter. *Foundations of Colloidal Science*. Oxford University Press, USA, 2nd edition, 2001.

[47] E. Roduner. Size matters: why nanomaterials are different. *Chem Soc Rev*, 35(7):583–592, Jul 2006.

[48] C. Burda, X. Chen, R. Narayanan, and M.A. El-Sayed. Chemistry and properties of nanocrystals of different shapes. *Chem Rev*, 105(4):1025–1102, Apr 2005.

[49] O. Veiseh, J. W. Gunn, and M. Zhang. Design and fabrication of magnetic nanoparticles for targeted drug delivery and imaging. *Adv Drug Deliv Rev*, 62:284–304, Mar 2010.

[50] J. Drbohlavova, R. Hrdy, V. Adam, R. Kizek, O. Schneeweiss, and J. Hubalek. Preparation and Properties of Various Magnetic Nanoparticles. *Pharmacological Research*, 9:2352–2362, Jan 2009.

[51] M. Mahmoudi, K. Azadmanesh, M. A. Shokrgozar, W. S. Journeay, and S. Laurent. Effect of nanoparticles on the cell life cycle. *Chem Rev*, 111:3407–3432, May 2011.

[52] A. Moore, R. Weissleder, and A. Bogdanov. Uptake of dextran-coated monocrystalline iron oxides in tumor cells and macrophages. *Journal of Magnetic Resonance Imaging*, 7:1140–1145, 1997.

[53] B. D. Chithrani and W. C. Chan. Elucidating the mechanism of cellular uptake and removal of protein-coated gold nanoparticles of different sizes and shapes. *Nano Lett*, 7:1542–1550, Jun 2007.

[54] Y. Gossuin, P. Gillis, A. Hocq, Q. L. Vuong, and A. Roch. Magnetic resonance relaxation properties of superparamagnetic particles. *Wiley Interdisciplinary Reviews: Nanomedicine and Nanobiotechnology*, 1(3):299–310, 2009.

[55] H. Soo Choi, W. Liu, P. Misra, E. Tanaka, J. P. Zimmer, B. Itty Ipe, M. G. Bawendi, and J. V. Frangioni. Renal clearance of quantum dots. *Nat Biotech*, 25:1165–1170, September 2007.

[56] J. S. Weinstein, C. G. Varallyay, E. Dosa, S. Gahramanov, B. Hamilton, W. D. Rooney, L. L. Muldoon, and E. A. Neuwelt. Superparamagnetic iron oxide nanoparticles: diagnostic magnetic resonance imaging and potential therapeutic applications in neurooncology and central nervous system inflammatory pathologies, a review. *J Cereb Blood Flow Metab*, 30:15–35, Jan 2010.

[57] R. Weissleder, D. D. Stark, B. L. Engelstad, B. R. Bacon, C. C. Compton, D. L. White, P. Jacobs, and J. Lewis. Superparamagnetic iron oxide: pharmacokinetics and toxicity. *American Journal of Roentgenology*, 152:167–173, 1989.

[58] M. Levy, F. Lagarde, V. A. Maraloiu, M. G. Blanchin, F. Gendron, C. Wilhelm, and F. Gazeau. Degradability of superparamagnetic nanoparticles in a model of intracellular environment: follow-up of magnetic, structural and chemical properties. *Nanotechnology*, 21:395103, Oct 2010.

[59] D. L. Thorek and A. Tsourkas. Size, charge and concentration dependent uptake of iron oxide particles by non-phagocytic cells. *Biomaterials*, 29:3583–3590, Sep 2008.

[60] E. E. Finney and R. G. Finke. Nanocluster nucleation and growth kinetic and mechanistic studies: a review emphasizing transition-metal nanoclusters. *J Colloid Interface Sci*, 317(2):351–374, Jan 2008.

[61] Y. Sun. Controlled synthesis of colloidal silver nanoparticles in organic solutions: empirical rules for nucleation engineering. *Chem Soc Rev*, 42(7):2497–2511, Apr 2013.

[62] V. K. LaMer and R.H. Dinegar. Theory, Production and Mechanism of Formation of Monodispersed Hydrosols. *Journal of the American Chemical Society*, 72(11):4847–4854, 1950.

[63] J. K. Beattie. Monodisperse colloids of transition metal and lanthanide compounds. *Pure & Appl. Chem.*, 61(5):937–941, 1989. http://dx.doi.org/10.1351/pac198961050937.

[64] X. Peng, J. Wickham, and A. P. Alivisatos. Kinetics of II-VI and III-V Colloidal Semiconductor Nanocrystal Growth: Focusing of Size Distributions. *Journal of the American Chemical Society*, 120(21):5343–5344, 1998.

[65] T. Sugimoto. Preparation of monodispersed colloidal particles. *Advances in Colloid and Interface Science*, 28(0):65 – 108, 1987.

[66] L. Ratke and P.W. Voorhees. *Growth and Coarsening*. Springer Verlag, 2nd edition, 2002.

[67] V.L. Kolesnichenko. *Magnetic Nanoparticles*, chapter Synthesis of Nanoparticulate Magnetic Materials. Wiley-VCH, Weinheim, 2009.

[68] R. Massart. Preparation of aqueous magnetic liquids in alkaline and acidic media. *IEEE Transactions on Magnetics*, 17(2):1247–1248, 1981.

[69] L. Vayssières, C. Chanéac, E. Tronc, and J. P. Jolivet. Size Tailoring of Magnetite Particles Formed by Aqueous Precipitation: An Example of Thermodynamic Stability of Nanometric Oxide Particles. *Journal of Colloid and Interface Science*, 205(2):205–212, 1998.

[70] F.A. Cotton and G. Wilkinson. *Anorganische Chemie*. Verlag Chemie, GmbH, Weinheim/Bergstr., second edition, 1968.

[71] J. P. Jolivet, C. Chanéac, and E. Tronc. Iron oxide chemistry. From molecular clusters to extended solid networks. *Chem Commun (Camb)*, pages 481–487, Mar 2004.

[72] W. Stöber, A. Fink, and E. Bohn. Controlled growth of monodisperse silica spheres in the micron size range. *Journal of Colloid and Interface Science*, 26:62–69, 1968.

[73] S. Laurent, S. Boutry, I. Mahieu, L. Vander Elst, and R.N. Muller. Iron oxide based MR contrast agents: from chemistry to cell labeling. *Curr Med Chem.*, 16:4712–27, 2009.

[74] G. T. Hermanson. *Bioconjugate Techniques*. Academic Press, Elsevier, 2nd edition, 2008.

[75] F.E. Regnier and R. Noel. Glycerolpropylsilane Bonded Phases in the Steric Exclusion Chromatography of Biological Macromolecules. *Journal of Chromatographic Science*, 14(7):316–320, 1976.

[76] J. E. Schiel, R. Mallik, S. Soman, K. S. Joseph, and D. S. Hage. Applications of silica supports in affinity chromatography. *Journal of Separation Science*, 29(6):719–737, 2006.

[77] J. B. Haun, N. K. Devaraj, B. Marinelli, H. Lee, and R. Weissleder. Probing intracellular biomarkers and mediators of cell activation using nanosensors and bioorthogonal chemistry. *ACS Nano*, 5:3204–3213, Apr 2011.

[78] J. B. Haun, N. K. Devaraj, S. A. Hilderbrand, H. Lee, and R. Weissleder. Bioorthogonal chemistry amplifies nanoparticle binding and enhances the sensitivity of cell detection. *Nat Nanotechnol*, 5:660–665, Sep 2010.

[79] C. Rümenapp, B. Gleich, and A. Haase. Magnetic Nanoparticles in Magnetic Resonance Imaging and Diagnostics. *Pharmaceutical Research*, pages 1–15, 2012.

[80] F. Bloch. Nuclear Induction. *Physical Review*, 70:460–474, 1946.

[81] E. M. Purcell, H. C. Torrey, and R. V. Pound. Resonance Absorption by Nuclear Magnetic Moments in a Solid. *Physical Review*, 69:37–38, 1946.

[82] G. J. Stanisz, E. E. Odrobina, J. Pun, M. Escaravage, S. J. Graham, M. J. Bronskill, and R. M. Henkelman. T_1, T_2 relaxation and magnetization transfer in tissue at 3T. *Magn Reson Med*, 54:507–512, Sep 2005.

[83] R. Weissleder, G. Elizondo, J. Wittenberg, A. S. Lee, L. Josephson, and T. J. Brady. Ultrasmall superparamagnetic iron oxide: an intravenous contrast agent for assessing lymph nodes with MR imaging. *Radiology*, 175:494–498, 1990.

[84] C. Chouly, D. Pouliquen, I. Lucet, J. J. Jeune, and P. Jallet. Development of superparamagnetic nanoparticles for MRI: effect of particle size, charge and surface nature on biodistribution. *Journal of Microencapsulation*, 13:245–255, 1996.

[85] H. Ai. Layer-by-layer capsules for magnetic resonance imaging and drug delivery. *Adv Drug Deliv Rev*, 63:772–788, Aug 2011.

[86] D. Pan, S. D. Caruthers, A. Senpan, A. H. Schmieder, S. A. Wickline, and G. M. Lanza. Revisiting an old friend: manganese-based MRI contrast agents. *Wiley Interdiscip Rev Nanomed Nanobiotechnol*, Sep 2010.

[87] J. L. Arias, M. López-Viota, M. A. Ruiz, J. López-Viota, and A. V. Delgado. Development of carbonyl iron/ethylcellulose core/shell nanoparticles for biomedical applications. *Int J Pharm*, 339:237–245, Jul 2007.

[88] P. Pouponneau, J. C. Leroux, and S. Martel. Magnetic nanoparticles encapsulated into biodegradable microparticles steered with an upgraded magnetic resonance imaging system for tumor chemoembolization. *Biomaterials*, 30:6327–6332, Oct 2009.

[89] T. J. Yoon, H. Lee, H. Shao, and R. Weissleder. Highly magnetic core-shell nanoparticles with a unique magnetization mechanism. *Angew Chem Int Ed Engl*, 50:4663–4666, May 2011.

[90] S. Aime, C. Cabella, S. Colombatto, S. Geninatti Crich, E. Gianolio, and F. Maggioni. Insights into the use of paramagnetic Gd(III) complexes in MR-molecular imaging investigations. *J Magn Reson Imaging*, 16:394–406, Oct 2002.

[91] J. S. Choi, J. C. Park, H. Nah, S. Woo, J. Oh, K. M. Kim, G. J. Cheon, Y. Chang, J. Yoo, and J. Cheon. A hybrid nanoparticle probe for dual-modality positron emission tomography and magnetic resonance imaging. *Angew Chem Int Ed Engl*, 47:6259–6262, Jan 2008.

[92] D. Patel, A. Kell, B. Simard, B. Xiang, H. Y. Lin, and G. Tian. The cell labeling efficacy, cytotoxicity and relaxivity of copper-activated MRI/PET imaging contrast agents. *Biomaterials*, 32:1167–1176, Feb 2011.

[93] Y. Gossuin, A. Roch, Muller R. N., and P. Gillis. An evaluation of the contributions of diffusion and exchange in relaxation enhancement by MRI contrast agents. *Journal of Magnetic Resonance*, 158:36–42, 2002.

[94] M. F. Reiser, W. Semmler, and H. Hricak. *Magnetic Resonance Tomography*. Springer, 2008.

[95] D. Forge, Y. Gossuin, A. Roch, S. Laurent, L. Vander Elst, and R. N. Muller. Development of magnetic chromatography to sort polydisperse nanoparticles in ferrofluids. *Contrast Media & Molecular Imaging*, 5(3):126–132, 2010.

[96] P. Gillis, A. Roch, and R. A. Brooks. Corrected equations for susceptibility-induced T_2-shortening. *J Magn Reson*, 137(2):402–407, Apr 1999.

[97] N. Bloembergen and O. Morgan L. Proton Relaxation Times in Paramagnetic Solutions. Effects of Electron Spin Relaxation. 34:842–850, 1961.

[98] P. Gillis and Koenig S. H. Transverse relaxation of solvent protons induced by magnetized spheres: Application to ferritin, erythrocytes, and magnetite. *Magnetic Resonance in Medicine*, 5:323–345, 1987.

[99] R. A. Brooks, F. Moiny, and P. Gillis. On T_2-shortening by weakly magnetized particles: the chemical exchange model. *Magn Reson Med*, 45(6):1014–1020, Jun 2001.

[100] P. Gillis, F. Moiny, and R. A. Brooks. On T(2)-shortening by strongly magnetized spheres: a partial refocusing model. *Magn Reson Med*, 47(2):257–263, Feb 2002.

[101] Muller R. N., P. Gillis, F. Moiny, and A. Roch. Transverse relaxivity of particulate MRI contrast media: From theories to experiments. *Magnetic Resonance in Medicine*, 22:178–182, 1991.

[102] A. Roch, Y. Gossuin, Muller R. N., and P. Gillis. Superparamagnetic colloid suspensions: Water magnetic relaxation and clustering. *Journal of Magnetism and Magnetic Materials*, 293:532–539, May 2005.

[103] I. Koh, R. Hong, R. Weissleder, and L. Josephson. Nanoparticle-target interactions parallel antibody-protein interactions. *Anal Chem*, 81:3618–3622, 2009.

[104] J. M. Perez, L. Josephson, and R. Weissleder. Use of magnetic nanoparticles as nanosensors to probe for molecular interactions. *Chembiochem*, 5:261–264, Mar 2004.

[105] K. Aurich, S. Nagel, G. Glöckl, and W. Weitschies. Determination of the magneto-optical relaxation of magnetic nanoparticles as a homogeneous immunoassay. *Anal Chem*, 79:580–586, Jan 2007.

[106] G. Y. Kim, L. Josephson, R. Langer, and M. J. Cima. Magnetic relaxation switch detection of human chorionic gonadotrophin. *Bioconjug Chem*, 18:2024–2028, 2007.

[107] I. Koh, R. Hong, R. Weissleder, and L. Josephson. Sensitive NMR sensors detect antibodies to influenza. *Angew Chem Int Ed Engl*, 47:4119–4121, 2008.

[108] T. Quillard, K. Croce, F. A. Jaffer, R. Weissleder, and P. Libby. Molecular imaging of macrophage protease activity in cardiovascular inflammation in vivo. *Thromb Haemost*, 105:828–836, May 2011.

[109] H. Lee, E. Sun, D. Ham, and R. Weissleder. Chip-NMR biosensor for detection and molecular analysis of cells. *Nat Med*, 14:869–874, 2008.

[110] J. Baudry, C. Rouzeau, C. Goubault, C. Robic, L. Cohen-Tannoudji, A. Koenig, E. Bertrand, and J. Bibette. Acceleration of the recognition rate between grafted ligands and receptors with magnetic forces. *Proc Natl Acad Sci U S A*, 103:16076–16078, Oct 2006.

[111] H. Lee, T. J. Yoon, and R. Weissleder. Ultrasensitive detection of bacteria using core-shell nanoparticles and an NMR-filter system. *Angew Chem Int Ed Engl*, 48:5657–5660, 2009.

[112] D. Issadore, C. Min, M. Liong, J. Chung, R. Weissleder, and H. Lee. Miniature magnetic resonance system for point-of-care diagnostics. *Lab Chip*, 11:2282–2287, Jul 2011.

[113] J. B. Haun, C. M. Castro, R. Wang, V. M. Peterson, B. Marinelli, H. Lee, and R. Weissleder. Micro-NMR for rapid molecular analysis of human tumor samples. *Sci Transl Med*, 3:71ra16, Feb 2011.

[114] C. March, J. J. Manclús, A. Abad, A. Navarro, and A. Montoya. Rapid detection and counting of viable beer-spoilage lactic acid bacteria using a monoclonal chemiluminescence enzyme immunoassay and a CCD camera. *J Immunol Methods*, 303(1-2):92, Aug 2005.

[115] R. Juvonen, R. Satokari, K. Mallison, and A. Haikara. Detection of spoilage bacteria in beer by PCR. *J. Am. Soc. Brew. Chem.*, 3:99–103, 1999.

[116] O. Lazcka, F. J. Del Campo, and F. X. Muñoz. Pathogen detection: A perspective of traditional methods and biosensors. *Biosensors and Bioelectronics*, 22(7):1205 – 1217, 2007.

[117] M. Hutzler, E. Schuster, and G. Stettner. Ein Werkzeug in der Brauereimikrobiologie. *Brauindustrie*, pages 52–55, 2008.

[118] D. Forge, A. Roch, S. Laurent, H. Tellez, Y. Gossuin, F. Renaux, L. Vander Elst, and R. N. Muller. Optimization of the Synthesis of Superparamagnetic Contrast Agents by the Design of Experiments Method. *The Journal of Physical Chemistry C*, 112(49):19178–19185, Jan 2008.

[119] U. K. Laemmli. Cleavage of Structural Proteins during the Assembly of the Head of Bacteriophage T4. *Nature*, 227(5259):680–685, 08 1970.

[120] Malvern Instruments. *Zetasizer Nano Series User Manual*, 1.1 edition, Feb. 2004.

[121] N. Ban, C. Escobar, R. Garcia, K. Hasel, J. Day, A. Greenwood, and A. McPherson. Crystal structure of an idiotype-anti-idiotype Fab complex. *Proceedings of the National Academy of Sciences*, 91(5):1604–1608, 1994.

[122] J. Coates. *Interpretation of Infrared Spectra, A Practical Approach*. John Wiley & Sons, Ltd, 2006.

[123] A. M. Raem and P. Rauch, editors. *Immunoassays*. Spektrum Akademischer Verlag, 2007.

[124] N. C. Bell, C. Minelli, J. Tompkins, M. M. Stevens, and A. G. Shard. Emerging Techniques for Submicrometer Particle Sizing Applied to Stöber Silica. *Langmuir*, 28(29):10860–10872, 2012.

[125] D. Eberbeck, F. Wiekhorst, S. Wagner, and L. Trahms. How the size distribution of magnetic nanoparticles determines their magnetic particle imaging performance. *Applied Physics Letters*, 98(18):182502, 2011.

Publication List

Parts of this thesis have been published in the following peer-reviewed journal and patent:

- **paper:** Christine Rümenapp, Bernhard Gleich and Axel Haase. Magnetic Nanoparticles in Magnetic Resonance Imaging and Diagnostics. *Pharmaceutical Research*, 2012, 1-15.
- **patent pending:** Haase, A., C. Rümenapp, and B. Gleich, Vorrichtung und Verfahren zur Detektion von Stoffen in einer Flüssigkeit, in 102013215761.4, D.P.-u. Markenamt, Editor. 2013, Technische Universität München: Germany. p. 18.

Acknowledgements

For the success of a PhD, it takes a lot of people who I would like to acknowledge in the following.

First of all, I wish to thank Dr. Bernhard Gleich for his continuous support, encouragement, patience and loyalty throughout the years. Much appreciation goes to Prof. Axel Haase and Prof. Steffen Glaser for scientific discussions and support and giving me the opportunity to work on this thesis.

I was privileged to be allowed to work in the Lab of Prof. Muller, University of Mons, Belgium. Thank you very much for letting me work with your group. Without their help, this would not have been possible. I had a wonderful time in your lab and learned not only a lot about the manufacturing of magnetic nanoparticles but also about the Belgian way of life. I want to extend this to Dr. Raimund Marx for the chemical advices and refreshing my memory on the routine work in a chemical laboratory.

I also want to acknowledge collaborations with Dr. Matthias Opel at the Walther-Meissner Institute, Garching, who performed the M(H) measurements on my magnetic nanoparticles, for Prof. Fritz Wagner from the Physics Department E15 -Group B of the Technische Universität München, who performed the Mössbauer experiments and his patient explanations. The nice TEM images of the particles and the cells were obtained by Dr. Marianne Hanzlik from the Institute of Electronmicroscopy at the department for Chemistry of the Technische Universität München and by Prof. Hans Georg Mannherz from the Ruhruniversität Bochum. Dr. Dietmar Eberbeck from the Physikalische Technische Bundesanstalt in Berlin performed M(H) measurements as well and magnetic particle spectroscopy. Many thanks to all of you.

Thank you to Susanne Schnell-Witteczek and Sepp Hintermair. Thank you for your helping hands in the lab, managing orders and helping out in need. Especial thanks to Sepp for his cell culture know-how and support.

Many thanks go to Alexandra and Norbert. Thank you for being such wonderful colleagues and sharing daily PhD life with me. Thank you for making up a great interdisciplinary team. Appreciations go to our ex-student and now-colleague Alexander for focusing on the physics and explaining them to me.

It was a fortune to meet many wonderful people at my time at the Zentralinstitut für Medizintechnik. Thank you for making a great scientific atmosphere. Many appreciation goes in particular to Dr. Franz Schilling and Thomas Gaaß for helping me with questions on MRI and NMR and with one or the other experiment; for being wonderful colleagues and the

fun we had in- and outside the lab. The Hugel Group for their help and tutoring about functionalisation of surfaces and one or the other chemical from time to time. The Lieleg Group for sharing their equipment and contributing to the laughters in the lab and kitchen.

Thank you to my friends. Franka for pushing me forward, reviewing my thesis and giving me not only friendship support but also scientific support about protein chemistry. Petra and Anna for being there always and sharing family life with me. Mira and Ric, even though you are far away I can always feel your support and thoughts. Johanna and Raphi, for making up the greatest neighbours and floor mates. Meli, for being not only a friend but also the best osteopath my neck and shouder could hope for during the writing process.

My final thanks goes to my family. My mom, Anke, my dad, Thomas, my brother Christian and to Undine and Friedhelm, my grandparents and my uncle with family. Thank you for your unconditional support and faith. Thank you for being my great family, who is always there for me.